STRUCTURAL AND ELECTRONIC PROPERTIES OF BULK MATERIALS AND TRANSITION METAL ALLOYS

Thesis submitted for the degree of
Doctor of Philosophy (Science)
of the
Jadavpur University
2003

Chhanda Basu Chaudhury

S.N. Bose National Centre for Basic Sciences
JD Block, Sector III, Salt Lake City,
Kolkata, 700 098, INDIA

STRUCTURAL AND ELECTRONIC PROPERTIES OF BULK MATERIALS AND TRANSITION METAL ALLOYS

Thesis submitted for the degree of
Doctor of Philosophy(Science)
of the
Jadavpur University

Chhanda Basu Chaudhury

S.N.Bose National Centre for Basic Sciences
JD Block, Sector III, Salt Lake City,
Kolkata, 700 098, INDIA

CERTIFICATE FROM THE SUPERVISOR

This is to certify that the work in this thesis entitled **STRUCTURAL AND ELECTRONIC PROPERTIES OF BULK MATERIALS AND TRANSITION METAL ALLOYS** submitted by Smt. Chhanda Basu Chaudhury, who got her name registered on 19^{th} August, 1998 for the award of **Ph.D. (Science) degree** of **Jadavpur University**, is absolutely based upon her own work under the supervision of Prof. Abhijit Mookerjee and that neither this thesis nor any part of it has been submitted for any degree/diploma or any other academic award anywhere before.

ABHIJIT MOOKERJEE
Senior Professor and Dean (Academic Programme).
S.N.Bose National Centre for Basic Sciences,
Salt Lake, Kolkata, India.

ACKNOWLEDGMENTS

First of all I would like to convey my heartiest gratefulness to my supervisor, Professor Abhijit Mookerjee to whom I owe a lot. In my hard days when I was radarless, on the verge of wreck, he stood beside me with all his kindness, encouragement and wisdom and till then he gradually has guided me to a much awaited and cherished destination. His unremitting discipline, unrelenting persuit and vast knowledge do evoke awe and admiration. Close proximity with him has helped to open up a window to the expansive and bizarre world of materials physics.

I would like to thank all the academic and non-academic staff of the S. N. Bose National Centre For Basic Sciences for their physical and mental support during the days of my stay here. I express my gratitude to the former director, late Prof. C. K. Majumdar and the present director, Prof. S. Dattagupta for giving me the opportunity to work here. I also thank Prof. Rajendra Prasad of IIT, Kanpur for giving me the opportunity to work there. I also acknowledge Prof. O. K. Andersen and Prof. O. Jepsen for allowing me to use the TB-LMTO package extensively. I would like to express my sincerest gratitude to Prof. O. K. Andersen for useful and stimulating discussions with him during SERC school on Condensed Matter, 1999.

I offer my special thanks to Dr. Govindrajan Pari for having meaningful discussions and effective collaboration.

My sincere thanks goes to my friends in S. N. Bose National Centre. Specially I would like to mention the names of Dr. Nityananda Das, Dr. Radhikaprasad Dutta, Dr. Prabhat Thakur, Dr. Subhradip Ghosh, Dr. Biplab Sanyal, Mr. Durga Paudyal, Mr. Atisdipankar Chakraborty, Mr. Monodeep Chakraborty, Mr. Kamal Krishna Saha, Md. Mukul Kabir and Ain-Ul Huda whose constant encouragement, friendly behaviour and fruitful suggessions drove me to carry out my work here. I am also thankful to Dr. Debasish Biswas for academic discussions. I should mention specially the name of Dr. Parthapratim Biswas with whom I have splendid experience of myriad colours.

I am ever grateful to my teachers, Sri Monojit Roy and Sri Bikash Chandra Pal

of Asutosh College, Kolkata, who have motivated me to pursue physics and rendered many a decisive and precious advice at crucial junctures.

I should not forget mentioning the name of Sri Manas Kundu for his support towards the end of my work to completion.

Lastly, though it does not worth mentioning, I am ever indebted to my parents, sister and brothers for their tireless endeavour to help me to complete my work.

I would like to thank the CSIR, India for financial assistance during my research period.

PUBLICATIONS

1. **Ground state properties of alkaline earth chalcogenides** by Basu Chaudhuri C. and Mookerjee A. (submitted to *Int. J. Mod. Phys. B*)

2. **High-pressure studies of $MgTe$ using first-principle electronic-structure calculations** by Basu Chaudhuri C., Pari G., Mookerjee A. and Bhattacharyya A. K., *Phys. Rev.* **B 60** 11 846 (1999)

3. **A study of $MgTe$ doped with transition metals Mn, Fe, Co, and Ni** by Basu Chaudhuri C., Pari G., Mookerjee A. and Bhattacharyya A. K., *Int. J. Mod. Phys. B* (submitted to *Int. J. Mod. Phys. B*)

4. **Electronic structure and magnetism of disordered bcc Fe alloys** by Ghosh S., Sanyal B., Basu Chaudhuri C. and Mookerjee A., *Eur. J. Phys.* **B 23** 455 (2001)

5. **Effect of short-range order on electronic and magnetic properties of disordered Co-based alloys** by Ghosh S., Basu Chaudhuri C., Sanyal B. and Mookerjee A., *J. Magn. Magn. Mater.* **234** 100 (2001)

Contents

List of Figures

List of Tables

Chapter 1

The Linearized Muffin-Tin Orbitals Method

1.1 Introduction

The theory of electronic structure has, for many years, been of great significance for understanding of the physical and chemical properties of solid state materials. Electrons at the microscopic level to a great extent govern the behavior of these materials and a good description may be obtained in terms of the stationary states of the electronic system. One reason for this state of affairs is that the valence electrons are light particles whose motion immediately follow the much heavier ion-cores. In theoretical terms this means that the quantum mechanics of ion-cores and electrons may be treated separately . This procedure is known as the Born-Oppenheimer approximation. According to this one may first solve for the electronic structure and at a latter stage use the energy of the electronic ground state obtained as a function of nuclear positions as a potential energy for the motion of nuclei. The electronic structure problem at this stage consists of finding the eigenstates and eigenvalues of an infinite number of interacting fermions. Further approximations are thus needed. The one-electron approximation treats each electron as an independent particle moving in the fields of the nuclei and the other electrons. One thus has to solve the one electron Schrödinger like equation (referred to as the Kohn-Sham equation) :

$$\left(-\nabla^2 + V\right)\psi_j = E_j\psi_j \qquad (1\text{-}1)$$

We shall always use (unless specifically states) atomic units in which lengths are

given in units of bohrs and energies in Rydbergs. V is the effective one electron potential and as stated before, consists of the electrostatic field from nuclei and the charge clouds of all other electrons, together with corrections for exchange and correlation.

A rigorous as well as convenient formulation for metals is provided by the density functional formalism of Hohenberg and Kohn (1964) and Kohn and Sham(1965). The local density approximation (LDA) like the $X\alpha$ method of Slater leads to an effective one electron potential which again is a function of electron density, $\rho(\vec{r}) = \sum_j^{occ} |\psi_j(\vec{r})|^2$. Since the density in turn depends on the solutions of the effective one electron Schrödinger equation we are led to perform the electron structure calculation in a self-consistent manner.

In course of the last decade or so the LMTO developed by Andersen and coworkers (Andersen *et al* (1985, 1986, 1987, Skriver (1984)) has emerged as a very convenient and accurate scheme for studying the electronic structure of solids within the density functional formalism. An interesting review is available in the monograph *Electronic Structure of Alloys, Surfaces and Clusters* (Mookerjee and Sarma (2003)).

The LMTO is physically transparent and computationally convenient and indeed possesses a number of very attractive features :

Firstly, the method is cast in the form of a standard algebraic eigenvalue problem and therefore has the speed required in a self-consistent calculation which often has to run through a number of cycles.

Secondly like all other linear methods such as the linearized augmented plane wave method (LAPW) or the linear augmented spherical wave method (LASW) it is an approximate method but it has the required accuracy over a chosen energy window.

Thirdly, it employs the same type of basis functions for all elements in the periodic table thus leading to a conceptually consistent description of physical trends throughout the periodic table.

Fourthly, as indicated earlier, the method is physically transparent and can be used in several levels of approximations.

In this chapter we shall briefly describe the formalism behind the LMTO. We shall discuss the major approximations and also the means to go beyond them and present some applications.

Because of its versatility the LMTO method may be applied to problems ranging from complicated self-consistent calculations in crystals with many atoms per unit cell to the construction of simple analytical models of solid state problems. The method has also been extended to treat impurities in crystals and for surfaces (Lambrecht *et al* (1983)) with Green function techniques which may be used both metal and semiconductor hosts. For disordered alloys, Kudrnovský *et al* (1987, 1990) have developed a single site coherent potential approximation (CPA) within the LMTO Self-consistent Green function calculations for extended defects, as well as, self-consistent recursion calculations for liquids and amorphous materials have also been performed utilizing the LMTO formalism. The method moreover can be extended to provide, the full potential, non-spheridized electron density required for a speedy and accurate evaluation of total energy and force calculations. (Andersen *et al* (1985))

We have divided the chapter in three sections. In section 1.2 we shall give a schematic description of the LMTO method and introduce the necessary physical quantities. In section 1.3 we shall give a detailed discussion of the formalism with in depth discussions of relevant physical quantities. In section 1.4 we shall discuss some extensions of the LMTO formalism and some notable applications.

1.2 Schematic Description of the LMTO Method

The objective of the method is firstly to solve the Schrödinger's equation

$$\left[-\nabla^2 + V(\vec{r})\right] \psi_j(\vec{r}) = E_j \psi_j(\vec{r}) \tag{1-2}$$

of the one electron problem. The potential $V(\vec{r})$ is characteristic of an infinite periodic solid and is often approximated by a collection of muffin tin wells centered at the *lattice points* $\vec{R}$. Thus

$$V(\vec{r}) = \sum_R V_{MT}(\vec{r}_R) + V_0 \tag{1-3}$$

Here $\vec{r}_R = \vec{r} - \vec{R}$ and $V_{MT}(\vec{r}_R)$ is spherically symmetric about $\vec{R}$ in a sphere of radius S and zero outside. V_0 is the flat potential in the interstitial region .

Secondly one has to construct the charge density as,

$$\rho(\vec{r}) = \sum_{j}^{occ} |\psi_j(\vec{r}|^2 \tag{1-4}$$

and subsequently use it to find the potential $V(\vec{r})$ for the next self-consistency iteration by solving the Poisson equation for the Hartree part and by using one of the standard expression for the exchange-correlation part. We have used both the von-Barth-Hedin (von Barth and Hedin (1972)) and the Langreth-Mehl (Langreth and Mehl (1983)) exchange-correlations. After the self-consistency has been achieved for the potential one may evaluate with its help various quantities of physical interest such as the total energy of the electrons and the nuclei in the Born-Oppenheimer approximation, the pressure, the stress etc. The one electron states that are significant for physical and chemical properties range from the energy where an electron can tunnel from one atom to the next up to the Fermi level. The relevant energy range thus extends approximately half a rydberg on either side of the potential energy maximum and the latter about a rydberg below the Fermi level.

We may classify the older one electron methods according to whether one seeks wave functions as an expansion in some set of fixed basis functions, like plane waves, atomic orbitals , Gaussian orbitals as in the LCAO, plane waves and Gaussian orbital pseudopotentials methods etc. or whether one expands the wave functions in the set of energy and potential dependent partial waves as is done in Wigner -Seitz cellular method, Korringa-Kohn-Rostoker method, and the augmented plane wave method (APW).

In the former methods (1-2) is solved by expanding the wave functions approximately as,

$$\sum_{R_n,L} \chi_{R_n,L;j} u_{R_n,L;j} \approx \psi_j(\vec{r}) \tag{1-5}$$

where $\{\chi_{R_n,L;j}\}$ is the energy independent basis set . The coefficients $u_{R_n,L;j}$ and the one electron energies E_j 's are obtained with help of Rayleigh-Reitz variational principle as the eigenvalues and eigenvectors of the algebraic eigenvalue problem

$$(H - E_j O)\,\vec{u}_j = 0 \tag{1-6}$$

From a computational standpoint the procedure is highly convenient and is employed in the LMTO method with the Hamiltonian matrix

$$H_{R'_n,L';R_n,L} = \langle \chi_{R'_n,L'} | \left(-\nabla^2 + V\right) | \chi_{R_n,L} \rangle \tag{1-7}$$

and the overlap matrix

$$O_{R'_n,L';R_n,L} = \langle \chi_{R'_n L'} | \chi_{R_n L} \rangle \tag{1-8}$$

For crystals the above basis functions can be transformed into Bloch functions

$$\chi_{R_n,L}(\vec{k},\vec{r}) \equiv \sum_{\vec{T}} \chi_{R_n L}(\vec{r} - \vec{R} - \vec{T}) \exp(i\vec{k}\vec{T}) \tag{1-9}$$

so that for each Bloch vector the matrix obtained is of convenient size . In (1-9) the vector $\vec{R}$, runs over the atoms in the primitive cell only, $\vec{T}$ are the translational vectors of the lattice, and the Bloch function is normalized to unity in the primitive cell.

The essential disadvantage of the fixed basis methods is that these basis sets must be large in order to be reasonably complete. Atomic orbitals or Gaussian sets must include several radial functions per atom and angular momentum component. For plane waves exceedingly large basis sets are needed for materials having other than broad bands.

In the partial wave methods, since the muffin tin potential is considered to be spherically symmetric about the atomic sites in the muffin tins, the Scrödinger equation is separable in radial and angular parts. The Schrödinger equation may be solved exactly in terms of partial wave expansions,

$$\psi_j(\vec{r}) = \psi_{int,j}(E_j,\vec{r}_i) + \sum_{RL} \phi_{RL}(E_j,\vec{r}_R) C_{RL,j} \tag{1-10}$$

where $\psi_{int,j}$ is the interstitial part of the wave function.

The radial part of the partial wave $\phi_{RL}(\epsilon,\vec{r})Y_{LM}(\hat{r})$ for the MT well at $\vec{R}$ may be obtained by numerically integrating the corresponding radial Schrödinger equation.

The wave function in the interstitial region may be obtained by a plane wave expansion or by an analytical continuation of the partial wave expansions from a near site. In this work we shall frequently assume that , that the partial wave

vanishes outside its own sphere and the interstitial function vanishes outside the interstitial region i. e. inside the spheres. The partial waves are functions of energy variable E and one electron energies are those E_j for which coefficients c_j can be found such that the partial wave expansions from various spheres join continuously and differentiably together. The way this matching condition is formulated differs algebraically from one method to another, but in general the result is a set of linear homogeneous equations

$$M(E)c_j = 0 \tag{1-11}$$

having a secular matrix $M(E)$. This matrix in contrast to the $(H-OE)$ matrix of the earlier method has a complicated non-linear energy dependence,and the procedure for determining the one electron energies and the corresponding coefficients c_j is by first tracing a root E_j of $M(E)$ and then solving the linear homogeneous equations by substituting $E = E_j$. Even for moderately sized matrices this requires an order of magnitude more computation than the eigenvalue method. The partial wave methods have a number of positive points : the solution provided by them for the MT potential is highly accurate and for close-packed, high point symmetry structures they are in general more accurate than the corresponding fixed basis method. The partial waves apply equally well to any atom in the periodic table.

The LMTO method incorporates the desirable features of both the fixed basis and partial wave methods. The following simple discussion, provided by Andersen *et al* (Andersen *et al* (1985)), will make the methodology transparent. In the next section we shall give a more rigorous and detailed discussion.

We shall consider a simple model of bonding in a diatomic molecule to discuss the question of incorporation of energy dependent partial waves in an energy independent basis set. We shall employ only one energy independent orbital $\chi_L(\vec{r})$.

In an LCAO type description the bonding and anti bonding states are approximately expressed as

$$\Psi_A^B(\vec{r}) \approx \chi_L^\alpha(\vec{r}) \pm (-1)^l \chi^\alpha(\vec{r} - \vec{R}) \tag{1-12}$$

where the meaning of the superscript α will be clarified soon,and their energies E = E_A or E_B may be estimated from (1-6). Inside atomic spheres, the exact states can

be expressed by partial wave expansions

$$\Psi_{A/B}(\vec{r}) = \sum_L \phi_L^\alpha \left(\vec{r}, E_{A/B}\right) h_L^\alpha \tag{1-13}$$

where the subscripts indicate we have included the the energy dependence of the expansion coefficients h_L^α arising from the choice of the orbitals in the normalization of the partial waves.

The function χ_L should be augmented by $\phi_L(\vec{r}, E_B)$ and we see that if we augment the tail $\chi_L(\vec{r} - \vec{R})$ by $1/2(-1)^{l'} \sum_{L'} \left[\phi_{l'}^\alpha(r, E_B) - \phi_{l'}^\alpha(r, E_A)\right] Y_L(\hat{r}) h_{L'}^\alpha$ and the head $\chi_L(\vec{r})$ by $1/2\left[\phi_L^\alpha(r, E_B) + \phi_L^\alpha(r, E_A)\right]$ we may approximately obtain (1-13) from (1-12). In a solid the states of lowest and highest energies are E_B and E_A respectively and with predominant l character correspond to bonding and anti-bonding between most of the nearest neighbours. In addition, a band of states between E_B and E_A exists arising from all possible combinations of bonding and anti-bonding between nearest neighbours throughout the crystal with B_ℓ and A_ℓ being the bottom and top of the ℓ-th band. Now the entire range of energy dependence has to be supplied by the tails of $\chi_L^\alpha(\vec{r} - \vec{R})$ from other sites. (We now understand the meaning of the superscript α upon χ). The tail functions are therefore augmented by the energy derivative functions

$$\dot{\phi}_L(E_\nu, r) \equiv \left[\partial\phi_l(E, r)/\partial E\right]_{E=E_\nu} \tag{1-14}$$

The heads are similarly augmented by an appropriate linear combination of $\phi_l(E_\nu, r)$ and $\dot{\phi}_L(E_\nu, r)$. The augmented orbital thus takes the form

$$\chi_{RL}^\alpha(\vec{r_R}) = \chi_{RL}^{\alpha,i}(\vec{r_R}) + \phi_{RL}^\alpha(\vec{r_R}) + \sum_{R'} \sum_{L'} \dot{\phi}_{RL}^\alpha(\vec{r_R}) h_{RL,R'L'}^\alpha \tag{1-15}$$

where $\phi_{RL}(\vec{r_R})$ and $\dot{\phi}_{RL}(\vec{r_R})$ are defined to be zero outside a chosen augmentation sphere about the site $\vec{R}$. Moreover χ^i is the interstitial part of the augmented orbital and is defined to be zero inside all augmentation spheres, and the original approximate orbital in the interstitial region between the spheres. The normalization of ϕ and the expansion coefficients are so chosen that the augmented orbitals are continuous and once differentiable at the spheres. We shall show in the next section that both ϕ and $\dot{\phi}$ are orthogonal to the core states and phi-phi-dot augmentation

thus can be used to orthogonalize the orbitals (Andersen (1977), Skriver (1984)) to the core states.

The augmented orbitals may be used as basis functions in a variational calculation. For closed-packed systems the potential is nearly spherically symmetric for a large volume around each atom and one may thus choose the augmentation spheres as large as possible either as touching muffin-tin spheres or as slightly overlapping, space-filling Wigner-Seitz spheres.

For such large augmentation spheres the radial degree of freedom is sufficiently described by the $\phi, \dot{\phi}$ augmentation only i.e. only one orbital per ℓm value and thus a minimal basis set is obtained in this manner. The Taylor series of the radial function truncated after the first two terms

$$\phi_l(E, r) \approx \phi_l(E_\nu, r) + \dot{\phi}_l(E_\nu, r)(E - E_\nu) \tag{1-16}$$

can describe fairly well the change of radial wave function throughout the atomic sphere ($r \leq s$) from the bonding to the anti-bonding levels.

Further since the $\phi - \dot{\phi}$ is used in a variational scheme, the error of the radial wave function which is of second order in $(E - E_\nu)$ gives rise to errors in fourth order in $(E - E_\nu)$ in the energy bands. We thus see that to set up the linear muffin tin orbital method one starts with the muffin-tin orbitals which are solutions of the Helmholtz equation

$$(\nabla^2 + \kappa^2)\psi = 0 \tag{1-17}$$

as the envelope set. Each linear method use a characteristic envelope set. The plane waves give rise to the LAPW method, the Slater type orbitals to the LSTO method. The chosen envelope set should be reasonably complete in the interstitial region. After a set is chosen each basis function is then expanded in spherical harmonics about all atomic sites $\vec{R}$ and each component is continuously and differentiably augmented inside spheres of chosen radii s_R . In the above we have given a schematic description of the whole method. In the next section we shall discuss in detail how the methodology is implemented.

1.3 Detailed Formulation of the LMTO

In this section we shall give a more elaborate description of $\phi, \dot{\phi}$ functions, the envelope functions, the potential parameters and the various functions that arise in the LMTO framework. For convenience we shall divide the section in four subsections. We shall introduce mathematical expressions whenever necessary.

1.3.1 The radial wave functions and the Potential function

We shall first study one electron states viz. $\phi, \dot{\phi}$ in a single sphere,their logarithmic derivatives $D_l(E)$ at the sphere boundary and introduce the potential functions $P_L(E)$.

As indicated before the one electron wave functions inside a muffin tin sphere are the solutions of the radial Schrödinger equation

$$(H - E)\ |\psi_l(E, r)\rangle = 0 \tag{1-18}$$

Let us define a radial function normalized to unity in the sphere

$$\phi_l(E, r) \equiv \langle \psi_l^2(E, r) \rangle^{-1/2}\ \psi_l(E, r) \tag{1-19}$$

where the normalization integral is

$$\begin{aligned} \langle \psi_l^2(E, r) \rangle &\equiv \int \psi_{lm}^{\star}(E, r) \psi_{lm}(E, r) d\vec{r} \\ &= \int_0^s \psi_l^2(E, r) r^2 dr \int \int |Y_{lm}(\hat{r})|^2 d\Omega \\ &= \int_0^s \psi_l^2(E, r) r^2 dr \end{aligned} \tag{1-20}$$

In LMTO attention is focused upon energy range centered around some energy E_ν which we are free to choose for the problem at hand. Thus for each angular momentum component ℓ we choose an energy $E_{\nu l}$ and use the energy independent basis set formed by normalized radial wave function

$$\phi_{\nu l}(r) \equiv \phi_l(E_\nu, r) \tag{1-21}$$

and its energy derivative,

$$\dot{\phi}_{\nu l}(r) \equiv [\partial \phi_l(E_\nu, r)/\partial E]_{E=E_\nu} \tag{1-22}$$

The corresponding logarithmic derivatives at the sphere boundaries ($r = s$) are

$$\begin{aligned} D_{\nu l} &= s\ \phi'_{\nu l}(s)/\phi_{\nu l}(s) = s\ \psi'_{\nu l}(s)/\psi_{\nu l}(s) \\ D_{\dot{\nu} l} &= s\dot{\phi}'_{\nu l}(s)/\phi_{\nu l}(s) \end{aligned} \tag{1-23}$$

where dash(l) indicates spatial derivative. By (1-19),the normalization integral in the sphere is unity i. e.

$$\langle \phi(E)|\phi(E)\rangle = 1 \tag{1-24}$$

One can obtain by successive differentiation

$$\langle \dot{\phi}_\nu|\phi_\nu\rangle = 0 \tag{1-25}$$

and also

$$\langle \dot{\phi}_\nu^{\,2}\rangle = -\langle \phi_\nu|\ddot{\phi}_\nu\rangle \tag{1-26}$$

From (1-18) we obtain the u-th energy derivative of the partial wave $\phi_\nu^u(S)$ and the corresponding logarithmic derivative $D\{\phi_\nu^u(S)\}$ and their integral $\langle \phi_\nu|\phi_\nu^u\rangle$ in the sphere.

Differentiating the Schrödinger equation (1-18)successively with respect to energy one obtains

$$(H - E_\nu)|\psi_\nu^u\rangle = u|\psi_\nu^{u-1}\rangle \tag{1-27}$$

From Green's second identity we get,

$$\begin{aligned} \langle \psi_2|H - E|\psi_1\rangle &= \int_{r\le s}\left[\psi_1^\star(\vec{r})\nabla^2\psi_2(\vec{r}) - \psi_2^\star(\vec{r})\nabla^2\psi_1(\vec{r})\right]d\vec{r} \\ &= \int_{r=s}\left[\psi_1^\star(\vec{r})\frac{\partial\psi_2(\vec{r})}{\partial n} - \psi_2^\star(\vec{r})\frac{\partial\psi_1}{\partial n}\right]s^2 d\Omega \\ &= (D_2 - D_1)\ s\psi_1(s)\psi_2(s) \end{aligned} \tag{1-28}$$

Here $\psi_1(\vec{r})$ and $\psi_2(\vec{r})$ are arbitrary functions of the form $\psi_l(r)Y_{lm}(\hat{r})$ with the same l,m and radial logarithmic derivatives D_1, D_2 respectively . $\partial/\partial n$ means differentiation with respect to the normal to the surface of the sphere and also in the first step we have inserted the Hamiltonian $H = -\nabla^2 + V(r)$ and used

$$\langle \psi_1|E - V(r)|\psi_2\rangle = \langle \psi_1|E - V(r)|\psi_1\rangle$$

If we set $\psi_1 = \psi_\nu^u(r), \psi_2 = \psi_\nu(r)$ we obtain from (1-28)

$$\begin{aligned} & \langle\psi_\nu|H - E_\nu|\psi_\nu^u\rangle - \langle\psi_\nu^u|H - E_\nu|\psi_\nu\rangle \\ = \; & [D_\nu - D\{\psi_\nu^u\}]\, s\psi_2(s)\psi_\nu^u(s) \end{aligned} \tag{1-29}$$

Also from (1-27)we obtain the result,

$$\begin{aligned} u\langle\psi_\nu|\psi_\nu^{u-1}\rangle &= \langle\psi_\nu|H - E_\nu|\psi_\nu^u\rangle \\ &= [D_\nu - D\{\psi_\nu^u\}]\; s\psi_\nu(s)\psi_\nu^u(s) \end{aligned} \tag{1-30}$$

By putting $u = 1$,we get

$$D_{\dot\nu} = D_\nu - \left[s\phi_\nu(s)\dot\phi_\nu(s)\right]^{-1}$$

i. e.

$$D_\nu - D_{\dot\nu} = \left[s\phi_\nu(s)\dot\phi_\nu(s)\right]^{-1} \tag{1-31}$$

Now we shall prove that $\dot\phi_\nu(r)$ is orthogonal to the core states ϕ_n defined by

$$\left.\begin{array}{lcll} H|\phi_n\rangle & = & E_n\phi_n & \\ D\{\phi_n\} & = & D_\nu & \text{with } n \neq \nu \\ \phi_n(s) & << & \phi_\nu(s) & \end{array}\right\} \tag{1-32}$$

ψ_n and ψ_ν are orthogonal and thus by using,

$$0 = \langle\phi_n|\phi_\nu\rangle = \langle\phi_n|H - E_\nu|\phi_\nu\rangle$$

Interchanging the functions in the last integral and also from (1-29) we obtain,

$$\begin{aligned} \langle\phi_n|H - E_\nu|\dot\phi_\nu\rangle &= \langle\dot\phi_\nu|H - E_\nu|\phi_n\rangle \\ &+ [D_\nu - D_{\dot\nu}]\, s\phi_n(s)\dot\phi_\nu(s) \end{aligned}$$

$$\begin{aligned} 0 &= \langle\dot\phi_\nu|H - E_\nu|\phi_\nu\rangle + [D_\nu - D_{\dot\nu}]\, s\phi_n(s)\dot\phi_n(s) \\ &= (E_n - E_\nu)\langle\dot\phi_\nu|\phi_n\rangle + \phi_n(s)/\phi_\nu(s) \end{aligned}$$

utilizing also (1-31). From the last of (1-32) we have the second term on the right hand side approximately zero ,and hence we obtain the desired result

$$\langle\dot\phi_\nu|\phi_n\rangle = 0 \; for \; n \neq \nu \tag{1-33}$$

Any linear combination of $\phi_\nu(r)$ and $\dot{\phi}_\nu(r)$ is thus orthogonal to the core states and augmentation of the muffin tin orbital by $\phi_\nu(r) - \dot{\phi}_\nu(r)$ functions is a suitable way of orthogonalization to the core states. Also as mentioned at the end of last section by augmenting tails with $h_{RL,R'L'}\dot{\phi}_{\nu l}(r)$ at the neighbouring sites they are also made orthogonal to the core states of these neighbouring atoms also.

To define ϕ^α, $\dot{\phi}^\alpha$, one may choose the following relation with ϕ , $\dot{\phi}$,

$$\phi^\alpha \equiv [1 + (E - E_\nu)\, o^\alpha_{Rl}]\, \phi_{Rl}(E, r)$$

and therefore

$$\dot{\phi}^\alpha_{Rl}(E_\nu, r) = \dot{\phi}_{Rl}(r) + \phi_{Rl}(r) o^\alpha_{Rl} \tag{1-34}$$

also

$$\phi^\alpha_{Rl}(r) \equiv \phi_{Rl}(r)$$

The constant o^α_{Rl} is to be so defined such that the linear combination of $\dot{\phi}^\alpha_{Rl}$ functions in (1-15)) in previous section matches continuously and differentially to the tail of $\chi_{R'L'}(r'_R)$.

We now introduce the potential functions which is very important for our subsequent work. The potential function for energy E and angular momentum l is defined by

$$P_l(E) = 2(2l+1)\frac{D_l(E) + l + 1}{D_l(E) - l} \tag{1-35}$$

The log-derivative $D_l(E)$ is a monotonically increasing function of energy except at its singularities. The potential function is therefore an increasing function of energy. For each l,both the functions consist of periods in energy(Skriver,1984;Andersen 1977) labelled by the principal quantum number and separated by energy V_{nl} defined to be those for which

$$D_l(V_{nl}) = l \tag{1-36}$$

Also within each period we further define three parameters

$$\begin{aligned} D_l(B_{nl}) &= 0 \\ D_l(C_{nl}) &= -l - 1 \\ D_l(A_{nl}) &= -\infty \end{aligned}$$

The energies V_{nl}, B_l, C_l, A_l represent the square well pseudo-potential, the bottom, the centre and the top respectively of the $n\ell$-th energy band.

According to the Wigner-Seitz rule a ℓ-band is formed in the energy range where the log-derivative is negative i.e. from $D_l(B_{nl}) = 0$ to $D_l(A_{nl}) = -\infty$. Now

$$P_l(B_l) = -\frac{l+1}{l} \times 2(2l+1)$$

and

$$P_l(A_l) = 2(2l+1)\frac{(D_l + l + 1)}{D_l - l} = 2(2l+1)$$

Thus from Wigner-Seitz rule the band is formed in terms of potential function in the range,

$$-\left(\frac{2l+1}{l}\right)(l+1) < P_l < 2(2l+1) \tag{1-37}$$

and has hence a width on the P-scale of $2(2l+1)^2/l$. We further observe

$$P_l(C_l) = 0 \tag{1-38}$$

We shall again discuss the potential function in later sections.

In the LMTO formalism as noted before,the Schrödinger equation is treated as an eigenvalue problem subject to the boundary condition of a specified log-derivative at the sphere boundary. One can further consider parametrization of the function $E_l(D)$ inverse to $D_l(E)$. For this purpose we shall use the Rayleigh-Reitz variational principle with a radial trial function of arbitrary log-derivative D at the sphere boundary given as

$$\phi(D, r) = \phi_\nu(r) + \omega(D)\dot{\phi}_\nu(r)$$

where

$$\omega(D) = -\frac{\phi_\nu}{\dot{\phi}_\nu}\frac{D - D_\nu}{D - D_{\dot{\nu}}} \tag{1-39}$$

Here $\phi_\nu \equiv \phi_\nu(s)$, $\dot{\phi}_\nu \equiv \dot{\phi}_\nu(s)$. Further we see that

$$\phi_\nu(D, s) = \phi_\nu \frac{D_\nu - D_{\dot{\nu}}}{D - D_{\dot{\nu}}} \tag{1-40}$$

With the basis $\phi_{lm}(D, \vec{r}) = i^l Y_{lm}(\hat{r})\phi_l(D, r)$ the matrix elements of the Hamiltonian in the sphere,

$$\langle \phi_{l'm'}(D')|H - E_{\nu l}|\phi_{lm}(D)\rangle = \omega_l(D)\delta_{l'l}\delta_{m'm} \tag{1-41}$$

$$\langle \phi_{l'm'}(D')|\phi_{lm}(D)\rangle = \delta_{l'l}\delta_{m'm}\left[1+\omega_l(D')\omega_l(D)\langle \dot{\phi}^2_{\nu l}\rangle\right] \tag{1-42}$$

With these we obtain the variational estimate

$$\begin{aligned} E_l(D) &= E_{\nu l} + \frac{\langle \phi_{lm}(D)|H-E_{\nu l}|\phi_{lm}(D)\rangle}{\langle \phi^2_{lm}(D)} \rangle \\ &= E_{\nu l} + \frac{\omega_l(D)}{1+\langle \dot{\phi}^2_{\nu l}\rangle \omega_l^2(D)} + O(\epsilon^3) \end{aligned} \tag{1-43}$$

where $\epsilon = E - E_\nu$.

The variational estimate $E_l(D)$ is thus a single valued function confined to a energy-window

$$E_\nu - \left(\frac{1}{2}\right)\langle \dot{\phi}^2_\nu\rangle^{-1/2} \leq E(D) \leq E_\nu + \left(\frac{1}{2}\right)\langle \dot{\phi}^2_\nu\rangle^{-1/2} \tag{1-44}$$

We shall refer to (1-44) in later subsections.

1.3.2 Envelope fun tions and structure matrices

In this subsection we sl ıll discuss the envelope functions and structure matrices. The requirement of an envelope function is that it should be reasonably complete in the interstitial region i. e. in the region between atomic spheres. For closed-packed lattices the interstitial region is small,and if one applies the atomic sphere approximation mentioned before, this region need not be considered. In such cases the above requirement is mild but even then each envelope function should be smooth so that the radius of convergence of the one centre expansion exceeds the atomic sphere radius. For fast ℓ-convergence each envelope function should be a reasonable solution of the Schdinger equation in a larger region between the atoms. The augmentation then needs to take place only for the few lower ℓ-components i.e. s- , p-, (for transition and noble metals) the d-, and for rare earths and actinides the f-components. As noted before the potential between the atoms is rather flat and kinetic energy $\kappa^2 \equiv E - V(r)$ is rather small. One may thus choose for the envelopes the solutions of the Helmholtz equation $(\nabla^2 + \kappa^2)\chi^{(e)} = 0$ with κ^2 small. In the partial wave methods like the KKR or the APW ,the potential is approximated by a muffin tin potential and κ^2 is chosen equal to $E - V_{MTZ}$ such that $\chi^{(e)}$ is an exact solution of the Schrödinger equation in the interstitial region. For evaluating the

Hamiltonian and overlap matrices we must include the integrals over the interstitial region or eliminate these by employing ASA. The simplest choice is to set $\kappa^2 = 0$ and in this work we shall mainly deal with this set. The envelope function $\chi^{(e)}_{RL}$ of a MTO is thus defined to be atom centered angular momentum eigenvalues of the Laplace's equation and this has the form of static multipole field given by

$$K_{RL}(\vec{r_R}) = \left(\frac{r_R}{\omega}\right)^{-l-1} Y_L(r_R) \tag{1-45}$$

where $\vec{r_R} = \vec{r} - \vec{R}$, and $L \equiv$ composite angular momentum index.

We note that the above is irregular at $\vec{r} \equiv \vec{R}$ and is the irregular solution of the Laplace equation, the regular solution being

$$J_{RL}(\vec{r_R}) = \left(\frac{r_R}{\omega}\right)^{l} Y_L(\hat{r_R}) \tag{1-46}$$

$K_{RL}(\vec{r_R})$ may be expanded in terms of $J_{RL}(\vec{r_R})$ as,

$$\begin{aligned} K_{RL}(\vec{r_R}) &= -\sum_{L'} \left(\frac{r_R}{\omega}\right)^{l'} \frac{Y_{L'}(\vec{r_{R'}})}{2(2l+1)} S_{RL,R'L'} \\ &= -\sum_{L'} J_{R'L'}(\vec{r'_R}) S_{RL,R'L'} \end{aligned} \tag{1-47}$$

valid for $r_R \leq |\vec{R} - \vec{R'}|$. All distances are measured in terms of an arbitrary length ω ,which may be the lattice constant or the Wigner-Seitz radius of the lattice. The expansion coefficients $S \equiv [S_{R'L',RL}]$ are called the structure constants. Actually they are called bare canonical structure constants for reasons to be clarified soon. They only depend on atomic positions in units of ω and is thus independent of the atomic sphere potential and the lattice parameters or W. S. sphere radius. They are thus fixed for a particular lattice type and hence to be calculated only once for a bcc,fcc or sc system. They may be expressed as two centre integrals with the z-axis chosen along the inter-atomic vector $\vec{R} - \vec{R'}$,of length d. The bare canonical structure constants are given by the general formula

$$S_{l'lm} = (-)^{l+M+1}(l+l')2\left[\frac{(2l'+1)(2l+1)}{(l'+M)(l'-M)(l+M)(l-M)}\right]^{1/2}\left(\frac{\omega}{d}\right)^{l'+l+1} \tag{1-48}$$

with particular elements like

$$S_{ss\sigma} = -2\left(\frac{\omega}{d}\right), S_{sp\sigma} = (2\sqrt{3})\left(\frac{\omega}{d}\right)^2 \tag{1-49}$$

etc. For a general direction of z-axis the structure constant matrix is to be obtained from (1-48) and table I in (Slater and Koster,1954) or directly from table II in (Andersen *et al* ,1978). In (1-15) the requirement of fast l-convergence leads to a long-range power law decay for the muffin tin orbitals(MTO). But as indicted in section 1.1 the envelope function is to be augmented not only inside the atoms at which it is centered but also inside all other atoms. We may therefore instead of (1-45) use solutions of Laplace's equation which are irregular also at the neighbouring sites. A highly localized in space envelope set is thus obtained.

We shall use a special bra-ket notation (used very frequently by Andersen and coworkers) for convenience of analysis. The unscreened or bare MTO ,$K^0_{RL}(r_R)$ and the screened MTO ,$K^\alpha_{RL}(r_R)$ are denoted by $|K^0_{RL})^\infty$ and $|K^\alpha_{RL})^\infty$. The superscript ∞ indicates that the functions extend throughout all space. Omissions of the subscript ∞ ,as in $|K^0_{RL}\rangle$, $|J^0_{RL}\rangle$ means that the functions are truncated outside the W. S. sphere centered around $\vec{R}$. In this notation the bare multipole about all sites of the structure are given by,

$$|K)^\infty = |K\rangle - |J\rangle S \tag{1-50}$$

The on-site elements of S are defined to be zero. The regular solutions $J_{R'L'}$ are modified by adding the amount $-\alpha_{R'l'}$ of the irregular solution

$$|J^\alpha\rangle = |J\rangle - |K)\alpha \tag{1-51}$$

Here α is the diagonal matrix $[\alpha_{Rl}]$. The multipole field screened according to (1-51) is defined in analogy with (1-50) as,

$$|K^\alpha)^\infty \equiv |K\rangle - |J\rangle S^\alpha \tag{1-52}$$

By inserting (1-51) in (1-52) we find that the screened structure constant matrix is given by

$$S^\alpha = S(\hat{1} - \alpha S)^{-1} \tag{1-53}$$

or

$$(S^\alpha)^{-1} + \alpha = S^{-1} \tag{1-54}$$

or

$$S^\alpha = S + S\alpha S^\alpha \tag{1-55}$$

and the screened multipole field is given by,

$$\begin{aligned} |K^\alpha\rangle^\infty &= |K\rangle^\infty(\hat{1} - \alpha S)^{-1} \\ &= |K^0\rangle^\infty(\hat{1} + \alpha S) \end{aligned} \tag{1-56}$$

The so called screening charge is therefore given by αS^α. We now want to determine α such that (1-53)-(1-56) have the shortest range. We furthermore want the screened structure constant to be canonical i. e. independent of the atomic potential and the scale of the structure and therefore choose the elements $[\alpha_{Rl}]$ to be site independent constants. In fact we are left with three parameters $\alpha_s, \alpha_p, \alpha_d$. By numerical inversion of the 9×9 matrix $\alpha_l^{-1} - S_{ll'}^k$ on a lattice with Bloch vectors $\vec{k}$ and subsequent Fourier transformation $S^\alpha_{RL,R'L'}$ may be obtained. The shortest possible range is given by α_ℓ 's

$$\begin{aligned} &\alpha_s = 0.3458 \ ; \ \alpha_p = 0.05303 \ ; \ \alpha_d = 0.010714 \\ &\alpha_\ell = 0 \ for \ \ell > 2 \end{aligned} \tag{1-57}$$

The parameters are generally represented by β and the representation is also given the superscript β. By plotting any element of S^α ,say the $ss\sigma$ element against d/ω the shortest possible range may be ascertained. More details may be found in Andersen(1984).

We thus want to use $|K^\alpha\rangle^\infty$ outside augmentation spheres and $|\chi^\alpha\rangle$ inside. Both the functions can be expressed as one-centre angular momentum expansions (as in (1-15))and hence the augmentation is done by continuous and differentiable matching of at the sphere radii(s_R) . Each radial function

$$K_L(r) \equiv \left(\frac{r}{\omega}\right)^{-l-1}$$

and

$$J_l^\alpha(r) \equiv [2(2l+1)]^{-1}\,(r/\omega)^l - \alpha_l\,(r/\omega)^{-l-1}$$

should be matched by a linear combination of $\phi_l(r)$ and $\dot{\phi}_l(r)$. The latter two functions we recollect were obtained numerically from the radial Schrödinger equation at energies E_ν and $E_\nu + dE_\nu$ and subsequent normalization in the sphere. A function

f(r) can be matched in the previously discussed manner to a linear combination of two functions in the following way

$$f(r) \rightarrow [a(r)W\{f,b\} + b(r)W\{f,a\}]\, W\{a,b\}^{-1} \tag{1-58}$$

where

$$\begin{aligned} W\{a,b\} &\equiv S^2\,[a(S)b'(S) - b(S)a'(S)] \\ &\equiv Sa(S)b(S)\,[D\{b\} - D\{a\}] \end{aligned} \tag{1-59}$$

is the Wronskian and $D\{\}$ is the log-derivative at the sphere boundary r=S,

$$\left.\begin{aligned} f(S) &= \alpha a(S) + \beta b(S) \\ f'(s) &= \alpha a'(s) + \beta b'(S) \end{aligned}\right\} \tag{1-60}$$

Solving for α,β we obtain,

$$\alpha = -\frac{f(S)b'(S) - f'(S)b(S)}{a(S)b'(S) - a'(S)b(S)} \tag{1-61}$$

$$\beta = -\frac{f(S)a'(S) - f'(S)a(S)}{a(S)b'(S) - a'(S)b(S)} \tag{1-62}$$

We thus see that,

$$\begin{aligned} \alpha &= -\frac{W\{f,b\}/S^2}{W\{a,b\}S^2} \\ &= -\frac{W\{f,b\}}{W\{a,b\}} \end{aligned}$$

Similarly

$$\beta = -\frac{W\{f,a\}}{W\{a,b\}} \tag{1-63}$$

Hence

$$\alpha a(r) + \beta b(r) = -\frac{[a(r)W\{f,b\} + b(r)W\{f,a\}]}{W\{a,b\}} \tag{1-64}$$

whose matching with f(r) can be performed provided $W\{a,b\} \neq 0$. The Wronskian of ϕ and $\dot{\phi}$ may be obtained from (1-59) and Green's second identity as

$$1 = \langle \phi^2 \rangle = \langle \phi | -\nabla^2 + V - E_\nu | \dot{\phi}^\alpha \rangle \tag{1-65}$$

to be

$$W\{\phi, \dot{\phi}\} = 0 \tag{1-66}$$

For the radial solutions of Laplace's equation we obtain ,

$$W\{K, J^\alpha\} = W\{k, J\} = \omega/2 \tag{1-67}$$

The tail of the MTO is expanded in (1-52) in J^α functions only ,whereas we recall that the tail functions of the energy independent MTO introduced earlier is expanded in terms of $\dot{\phi}^\alpha$ functions only. These two radial functions for the same Rl must have identical logarithmic derivatives. With a given α ,$J^\alpha(r)$ is specified by (1-51) whereas $\dot{\phi}^\alpha$ by (1-34). Since they have the same log-derivative from (1-59),we have

$$W\{J^\alpha, \dot{\phi}^\alpha\} = 0 \tag{1-68}$$

also as

$$\dot{\phi}^\alpha(r) = \dot{\phi}(r) + \phi(r) o^\alpha_{RL} \tag{1-69}$$

Hence,

$$0 = W\{J^\alpha, \dot{\phi}^\alpha\} = W\{J^\alpha, \dot{\phi}\} + o^\alpha W\{J^\alpha, \phi\} \tag{1-70}$$

and thus

$$o^\alpha = -\frac{W\{J^\alpha,\ \dot{\phi}^\alpha\}}{\{J^\alpha, \phi\}} \tag{1-71}$$

Once again utilizing the result (1-68) we obtain an expression for α in terms of logarithmic derivatives of $\dot{\phi}^\alpha$ as,

$$W\{J^\alpha, \dot{\phi}^\alpha\} = 0$$

or,

$$W\{J, \dot{\phi}^\alpha\} - \alpha W\{K, \dot{\phi}^\alpha\} = 0$$

hence,

$$\begin{aligned} \alpha_l &= \frac{W\{J, \dot{\phi}^\alpha\}}{W\{k, \phi^\alpha\}} \\ &= \frac{(s/\omega)^{2l+1}}{2(2l+1)} \frac{D\{\dot{\phi}^\alpha - l\}}{D\{\dot{\phi}^\alpha\} + l + 1} \end{aligned} \tag{1-72}$$

while the last expressions on the right hand side had been obtained by expanding the Wronskians in terms of log-derivatives.

If $a(r) \equiv \dot{\phi}^{\alpha}(r)$ and $b(r) \equiv \phi(r)$ then we find that,

$$J(r) \rightarrow \dot{\phi}^{\alpha}(r) W\{J^{\alpha}, \phi\} \tag{1-73}$$

$$K(r) \rightarrow \dot{\phi}^{\alpha}(r) W\{K, \phi\} - \phi(r) W\{K, \dot{\phi}^{\alpha}\} \tag{1-74}$$

The augmented multipole field thus has the one-centre expansion ,

$$|K^{\alpha}\rangle \rightarrow |\phi\rangle W\{K, \dot{\phi}^{\alpha}\} - |\dot{\phi}^{\alpha}\rangle \left[-W\{K, \phi\} + W\{J^{\alpha}, \phi\} + W\{J^{\alpha}, \phi\} S^{\alpha}\right] \tag{1-75}$$

where the $W\{\}$ are diagonal matrices which also obey a useful relation

$$W\{K, \dot{\phi}^{\alpha}\} W\{J^{\alpha}, \phi\} = \omega/2 \tag{1-76}$$

In the next subsection we shall introduce the atomic sphere approximation (ASA) and obtain expressions for Hamiltonian and overlap in this approximation.

1.3.3 Atomic Sphere Approximation

In the Atomic Sphere Approximation (ASA) the solid is assumed to be wholly composed of slightly overlapping atomic Wigner Seitz spheres. As a result there is no interstitial region. The LMTO formalism for the approximation assumes a particularly simple form which we shall discuss in some details now. The Wigner-Seitz spheres are taken as augmentation spheres and χ^{i} term in (1-15) drops out and the non-spherical components of the potential are neglected.

We shall use frequently the special bra-ket notation introduced earlier. The augmented orbital in this notation may be expressed as,

$$|\chi^{\alpha}\rangle^{\infty} = |\phi\rangle + |\dot{\phi}^{\alpha}\rangle h^{\alpha} \tag{1-77}$$

As noted before $|\chi^{\alpha}_{RL}\rangle^{\infty}$ are functions spread out over all space,whereas $|\chi^{\alpha}_{RL}\rangle$ is restricted to its own augmentation spheres. Also we rewrite (1-34) as

$$|\dot{\phi}^{\alpha}\rangle = |\dot{\phi}\rangle + |\phi\rangle o^{\alpha} \tag{1-78}$$

For the MTO's o^α is a diagonal matrix. We also obtain for the interaction between ϕ and $\dot{\phi}^\alpha$ and their energy derivatives the following matrix equation

$$\begin{aligned} \langle\phi|\phi\rangle &= \hat{1} \quad ; \quad \langle\phi|\dot{\phi}^\alpha\rangle = 0 \\ \langle\phi|\dot{\phi}^\alpha\rangle &= o^\alpha \quad ; \quad \langle\dot{\phi}^\alpha|\dot{\phi}^\alpha\rangle = p^\alpha = (o^\alpha)^2 + p \end{aligned} \tag{1-79}$$

p is a diagonal matrix with elements

$$p_{RL} = \langle\dot{\phi}^2_{RL}\rangle = \int_0^{rsS_R} \dot{\phi}^2_{RL}(E,r) r^2 dr \tag{1-80}$$

We note that $0 \leq p_{RL} \leq p^\alpha_{RL,RL}$. We recollect from (1-44) that $p^{1/2}_{RL}$ corresponds to the energy window.

The expression for the Hamiltonian and overlap matrices will be introduced now. The overlap matrix

$$O^\alpha = {}^\infty\langle\chi^\alpha|\chi^\alpha\rangle^\infty = \hat{1} + o^\alpha h^\alpha + (o^\alpha h^\alpha)^\dagger + h^\alpha p^\alpha h^\alpha \tag{1-81}$$

Apart from the on site terms of (1-81) the terms in the first part of (1-81) are the one, two,three centre terms respectively. We recollect here that

$$|\chi\rangle^\infty = |\chi\rangle^i + |\phi\rangle + |\dot{\phi}^\alpha\rangle h^\alpha$$

For calculating the Hamiltonian matrix we recollect the following relations

$$\begin{aligned} (-\nabla^2 + V)|\phi^\alpha(E)\rangle &= E|\phi^\alpha(E)\rangle \\ (-\nabla^2 + V - E_\nu)|\phi^\alpha(E)\rangle &= 0 \\ (-\nabla^2 + V - E_\nu)|\phi^\alpha\rangle &= |\phi\rangle \end{aligned} \tag{1-82}$$

As a result

$$\begin{aligned} H^\alpha &= {}^\infty\langle\chi^\alpha| - \nabla^2 + V|\chi^\alpha\rangle^\infty \\ &= (\hat{1} + o^\alpha h^\alpha)^\dagger h^\alpha + \left(\hat{1} + o^\alpha h^\alpha\right)^\dagger E_\nu \left(\hat{1} + o^\alpha h^\alpha\right) + h^\alpha E_\nu p h^\alpha \end{aligned} \tag{1-83}$$

which also once again involves one,two,three centre terms. In other words the diagonal matrix E_ν commutes with the surrounding matrices and the second and third terms may be subsumed in the overlap matrices.

By rewriting (1-77) in terms of (1-78) we obtain,

$$|\chi^{\alpha}\rangle^{\infty} = |\phi\rangle(\hat{1} + o^{\alpha}h^{\alpha}) + |\phi\rangle h^{\alpha} \tag{1-84}$$

Assuming $(\hat{1}+o^{\alpha}h^{\alpha})$ can be inverted we can go back to the unscripted representation defined in terms of ϕ and $\dot{\phi}$ originally introduced in (1-21),(1-22) as,

$$|\chi\rangle^{\infty} \equiv |\chi^{\alpha}\rangle^{\infty}(\hat{1} + o^{\alpha}h^{\alpha})^{-1} = |\phi\rangle + |\dot{\phi}\rangle h \tag{1-85}$$

In the new basis the Hamiltonian is given by

$$H = E_{\nu} + h + hE_{\nu}ph \equiv H^{(2)} + hE_{\nu}ph \tag{1-86}$$

and since H is hermitian,E_{ν},p are diagonal matrices h too is a hermitian matrix. The overlap matrix in this representation is given by,

$$O = \hat{1} + hph \tag{1-87}$$

The new set of orbitals is orthogonal to the first order in $h \approx H - E_{\nu}$ and it is specified by the vector analogue of the scalar first order Taylor series (1-16) for energy dependence of the radial wave functions. In the terminology of LMTO the associated representation is called the $\gamma-$ representation and the physical quantities (orbitals, Hamiltonian etc.) is given the superscript γ . Thus we see that in the ASA, the matrix h alone determines the Hamiltonian and the overlap,as well as coefficients in the one-centre expansion (1-15). The matrices E_{ν} and p are the diagonal potential parameters . Utilizing the matching conditions of earlier

By a comparison with χ_{RL} in (1-77) with (1-75),we see that

$$|K^{\alpha}_{RL}\rangle^{\infty} \rightarrow -|\chi^{\alpha}_{RL}\rangle^{\infty} W\{K, \dot{\phi}^{\alpha}\} \equiv |\chi^{\alpha}_{RL}\rangle^{\infty} \left(\tfrac{2\Delta^{\alpha}_{RL}}{w}\right) \tag{1-88}$$

Thus

$$|\chi^{\alpha}_{RL}\rangle^{\infty} = |\phi\rangle + |\dot{\phi}\rangle \left[-\frac{W\{K,\phi\}}{W\{K,\dot{\phi}^{\alpha}\}} + \frac{W\{J^{\alpha},\phi\}}{W\{K,\dot{\phi}^{\alpha}\}} S^{\alpha}\right] \tag{1-89}$$

so that

$$h^{\alpha} \equiv -\frac{W\{K,\phi\}}{W\{K,\dot{\phi}^{\alpha}\}} + \frac{W\{J^{\alpha},\phi\}}{W\{K,\dot{\phi}^{\alpha}\}} S^{\alpha} \tag{1-90}$$

From (1-67),(1-73) and (1-74) we get

$$W\{K,\dot{\phi}^\alpha\}W\{J^\alpha,\phi\} = \frac{w}{2} \tag{1-91}$$

hence,

$$h = -\frac{W\{K,\phi\}}{W\{K,\dot{\phi}^\alpha\}} + \left(\frac{2}{w}\right)^{1/2} W\{J^\alpha,\phi\}S^\alpha W\{J^\alpha,\phi\}\left(\frac{2}{w}\right)^{1/2} \tag{1-92}$$

The approximate Hamiltonian $H^{\alpha\ (1)} \equiv E_\nu + h^\alpha$ is thus obtained as

$$\begin{aligned} H^{(1)} &\equiv E_\nu + h^\alpha \\ &= E_\nu - \frac{W\{K,\phi\}}{W\{K,\dot{\phi}\}} + (2/w)^{1/2}\, W\{J^\alpha,\phi\}S^\alpha W\{J^\alpha,\phi\}(2/w)^{1/2} \\ &\equiv c^\alpha + (\Delta^\alpha)^{1/2}\, S^\alpha\, (\Delta^\alpha)^{1/2} \end{aligned} \tag{1-93}$$

Here

$$c^\alpha \equiv E_\nu - \frac{W\{K,\phi\}}{W\{K,\dot{\phi}^\alpha\}} \tag{1-94}$$

and

$$(\Delta^\alpha)^{1/2} \equiv (2/w)^{1/2} W\{J^\alpha,\phi\} \tag{1-95}$$

are LMTO potential parameters both being diagonal matrices. The above formulae (1-94) to (1-95) are valid for any choice of α provided the corresponding S^α defined through (1-53) to (1-55) does not have any poles. We may thus choose

$$\gamma = \frac{W\{J,\dot{\phi}\}}{W\{K,\dot{\phi}\}} \equiv \frac{(s/w)^{(2l+1)}}{2(2l+1)}\,\frac{D\{\dot{\phi}\}-l}{D\{\dot{\phi}\}+l+1} \tag{1-96}$$

$o^\alpha = 0$ from (1-71) and $\dot{\phi}^\alpha(r) = \phi(r)$.

The corresponding second order Hamiltonian is given by,

$$\begin{aligned} H^{(2)} \equiv E_\nu + h &= E_\nu - \frac{W\{K,\phi\}}{W\{K,\dot{\phi}\}} + (2/w)^{1/2} W\{J^\gamma,\phi\}S^\gamma W\{J^\gamma,\phi\}(2/w)^{1/2} \\ &= c^\gamma + (\Delta^\gamma)^{1/2}\ S^\gamma\ (\Delta^\gamma)^{1/2} \end{aligned} \tag{1-97}$$

where

$$|J^\gamma\rangle \equiv |J\rangle - |K\rangle\gamma$$

and

$$W\{J^\gamma,\phi\} = (w/2)W\{K,\dot{\phi}\}^{-1} \tag{1-98}$$

The structure factor matrix in γ -representation is obtained from

$$S^{\gamma} \equiv S^{0}\left[\hat{1} - \gamma S^{0}\right] = S^{\alpha}\left[\hat{1} - (\gamma - \alpha)\, S^{\alpha}\right]^{-1} \tag{1-99}$$

The first potential parameter

$$\begin{aligned} c^{\alpha} &\equiv E_{\nu} - W\{K,\phi\}/W\{K,\dot{\phi}^{\alpha}\} \\ &= E_{\nu} - (2/w)W\{K,\phi\}W\{J^{\alpha},\phi\} \end{aligned} \tag{1-100}$$

which determines the position of the Rl band and the screened potential parameters

$$(\Delta^{\alpha})^{1/2} \equiv -(2/w)^{1/2}W\{J^{\alpha},\phi\} = -(w/2)^{1/2}W\{K,\dot{\phi}\}^{-1} \tag{1-101}$$

determines the width and the hybridization strength of the band. That, the definition (1-100),is equivalent to the earlier definition of C in (1-37) as the band centre can be seen from the following simple argument. Recollecting that

$$\begin{aligned} K(r) &\rightarrow -W\{K,\dot{\phi}^{\alpha}\}\left[\phi(r) - \dot{\phi}^{\alpha}(r)\tfrac{W\{K,\phi\}}{W\{K,\dot{\phi}^{\alpha}\}}\right] \\ &= \left(\frac{1/2w}{\Delta^{\alpha}}\right)^{1/2}\left[\phi(r) - (c^{\alpha} - E_{\nu})\dot{\phi}^{\alpha}(r)\right] \\ &\approx \left[\frac{K(s)}{\phi^{\alpha}(C,S)}\right]\phi(C,r) \end{aligned}$$

Thus we see that c^{α} is the energy to the first order in its deviation from E_{ν} for which the radial solution of Schrödinger equation matches onto the K(r),(at $r = s$ in the above) the LMTO envelope,which is the irregular solution of the of the Laplace's equation. Thus c^{α} is the energy for which the logarithmic derivative takes the value $-l-1$. Thus the definition of c^{α}, is equivalent to what was stated earlier in (1-37). Further (1-101) shows that $\Delta^{\alpha 1/2}$ is proportional to the amplitude of the corresponding radial wave function at the average W. S. radius of the lattice ω . We note that

$$(\Delta^{\alpha})^{1/2} \approx (w/2)^{1/2}\frac{\phi^{\alpha}(C,S)}{K(S)} \approx (w/2)^{1/2}\,\phi^{\alpha}(C,S) \tag{1-102}$$

For α 's chosen independently of the potential then , $H^{(1)}$ as is evident from (1-94) and (1-95),depends only on $\phi(S)$ and $D\{\phi\}$ but not on $D\{\dot{\phi}\}$,and in this case the

information about the energy derivative is carried entirely by o^α as is seen from (1-71). When $\alpha = \gamma$ as in (1-96) it becomes equivalent to $D\{\dot{\phi}\}$. Also C is the energy for which $\phi(E,r)$ has the logarithmic derivative -l -1 at the sphere to the order $(C - E_\nu)^2$ and $\Delta^{1/2}$ becomes the value $(\omega/2)^{1/2}\,\phi(C,\omega)$ to order $(C - E_\nu)$.

One can thus see that $H^{(1)}$ is a Hamiltonian correct to first order whereas $H^{(2)}$ is correct to second order.

We have earlier mentioned that the most localized orbitals are obtained for $\alpha \equiv \beta$ whose magnitudes also we provided earlier. The many decimal places however do not indicate that the localization of S^α depends that sensitively on the exact values of α but rather the values correspond to the the logarithmic derivative values $D_\ell\{\dot{\phi}^\alpha\} = 2.0,\ 2.4$ and 2.6 for $\ell = 0,\ 1,\ 2$ with $D_{i\ell}\{\phi\}_{s=w} = \ell$ for $\ell \geq 3$ which were the parameters actually used in the numerical calculation of S^α .

The fourth potential parameter is p defined in (1-80). We have shown it earlier in (1-44), that $p^{-1/2}$ is the size of the energy window inside which a linear method is supposed yield realistic results.

1.3.4 Calculation of total energy and charge density within the ASA

In the ASA for the calculation of band structure to second order in $(E_j - E_\nu)$ we have three possible ways in accordance with what we studied in earlier sections. These procedures will be discussed for convenience at the end of this section.

For a crystalline material characterized by Bloch vectors $\{\vec{k}\}$ energy eigenvalues accurate up to second order in $(E_j - E_\nu)$ may be obtained from the matrix equation for the Hamiltonian in the orthogonal representation

$$H^\gamma(\vec{k})u_j(\vec{k}) = u_j(\vec{k})E_j(\vec{k})$$

or as

$$u_j^\dagger H^{\gamma(2)} u_j = E_j^{(2)} \tag{1-103}$$

For each $\vec{k}$ the eigenvectors form a unitary matrix correct to $E_j(\vec{k}) - E_\nu$ are now given by

$$\psi_j(\vec{k},\vec{r}) \;=\; |\chi^\gamma(\vec{k})\rangle u_j(\vec{k})$$

$$
\begin{aligned}
&= \left[|\phi\rangle + |\dot{\phi}^{\gamma}\rangle h^{\gamma}(\vec{k})\right] u_j(\vec{k}) + |K^{\gamma}_{Rl}\rangle b_j(\vec{k}) \\
&= \sum_{RL}\left[\phi_{Rl}(r_R) + \dot{\phi}^{\gamma}_{Rl}(r_R)(E_j(\vec{k}) - E_{\nu Rl})\right]\sum_m Y_L(\hat{r}_R)u_{RL,j}(\vec{k}) \\
&\quad + \sum_{\vec{T},\vec{R},L} K_{RL}(\vec{r}_R + \vec{T})\exp i.\vec{k}.\vec{T} b_{RL,j}(\vec{k})
\end{aligned}
$$

The interstitial part is given by the last term drops out in the ASA calculation for the electron density in the self-consistent procedure.

The spherically averaged charge density needed to construct the ASA potential for the next iteration toward charge density is

$$\rho_R(r) = \frac{1}{4\pi}\sum_l \left[\phi^2_{Rl}(r)m^0_{Rl} + 2\phi_{Rl}(r)\dot{\phi}^{\gamma}_{Rl}(r)m^1_{Rl} + \phi_{Rl}(r)\ddot{\phi}_{Rl}m^2_{Rl}\right] \tag{1-104}$$

in terms of the energy moments of the l-projected density of states,

$$m^q_{Rl} = \sum_{j\vec{k},occ}\left[E_j(\vec{k}) - E_\nu\right]^q \sum_m |u_{Rl,j}(\vec{k})|^2 \tag{1-105}$$

The wave function correct to first order in $(E_j - E_\nu)$ is given by,

$$
\begin{aligned}
\psi_j(\vec{r}) &= \sum_{RL}\chi_{RL}(\vec{r}_R)u_{RL,j} \\
&= \sum_{RL}\left[\phi_{RL}(r_R) + (\epsilon^{(2)}_j - \epsilon_{\nu Rl})\dot{\phi}_{Rl}(r_R)\right]Y_L(\vec{r}_R)u_{RL,j} \\
&\approx \sum_{RL}\phi_{RL}(\epsilon_j, r_R)Y_L(\vec{r}_R)u_{RL,j}
\end{aligned} \tag{1-106}
$$

where the fact that $\vec{u}$ diagonalizes $H^{\gamma,(2)}$ have allowed us to transform to multi-centre expansion of overlapping energy independent orbitals into one centre expansion of non-overlapping energy dependent partial waves. The eigenvalues $E^{(2)}_j$ have errors of third and higher orders in their deviation from E_ν because the second order terms in the Hamiltonian and overlap matrices have been neglected so far.

The term extra in the Hamiltonian (1-86) are most easily taken into account by first order perturbation theory. From (1-6) and (1-85)-(1-86) we get,

$$
\begin{aligned}
0 &= \vec{u}^{\dagger}_j\left[H^{(2)} + hE_\nu ph - E(\hat{1} + hph)\right]\vec{u}_j \\
&= E^{(2)}_j + u^{\dagger}_j E_\nu p(E^{(2)}_j\hat{1} - E_\nu)^2 u_j - E\left[\hat{1} + u^{\dagger}_j p(E^{(2)}_j\hat{1} - E_\nu)^2\vec{u}_j\right]
\end{aligned}
$$

from which we obtain the one electron energy correct to second order in $(E_j - E_\nu)$

$$E_j = E_j^{(2)} + \frac{\sum_{RL} E_{\nu R\ell}\, p_{R\ell}\, (E_j^{(2)} - E_{\nu R\ell})^2 \sum_m |u_{R\ell,j}|^2}{1 + \sum_{R\ell}\, p_{R\ell}\, (E_j^{(2)} - E_{\nu R\ell})^2 \sum_m |u_{R\ell,j}|^2} \tag{1-107}$$

For making self-consistent calculations in ASA electron density spherically averaged in each sphere is needed . For this purpose one-centre expansions are sufficiently accurate. The spherical number density per spin is in general given by,

$$\rho_R(r) = (4\pi)^{-1} \sum_\ell \int^{E_f} \phi_{Rl}^2\, N_{R\ell}(E) dE$$

in terms of ℓ -projected density of states

$$N_{R\ell}(E) = \sum_j \delta(E - E_j) \sum_m |u_{RL,j}|^2 \tag{1-108}$$

We shall now expand $\phi(r)$ in a Taylor series and define the projected density of states and define the projected total density of states

$$\rho_{R\ell} \equiv \int^{E_f} N_{R\ell}(E) dE = \sum_j^{occ} |u_{RL,j}|^2 \tag{1-109}$$

and moments

$$m_{R\ell}^{(q)} = \int^{E_f} (E - E_{\nu Rl})^q\, N_{R\ell}(E) dE \tag{1-110}$$

and the density of states may be conveniently expressed as

$$\rho_R(r) = (4\pi)^{-1} \sum_\ell \left[n\, \phi^2(r) + 2\, m_{R\ell}^{(1)}\, \phi(r)\dot{\phi}(r) + m_{R\ell}^{(2)} \{\dot{\phi}^2(r) + \phi(r)\ddot{\phi}\} \right] \tag{1-111}$$

(1-111) is valid to second order . The subscript $R\ell$ has been dropped for convenience inside the square brackets. Since, as shown in earlier subsection, the eigenvectors are correct to second order, hence $\phi(r)$ has been expanded up to second order in Taylor series. It should be noted that the projection in (1-109)-(1-110) is onto the non-overlapping partial waves as well as onto the overlapping nearly orthogonal orbitals. This follows from (1-106). In (1-111) the first term contributes to the net l-charge in the sphere and the remaining terms redistribute the l-charge within the sphere. We can see this by integrating each term in the sphere.

The total energy of the electrons in ground state according to the density functional theory (Hohenberg and Kohn (1964), Skriver (1984)) is given by,

$$E_{tot} = T + \int\int \frac{\rho(\vec{r})\rho(\vec{r}')}{|\vec{r}-\vec{r}'|}\, d^3r d^3r' + E_{XC}\{n(\vec{r})\} + \int v_{ext}(\vec{r})\ \rho(\vec{r}) d^3(\vec{r}) \qquad \text{(1-112)}$$

Here $v_{ext}(\vec{r})$ is the electrostatic potential from the nuclei and $n(\vec{r})$ is the total electronic density generated by some potential $V(\vec{r})$. Since E_{tot} is obtained variationally $V(\vec{r})$ need not be the actual self-consistent atomic sphere potential. In the ASA, the kinetic energy is :

$$T = \int^{E_f} EN(E)dE - \sum_R \int^{S_R} v_R(r)\rho_R(r)4\pi r^2 dr \qquad \text{(1-113)}$$

Here the second term is the electron-electron interaction energy within density functional theory. In (1-113) above N(E) and $\rho_R(r)$ include both spin directions. Although the remaining terms require the full, rather than the spherically averaged $\rho(r)$ but if symmetry lowering displacements are not involved the spherically averaged $\rho(r)$ is sufficiently accurate. Using these approximations and including the electrostatic interaction between the ion-cores and within local density approximation the total energy expression may be suitably represented as,

$$E_{tot} = T + \sum_R \sum_{R'} \frac{Z_R\, Z_{R'}}{|\vec{R}-\vec{R}'|} + \sum_R U_R \qquad \text{(1-114)}$$

The second term in (1-114) is the Madelung term and Z_R is nuclear minus the electronic charge in the sphere centered at R . The third term is the sum of intrasphere interactions between the electrons and between the electrons and the nucleus in the sphere,that is,

$$U_R = \int_0^{s_R} \left[E_{XC}[\rho(r)] - 2\frac{Z}{r} + \int_0^s \frac{\rho(\vec{r}')4\pi r'^2 dr'}{|\vec{r}-\vec{r}'|} \right] 4\pi r^2 dr \qquad \text{(1-115)}$$

dropping the subscript R within the bracket.

In actual self-consistent numerical schemes after the calculation of the charge density, in each iteration,the potential is obtained by solving the Poisson's equation mentioned in section 3.1, and thereafter obtain by solving the Schrödinger equation the quantities $\phi_{Rl}, \dot{\phi}_{Rl}, \ddot{\phi}_{Rl}$ and the potential parameters $C_{Rl}, \Delta_{Rl}, p_{Rl}$ etc. and the cycle is repeated until self-consistency is achieved.

The normal practice is to mix the output density from the current cycle and the input density from the previous cycle to obtain a 'new' input density for calculating the potential which is closer to the self-consistent one .

A widely used procedure is the linear mixing (Dederichs and Zeller (1983) and references therein) by which the input density at the $M+1$ -th iteration is obtained by

$$\rho^{in}_{M+1} \;=\; \alpha\, \rho^{out}_{M} + (1-\alpha)\, \rho^{in}_{M}$$

where α the mixing parameter belongs to the range $0 \leq \alpha \leq 1$. Other mixing schemes such as the Anderson mixing (Anderson (1964), Matheiss and Hamman (1986)), Broyden mixing (Broyden (1965), Srivastava (1985)) are also in vogue. The mixing is necessary because a small change in input density may cause a large change in the output density thus causing a large fluctuation in the calculation.

1.4 Extensions and applications of the LMTO-ASA

Various types of extensions and improvements over the ASA are in use and references may be found in the LMTO literature (Andersen *et al* (1984, 1985)) The ASA approximates the the unit cell to be a sphere and also truncates the one centre expansion after the *d*-block. Corrections for both of these may be introduced by the the *combined correction* scheme. Full potential LMTO techniques have been developed for clusters and molecules by Springborg *et al* (1987) and for crystals by Fernando *et al* (1986), Weyreich (1988), Blöchl (1989) and Methfessel (1989, 1988). Green function techniques have been developed within LMTO for treating impurities in crystals and for surfaces and interfaces (Lambrecht *et al* (1986)).

A simple as well as accurate coherent potential approximation within TB-LMTO formalism for substitutionally disordered alloys had been developed by Kudrnovský *et al* (1987, 1990). Also self-consistent recursion method calculation for liquids and amorphous systems (Nowak *et al* 1990) and self-consistent Green function calculation for extended defects has been performed with TB-LMTO .

The screened structure factor matrix is also truncated beyond the $l = 2$ block i.e. by setting $\alpha_l = 0$ for $l > 2$. If we refer to the $l > 2$ orbitals by H and the $l \leq 2$ orbitals by L and the corresponding blocks of structure matrix accordingly we may

obtain the HL block of S^{α}

$$(S^{\alpha})^{HL} = \left(S^{0}\right)^{HL} + \left(S^{0}\right)^{HL} \alpha_{L} \left(S^{\alpha}\right)^{LL} \tag{1-116}$$

The HH block too may be obtained by,

$$(S^{\alpha})^{HH} = \left(S^{0}\right)^{HH} + \left(S^{0}\right)^{HL} \left[(\alpha_{L}) + \alpha_{L} \left(S^{\alpha}\right)^{LL} \alpha_{L}\right] \left(S^{0}\right)^{LH} \tag{1-117}$$

This technique is often referred to as the blow-up technique.

A particularly important tool in the LMTO calculational scheme is the downfolding technique which we shall discuss in some detail now. Although the minimal MTO basis set usually contains nine orbitals one s, three p and five d orbitals per atom per spin it is sometimes possible and also convenient to adopt an even smaller basis set. The downfolding serves many useful purposes (Lambrecht *et al* (1986)) such as providing simple physical pictures of phenomena,calculation of structural energies by the Andersen force theorem (Andersen *et al* (1985)), in calculating charge density profiles at surfaces. Also as we shall discuss a little latter the occurrence of ghost bands may be avoided by application of this technique.

The downfolding technique is a particular type of screening transformation. From the above equation, we see that the multi-centre MTO expansion which may be written in the form $\sum_{RL} |\chi_{RL}(r_R)\rangle^{\infty} N^{0}_{Rl}(E)^{-1} u_{Rl}(E)$ to be the solution of the Schrödinger equation for the solid provided the KKR-ASA equations are satisfied. The partial wave set in the approximate one centre expansion may be divided into a lower set and a lower set $\phi_L(E,r)$ and a higher set $\phi_H(E,r)$. Let us correspondingly divide the diagonal matrices of Potential function into higher H and lower L blocks namely $S^{0}_{LL}, S^{0}_{HH}, S^{0}_{HL}$ etc. This division can be made such that for the higher block $|P^{0}_{H} \gg |S^{0}_{HH}|$. Rewriting the KKR-ASA equation (eq) as $\sum_{R'L',RL} \left(P^{0}_{RL} - S^{0}_{R'L',RL}\right) N^{0-1}_{RL} u^{0}_{RL} = 0$ we expand them in block matrix form as introduced above,

$$\left[P^{0}_{L} - S^{0}_{LL}\right] \left[N^{0}_{L}(E)\right]^{-1} u_{L}(E) - S^{0}_{LH} \left[N^{0}_{H}(E)\right]^{-1} u_{H}(E) = 0_{L} \tag{1-118}$$

and,

$$-S^{0}_{HL} \left[N^{0}_{L}(E)\right]^{-1} u_{L}(E) + \left[P^{0}_{H}(E) - S^{0}_{HH}\right] \left[N^{0}_{H}(E)\right]^{-1} u_{H}(E) = 0_{H} \tag{1-119}$$

$P_H^0(E)$ for $l \to \infty$ diverges, whereas from the previous Wronskian relationship it may be shown that $P_H^0(E)/N_H^0(E)$ is finite. Hence $N_H^0(E)$ will vanish for higher l values. The above equation is thus further reduced to

$$\left[P_L^0(E) - S_{LL}^0\right]\left[N_L^0(E)\right]^{-1} u_L(E) = 0_L \tag{1-120}$$

$$u_H(E) = N_H^0(E)\left[P_H^0(E)\right]^{-1} S_{HL}^0\left[N_L^0(E)\right]^{-1} u_L(E) \tag{1-121}$$

and they thus provide a way of obtaining the higher $\ell, u_H(E)$ in terms of the lower $\ell, u_L(E)$.

For performing the downfolding transformation,an energy dependent value of screening constant $\beta(E)$ is so chosen that $\beta_L \equiv \alpha_L$ and $\beta_H(E) \equiv P_H^0(E)^{-1} = P_H^\alpha(E) + \alpha_H$. The last condition is equivalent to making $P_H^{\beta(E)} \equiv \infty$. The corresponding $RL \equiv H$ channel may be dropped from the MTO envelope set. In fact any channel may be removed by the above procedure. The transformation equation for the structure matrix from some suitable screening transformation is obtained as,

$$S^{\beta(E)} = S^\alpha + S^\alpha\left(\beta(E) - \alpha\right) S^{\beta(E)} \tag{1-122}$$

and with

$$\begin{aligned} \beta_L(E) &= \alpha_L \\ \beta_H - \alpha_H &= P_H^\alpha(E)^{-1} \end{aligned} \tag{1-123}$$

one obtains for the HH block,

$$S_{HH}^{\beta(E)} = S_{HH}^\alpha + S_{HH}^\alpha P_H^\alpha(E)^{-1} S_{HH}^{\beta(E)}$$

or,

$$S^{\beta(E)} = P_H^\alpha(E) F_{HH}^\alpha(E) S_{HH}^\alpha$$

where $F_{HH}^\alpha(E) = [P_H - S_{HH}]^{-1}$,the so called higher block Green function. Similarly we obtain

$$S_{HL}^{\beta(E)} = P_H(E) F_{HH}(E) S_{HL} \tag{1-124}$$

and,

$$S_{LL}^{\beta(E)} = S_{LL} + S_{LH} F_{HH}(E) S_{HL} \tag{1-125}$$

dropping the superscripts α . Utilizing the above equations we obtain ,

$$[P_L(E) - S_{LL} - S_{LH}F_{HH}(E)S_{HL}]\,[N_L(E)]^{-1}\,u_L(E) = 0_L \tag{1-126}$$

$$u_H(E) = N_H(E)F_{HH}(E)S_{HL}\,[N_L(E)]^{-1}\,u_L(E) \tag{1-127}$$

With the upper block being removed ,the lower block envelope set now looks like

$$|K_L^{\beta(E)}\rangle^{\infty} = |K_L\rangle - |J_L\rangle S^{\beta(E)} - |J_H^{\beta(E)}\rangle S_{HL}^{\beta(E)} \tag{1-128}$$

dropping the subscript $\alpha_L = \beta_L$.

For the lower angular momenta block there are two degrees of freedom for the augmentation namely the $|\tilde{J}_L$ and $|\phi_L(E)\rangle$ function, but for the higher block $|K_H\rangle$ has been removed and only the tail function $|\tilde{J}_H^{\beta(E)}\rangle$ is left, which is set proportional to $|\phi_H(E)\rangle$ as,

$$|\tilde{J}_H^{\beta(E)}\rangle = -|\phi_H(E)\rangle N_H(E)/P_H(E)$$

so that the lower block MTO is found to be

$$|\chi_L^{\beta(E)}\rangle^{\infty} = |\phi_L(E)\rangle N_L(E) + |\tilde{J}_L\rangle\left[P_L(E) - S_{LL}^{\beta(E)}\right] + |\phi_H(E)\rangle N_H(E)\,[P_H(E)]^{-1}\,S_{HL}^{\beta(E)}$$

The linear combination of only the lower MTO's will equal the one centre expansion including the higher partial waves when the lower KKR-ASA equations(eq) are satisfied.

To obtain a Hamiltonian form for the downfolding equations the higher block Green function is approximated as,

$$F_{HH}^{\gamma}(E) \cong F_{HH}^{\gamma} - F_{HH}^{\gamma}\frac{E - E_{\nu H}}{\Delta_H}F_{HH}^{\gamma} \tag{1-129}$$

whence the structure function matrix takes the form,

$$S_{LL}^{\beta(E)} \cong S_{LL}^{\gamma} + S_{LH}^{\gamma}\left[F_{HH}^{\gamma} + F_{HH}^{\gamma}\frac{E_{\nu H}}{\Delta_H}F_{HH}^{\gamma}\right]S_{HL}^{\gamma} - ES_{LH}^{\gamma}F_{HH}^{\gamma}\frac{1}{\Delta_H}F_{HH}^{\gamma}S_{HL}^{\gamma}$$

The downfolded KKR-ASA equations now take the well known Hamiltonian form with the Hamiltonian and overlap having the matrix form,

$$H_{LL}^{\beta} = C_L + \sqrt{\Delta_L}\left[S_{LL}^{\gamma} + S_{LH}^{\gamma}\left(F_{HH}^{\gamma} + F_{HH}^{\gamma}\frac{E_{\nu H}}{\Delta_H}F_{HH}^{\gamma}\right)S_{HL}^{\gamma}\right]\sqrt{\Delta_L} \tag{1-130}$$

$$O^{\beta}_{LL} = 1_{LL} + \sqrt{\Delta_L} S^{\gamma} F^{\gamma}_{HH} \frac{1}{\Delta_H} F^{\gamma}_{HH} S^{\gamma}_{HL} \sqrt{\Delta_L} \tag{1-131}$$

A convenient energy independent downfolding representation maybe obtained by setting $\beta_L = \alpha_L$ and $\beta_H \equiv \beta_H(E_{\nu H}) \equiv [P^0_H(E_{\nu H})]^{-1}$ which sets $P^{\beta}_H(E_{\nu H}) \equiv \infty$ i. e. V^{β}_H is chosen at $E_{\nu H}$ whence $F_{HH}(E)$ may be approximated as,

$$F^{\beta}_{HH}(E) \approx \frac{V^{\beta}_H - E}{\Gamma^{\beta}_H} \tag{1-132}$$

Use of the above two equations in KKR downfolded equations would yield a similar set of energy eigenvalue equations with

$$H^{\beta}_{LL} = C_L + \sqrt{\Delta_L} \left[S^{\beta}_{LL} + S^{\beta}_{LH} \left(V^{\beta}_H / \Gamma^{\beta}_H \right) S^{\beta}_{HL} \right] \sqrt{\Delta_L} \tag{1-133}$$

$$O^{\beta}_{LL} = 1_{LL} + \sqrt{\Delta_L} S^{\beta}_{LH} \left(\frac{1}{\Gamma^{\beta}_H} \right) S^{\beta}_{HL} \sqrt{\Delta_L} \tag{1-134}$$

As we mentioned before the downfolding is a very efficient technique to remove ghost bands which occur due to the nearly singular behavior of $H^{(2)}$ or S^{γ} and the resultant long ranged oscillations of the nearly orthogonal orbitals. This occurs when the determinant $\left(\alpha^H\right)^{-1} - (S^0)^{HH}$ vanishes. The damping from other orbitals causes a ghost band and not a divergence. The removal of these orbitals by the downfolding technique is the remedy.

Chapter 2

Ground state properties of alkaline earth chalcogenides

2.1 Introduction

Alkaline - earth chalcogenides are an important group of semiconducting materials. The Beryllium chalcogenides : BeS, BeSe and BeTe are potentially good materials for technological applications. BeS is an interesting material with high hardness and BeTe is a wide gap semiconductor. These materials have application for blue-green laser diodes and laser-emitting diodes (Waag *et al* (1996)). These compounds are difficult to handle experimentally, and theoretically not much work has been done on them (Stukel (1970), Sarma *et al* (1995), Van Camp and Van Doren (1996), Muñoz *et al* (1996a), Luo *et al* (1995), Muñoz *et al* (1996), González-Díaz *et al* (1997)). Few experimental data on their electronic structure are known (Yim *et al* (1972)) and these do not match well with the theoretical results. The elastic properties of these chalcogenides have not been established with any degree of rigour. High pressure phase transitions in these compounds from Wurzite to NiAs structures have been reported. Like the Be chalcogenides, which also go into the Wurzite structure, these show unusual behaviour due to the small core size and absence of occupied p electrons in the bonding process. Unlike the other alkaline earth chalcogenides, the Be compounds are more covalent than ionic with a Phillips ionicity value ranging from 0.169 in BeTe to 0.317 in BeS. These chalcogenides have large bulk moduli and lattice constants that match those of GaAs and ZnSe (Dandrea and Duke (1994), Mensz (1994)).

The Magnesium chalcogenides are wide band - gap semiconductors and are of technological and scientific interest. MgTe is the end point of $Mg_xCd_{1-x}Te$, $Mg_xMn_{1-x}Te$ and $Mg_xZn_{1-x}Te$ ternary systems, all of which are promising optoelectronic materials. MgS and MgSe have the sixfold coordinated NaCl (B1) structure characteristic of ionic compounds like MgO. They transform under pressure to the eight-fold coordinated CsCl (B2) structure . Few theoretical and experimental studies of the electronic properties of MgS and MgSe have been carried out (Peiris *et al* (1994), Duffy *et al* (1995), Van Camp and Van Doren (1997)). MgS undergoes B1 to B2 transition at 175 GPa. Ruoff *et al* (1998) have shown that MgSe undergoes a continuous transformation from B1 to a seven-fold coordinated FeSi (B28) structure starting from 99 GPa and completing at 202 GPa. At 429 GPa it undergoes transition to a orthorhombic distortion of the B2 structure. Experimental studies of MgTe are rarer because of its high hygroscopicity. The low temperature structure of MgTe has had some controversy. Some of the earlier experiments suggested that MgTe crystallizes in the Wurzite structure (Zachariasen (1927), Klemm and Wahl (1951), Parker *et al* (1971)). However, most recent experiments and theoretical calculations predicted that MgTe stabilizes in the NiAs (B8) structure (Li *et al* (1995), Yeh *et al* (1992), Van Camp and Van Doren (1995)). Recently we have carried out theoretical calculations to predict the MgTe stabilizes in the B8 structure at normal pressures and undergoes transitions first to a PH_4I and then to a B2 structure at pressures higher than 60 GPa (Basu Chaudhuri *et al* (1999)).

CaS is known to be efficient in cathode, X-ray and radio luminescence, with a bright response to excitation, a high storage power and a bright infra-red flash. Luo *et al* (1994) have carefully studied the behaviour of the Calcium chalcogenides. The chalcogenides are electronically very similar to CaO and crystallize in the B1 phase. CaS and CaSe transform into the B2 phase at around 40 and 38 GPa respectively. CaTe first transforms into a mixture of the B1 and MnP phases at 25 GPa and finally into the B2 phase at 33 GPa.

The Strontium and Barium chalcogenides show behaviour very similar to the Calcium chalcogenides. There has been rather more and extensive experimental and theoretical investigations into these compounds, both in the study of pressure induced B1 to B2 transitions and pressure induced semi-conductor/metal transitions

(Luo *et al* (1994), Zimmer *et al* (1985), Syassen (1985), Weir *et al* (1986), Cervantes and Williams (1998), Kalpana *et al* (1994)).

Theoretical study of the optical properties of alkaline-earth chalcogenides have been carried out by Stepanyuk and coworkers (Stepanyuk *et al* (1989a), Stepanyuk *et al* (1989b)). The authors have shown the importance of the energy dependence of the optical transition matrix element for accurate descriptions of the permittivity. The calculations were based on the LAPW technique.

The earlier theoretical studies used a variety of techniques : from the Linear Combination of Atomic Orbitals (LCAO) and empirical tight-binding (E-TB) to the whole gamut of local density approximation (LDA) based methods including the pseudo-potential, the linearized augmented plane wave (LAPW) and the linearized muffin-tin orbitals (LMTO) techniques. In this work we shall use the same theoretical technique : namely the LDA-based tight-binding LMTO (TB-LMTO), to study the whole series of chalcogenides.

The aim of this work is not to focus on any specific property of a particular compound, but rather to study the trends and variations across the whole series of compounds and what these trends reveal about the electronic and elastic properties of these class of materials.

The local density approximation (LDA) of the density functional (DF) formalism (Hohenberg and Kohn (1964)) provides a rather accurate description of the ground state properties of the elementary *spd* bonded metals. Some aspects of the description are, nevertheless, less satisfactory. The usual practice had been to use within the LDA approximation, the exchange-correlation suggested by von Barth and Hedin (von Barth and Hedin (1972)). In this approach, for instance, the cohesive energy is too large, in particular for *3d* metals, where the errors can be a few eV. The lattice parameter is also underestimated and for *3d* metals. An early attempt to improve the LDA approximation was the gradient expansion approximation (GGA). Calculations for atoms and a jellium surface (Langreth and Perdew (1977)) show, however, that the GGA does not improve the LDA approximation, if the calculated ab - initio coefficients of gradient correction (Rasolt *et al* (1979), Rasolt and Geldart (1980)) are used. The errors in the GGA have been studied by Langreth and Perdew (1977), Langreth and Perdew (1980) and by Perdew (1986).

Based on this analysis Langreth and Mehl (1983) and Hu and Langreth (1986), as well as Perdew (1986) and Perdew and Wang (1986) (PW), have proposed modified gradient expansions for the exchange - correlation energy.

The LMH and PW functionals have only been tested in rather few cases, but they give encouraging results for the ground state properties in these cases. For atoms it was found that both total energies and removal energies are improved in the LMH functional compared to LDA approximation (Langreth and Mehl (1983), Hu and Langreth (1986)). The PW functional gives a further improvement in the total energy of atoms (Perdew (1986), Perdew and Wang (1986)). The binding energies of the first row diatomic molecules are improved by both functionals. In the study of the band structure of V and Cu, it was found that the LMH potential gave an improvement in the Fermi surface for V but not for Cu. The deviation of the band structure from photo-emission results also increased somewhat for Cu. The ground state properties were not studied. For Si, one finds a similar error (factor 2) in the band gap as in the LSD approximation, while the cohesive energy (4.89 eV) was also improved over the LSD results (5.19 eV) compared with experiment (4.63 eV).

The usefulness of LMH and PW functionals relative to standard vBH-LDA has remained a matter of controversy. It has thus motivated us to compare the use of the different exchange-correlation functionals in our systematic study of ground state properties of alkaline earth chalcogenides. We shall obtain, in addition to the band structure and the density of states, the equilibrium lattice parameter and the bulk modulus. We find that in most cases the LMH functional gives somewhat better results than the vBH-LDA.

2.2 Results and Discussion

Not much work has been carried out on the Beryllium chalcogenides. Luo *et al* (1995) report experimental indication that BeSe and BeTe undergo a first-order structural phase transition under pressure from a zinc-blende to a NiAs structure. This is unique among alkaline-earth chalcogenides (II-VI compounds), since most of them show a transition between NaCl and CsCl structures (Weir *et al* (1986)). In

addition these compounds have wide band gaps and high bulk moduli. Experimental results on BeS is not available. Muñoz *et al* (1996) have carried out theoretical band-structure investigations on BeS, BeSe and BeTe using an ab-initio pseudo-potential technique. They had used the Ceperly-Alder (Ceperly and Alder (1980)) exchange-correlation and a norm conserving, non-local pseudo-potential within the Kerker (Kerker (1980)) scheme.

The top panel of figure (2.1) shows the band structure of the Beryllium chalcogenides. All three are indirect band-gap semiconductors with the highest occupied band at the Γ-point (top of the valence band is chosen to be the zero of our energy in all the figures), and the lowest unoccupied band at the X point. All three are 'large' gap semi-conductors. BeS has the largest gap of around 0.3 Ryd (compare this with the band gap of 0.074 Ryd for Si). This decreases for BeSe and BeTe, which has a smallest gap among the series of around 0.15 Ryd.

The figure (2.2) shows the density of states for the Beryllium chalcogenides, together with the partial density of states for Be and the chalcogen X in BeX. The features come out very clearly in all three cases. The lowest lying s-like feature going from just below -1 Ryd below the top of the valence band for BeS to just above -1Ryd for BeTe arises mostly from the s-electrons of Be. This is also clear from the band structures shown in figure (2.1). The bonding-antibonding states around the band gap are p-like and are strongly indicative of a predominantly covalent bonding in these chalcogenides.

In the next step we have minimized the total energy for a variation of the lattice parameter using both the von Barth-Hedin (VBH) and the Langreth-Mehl-Hu (LMH) forms of the exchange-correlation. The bulk modulus is then given by the expression :

$$B_0 = -V \left.\frac{d^2E}{dV^2}\right|_{V_0}$$

The results for the equilibrium lattice parameter and the bulk moduli are shown in table (2.1). The VBH gives lattice parameters *lower* than the experimental value while the LMH overestimates them. The lattice parameters increase as we go from BeS to BeTe, indicating that the covalent bonding is the strongest in the Sulphide and weakest in the Telluride. This is reflected in the decreasing bulk moduli as we

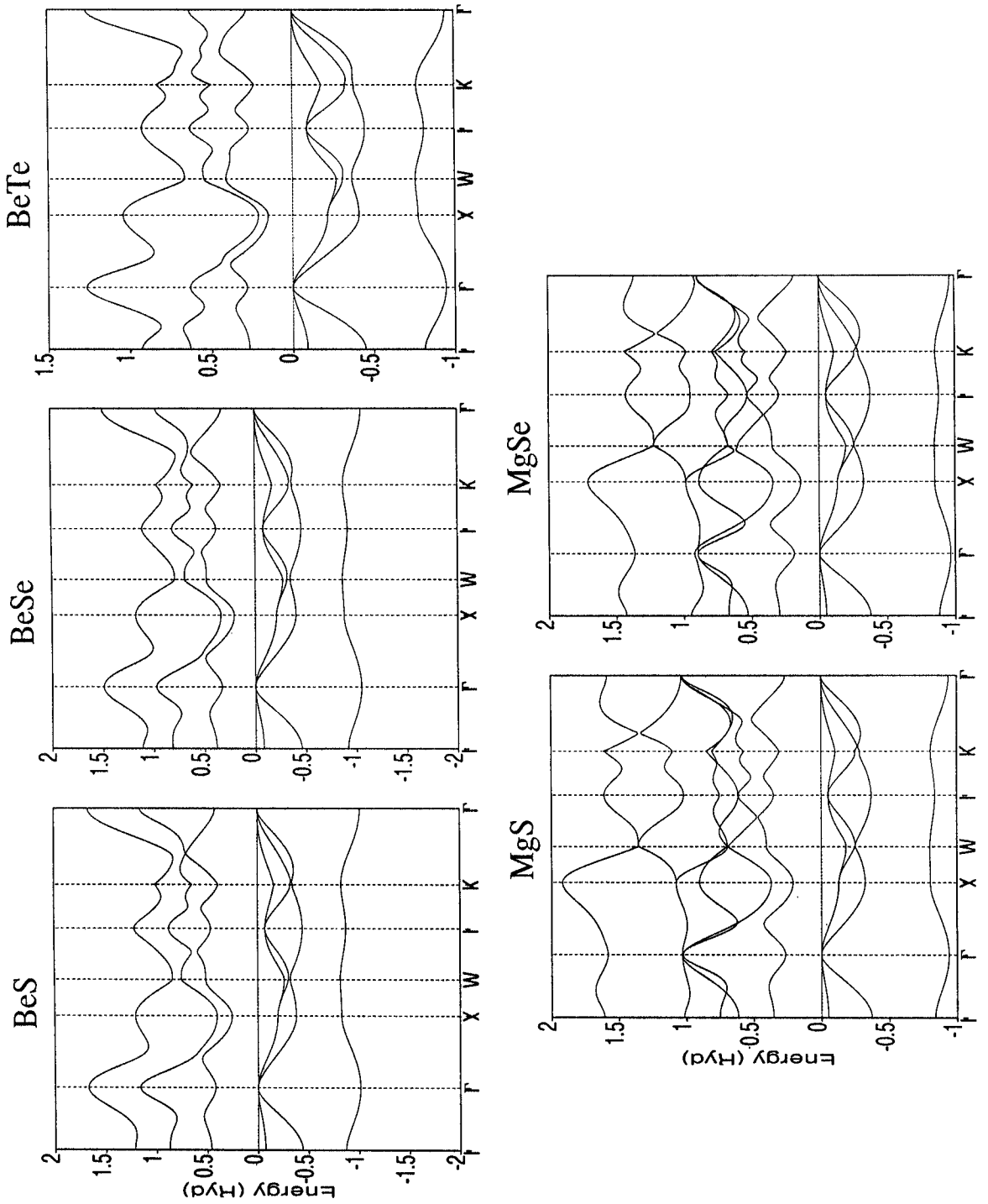

Figure 2.1: The band structures of Be and Mg chalcogenides

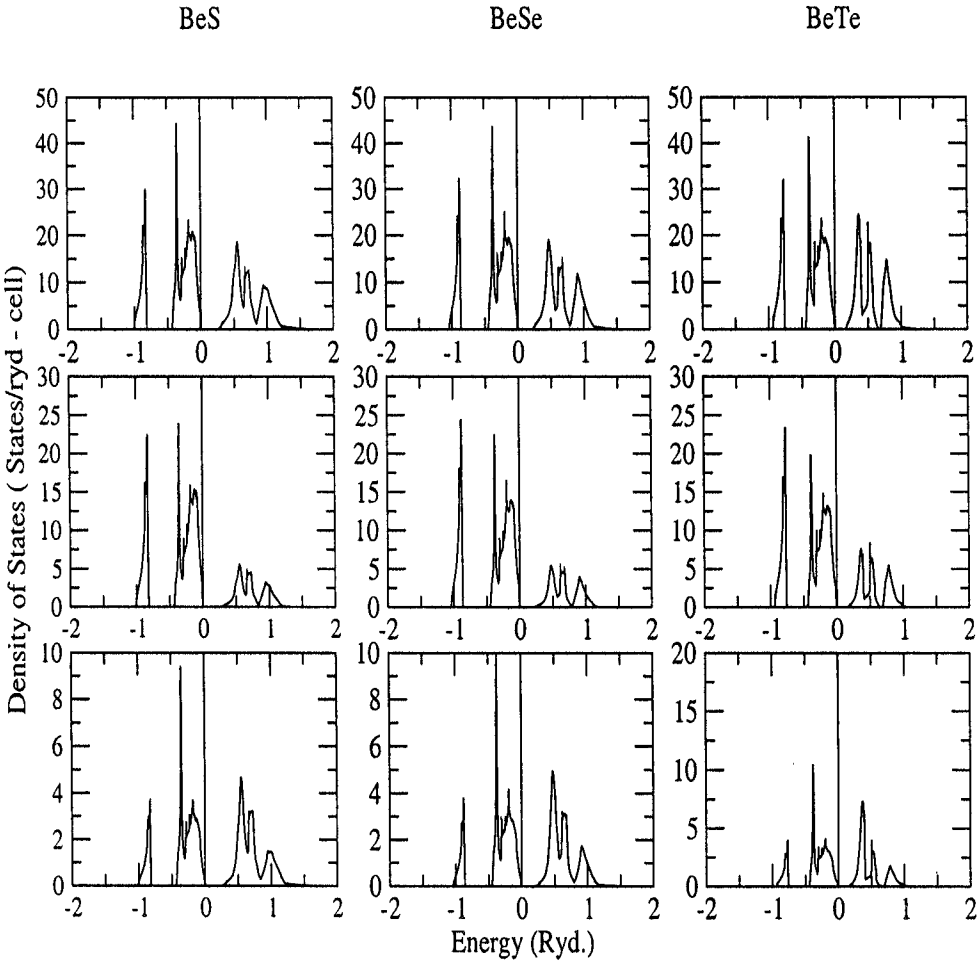

Figure 2.2: (Top) Density of states for BeX (Middle) Partial density of states for the chalcogen X in BeX (Bottom) Partial density of states for Be in BeX

go from BeS to BeTe. For the bulk moduli, the VBH seems to give better estimates as compared with the more reliable of the experimental results.

Unlike the Beryllium chalcogenides, the MgS and MgSe usually crystallize at normal pressures in the rock-salt structure and goes over to the CsCl structure at higher pressures. This is more characteristic of the alkaline-earth chalcogenides. MgTe has a more complicated behaviour and we shall study this compound in detail on its own in the next chapter. Earlier work on these compounds have been by Van Camp and Van Doren (1996) and Van Camp and Van Doren (1997) using a screened pseudo-potential method, with pseudopotentials of the form proposed by Kleinman and Bylander (1982). Our results are quoted here. Figure (2.1) shows the band structure of MgS and MgSe in the rock-salt structures. In comparison with the Beryllium compounds, the valence band structure is not very different. The density of states, shown in figure (2.3) also confirms this. A careful study of the states straddling the Fermi-energy show that unlike the predominantly covalent Beryllium compounds, these states are not equi-weighted bonding-antibonding type states. The ionicity of the Mg compounds are higher, the asymmetric ionic like bonding states are more in evidence. MgS and MgSe are both indirect band gap semiconductors with a Γ-X gap of 0.125 Ryd and 0.115 Ryd respectively. For MgSe this matches well with the 0.11 Ryd gap estimated by Van Camp and Van Doren (1997). It should be noted that all these calculations are LDA based, so underestimate the band gaps. But this is a consistent feature throughout the whole series of materials.

Calcium chalcogenides form a closed shell ionic system which crystallizes in a rock-salt structure. The band structure shown in the top panel of figure (2.4) indicates again that the valence bands have no d-like character and is predominantly *sp*-like.

The partial density of states on Ca and X, shown in figure (2.5) now clearly indicate the asymmetric ionic-bonding states straddling the Fermi-energy. For Ca compounds and others that follow, the table (2.1) indicates that the LMH form of exchange-correlation gives much better estimates of the lattice parameters and the bulk moduli. It is also interesting to note that with increasing ionicity between BeX to MgX to CaX chalcogenides, the bulk moduli decreases : for example, 1048 kbar

Compound	$B_0(VBH)$ *kbar*	$B_0(LMH)$ *kbar*	$B_0(expt.)$ *kbar*	$a(VBH)$ *a.u.*	$a(LMH)$ *a.u.*	$a(expt.)$ *a.u.*
BeS	1047.9	979.8	-	8.921	9.224	9.197[n]
$BeSe$	854.4	788.8	920[a]	9.536	9.827	9.711[a]
$BeTe$	645.6	604.4	670[a]	10.597	11.0004	10.618[a]
MgS	839.1	757.3	660 ± 17[b]			9.829[b]
			798 ± 37[c]	9.478	9.857	9.832[c]
$MgSe$	701.1	636.0	525.0[d]	10.048	10.456	10.332[d]
CaS	694.6	608	640[e]	10.431	10.757	10.754[e]
$CaSe$	580.1	506.1	510[e]	10.848	11.239	11.183[e]
$CaTe$	438.8	389.0	420± 20[e]	10.490	11.940	12.000[e]
BaS	494.5	432.7	394.2[f]	12.049	12.132	12.074[f]
$BaSe$	473.8	410.3	434± 26[g]	12.438	13.061	12.463[h]
$BaTe$	333.3	295	294[i]	13.122	13.613	13.242[i]
SrS	611.3	590.6	580[j]	11.189	11.530	11.388[j]
$SrSe$	518.6	484.4	450[k]	11.519	11.807	11.784[k]
$SrTe$	400.8	365.3	400[m]	13.192	13.657	12.588[m]

Table 2.1: The calculated bulk modulus(B_0) in *kbar*, lattice parameters (a) in $a.u.$ for alkaline earth chalcogenides using VBH and LMH

---

[a] Reference Luo *et al* (1995)

[b] Reference in Yeh *et al* (1992) A. Chizmeshya (private communication)

[c] Reference Peiris *et al* (1994)

[d] Reference Ruoff *et al* (1998)

[e] Reference Luo *et al* (1994)

[f] Reference Yamoka *et al* (1980)

[g] Reference Ruoff and Grzybowski (1985)

[h] Reference Grzybowski and Ruoff (1983)

[i] Reference Grzybowski and Ruoff (1984)

[j] Reference Syassen (1985)

[k] Reference Luo *et al* (1994)

[m] Reference Zimmer *et al* (1985)

[n] Reference in *Semiconductors other than Group IV elements and III-V compounds*, edited by O. Madelung, *Data in Science and Technology series* **VIII** (Springer Verlag, Berlin, 1992)

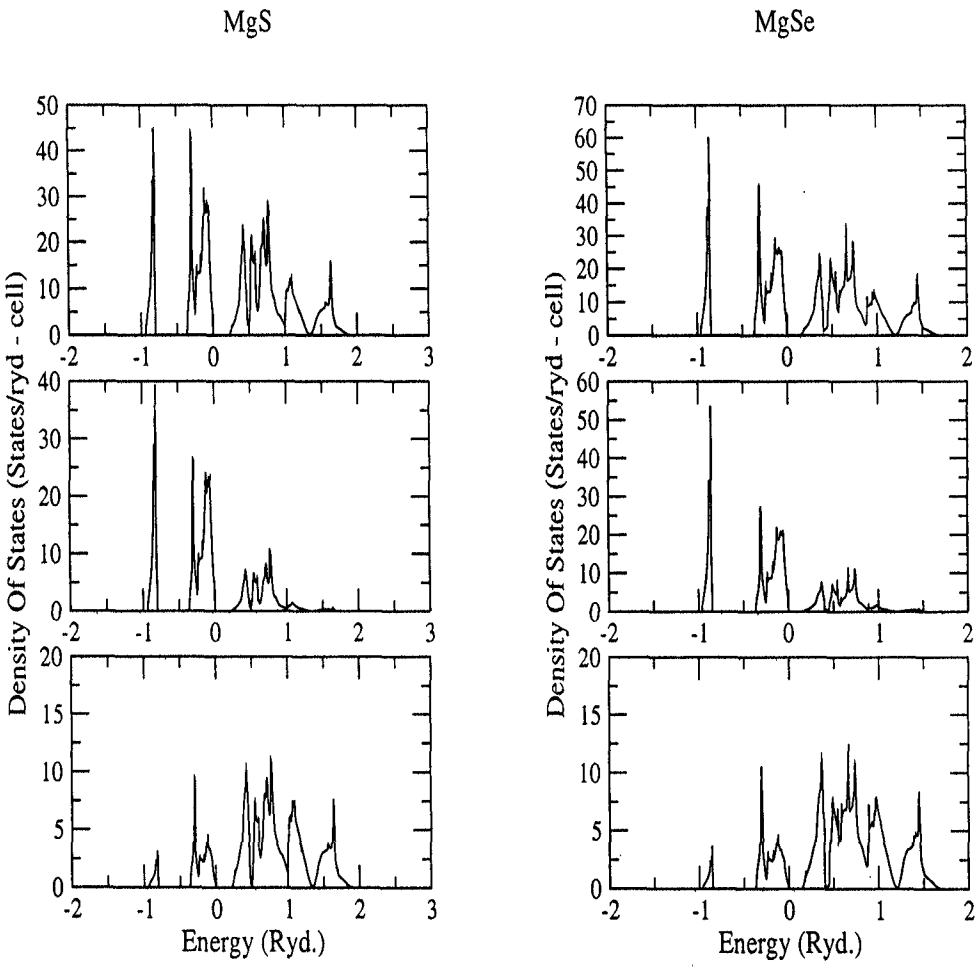

Figure 2.3: (Top) Density of states for MgX (Middle) Partial density of states for the chalcogen X in MgX (Bottom) Partial density of states for Mg in MgX

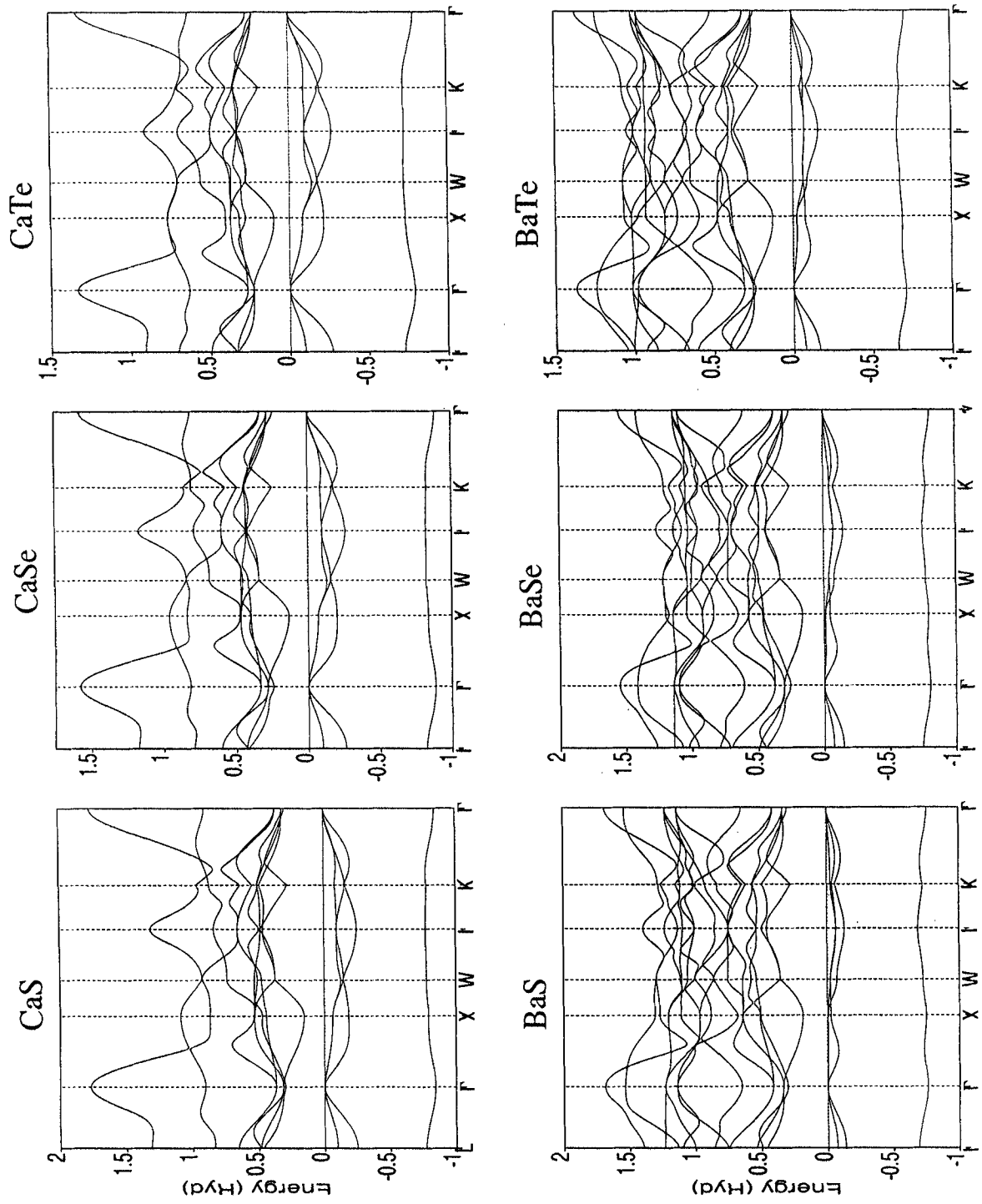

Figure 2.4: The band structures of Ca and Ba chalcogenides

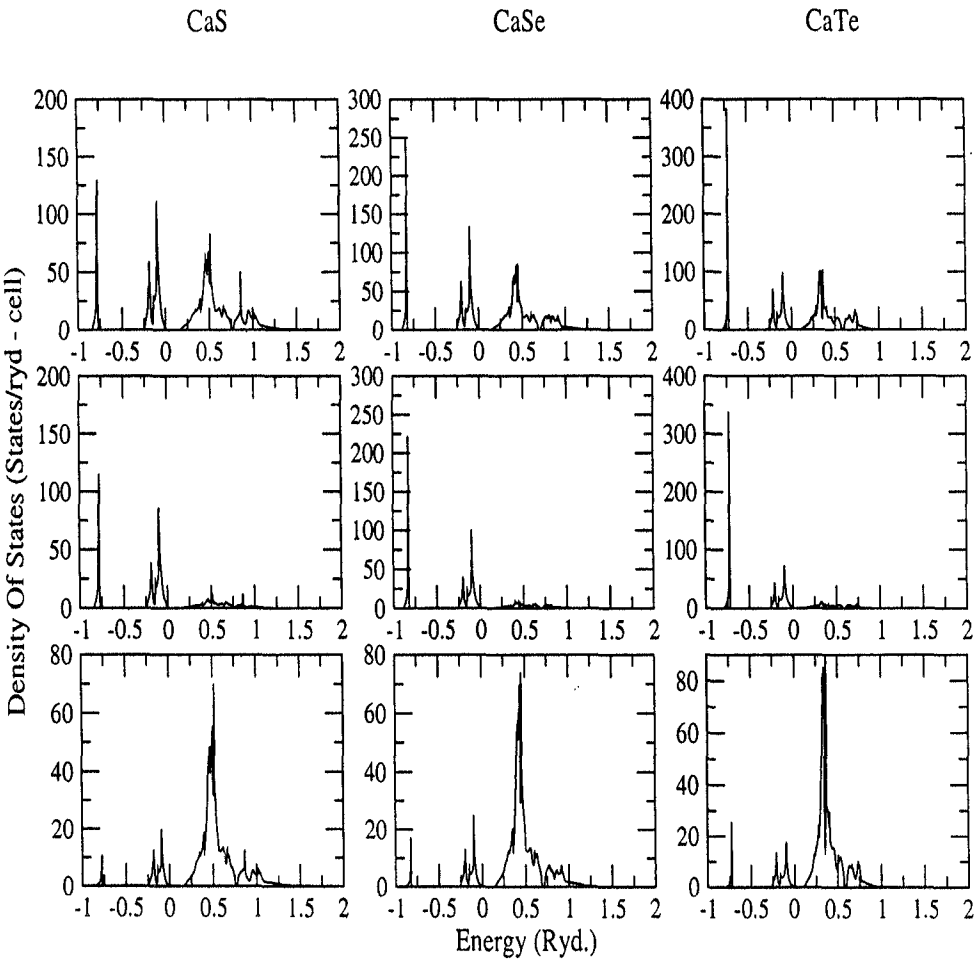

Figure 2.5: (Top) Density of states for CaX (Middle) Partial density of states for the chalcogen X in CaX (Bottom) Partial density of states for Ca in CaX

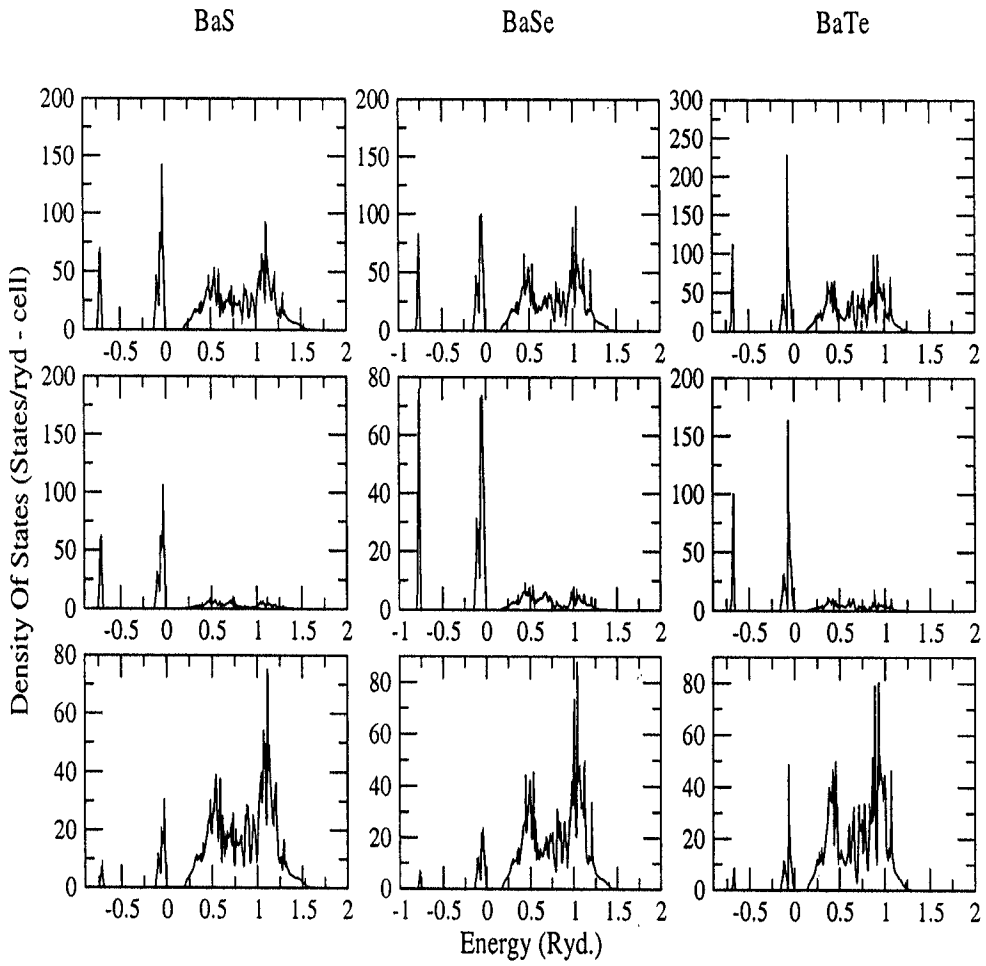

Figure 2.6: (Top) Density of states for BaX (Middle) Partial density of states for the chalcogen X in BaX (Bottom) Partial density of states for Ba in BaX

for BeS, 839 kbar for MgS and 695 kbar for CaS. This is what we should expect from the naive idea that covalent bonding is the strongest type of bonding in solids. These bulk moduli are in good agreement with the experimental results (as shown in table (2.1).

The band structure of the Ca and Ba chalcogenides (figure 2.4) show another feature of the series as compared to Be and Mg compounds. The bonding state immediately below the Fermi energy becomes narrower. This is also reflected in its narrow and high nature in the density of states (figure 2.6). This feature is also reflective of the transition of a wider covalently bonded bonding-state to to narrower ionic bonding state. Otherwise, the nature of the Barium compounds are rather similar to the Calcium chalcogenides. The band gaps are around 0.1 Ryd for BaS, 0.07Ryd for BaSe and 0.06 Ryd for BaTe. These agree well with LPAW calculations on BaSe and BaTe by Wang *et al* (1985) as well as ASW calculations by Carlsson and Wilkins (1984) and LMTO calculations of Kalpana *et al* (1994).

The band structure and partial density of states for the Strontium chalcogenides are shown in figures (2.7)-(2.8). The ionicity increases, bonding becomes weaker leading to lower bulk moduli, the band gap diminishes. This makes it possible to metalize some of these compounds under pressure (Kalpana *et al* (1994)). For most of these compounds the bulk modulus estimates are better with the LMH exchange-correlation rather than in VBH. Though it appears that the VBH exchange-correlation is better for estimates of the lattice parameter, this is doubtful, for LDA based calculations should overestimate the lattice parameter, which LMH consistently does. Our view is that the LMH is a more reliable approximation for the exchange-correlation as compared with the VBH.

The variation of the total energy with the lattice parameter showing minimum at the equilibrium lattice parameter is shown in the figures (2.11). The curvature at the minimum is related to the bulk modulus through the relation described earlier in the chapter. The variation of the bulk moduli across the compounds is shown in table (2.1). The general trend is clear : bulk modulus decreases as we go from BeX to SrX (X is any S, Se or Te) and also as we go from YS to YTe (Y is any Be,Mg,Ca,Ba or Sr). This is consistent with the decrease of bonding strength and increase of equilibrium lattice parameter. All the compounds are indirect (Γ-X) gap

semiconductors. The band gap also decreases as we go from Be to Sr and in a single alkaline-earth compound from S to Te. Of all these compounds MgTe has a rather different behaviour, which we shall discuss in the following chapters.

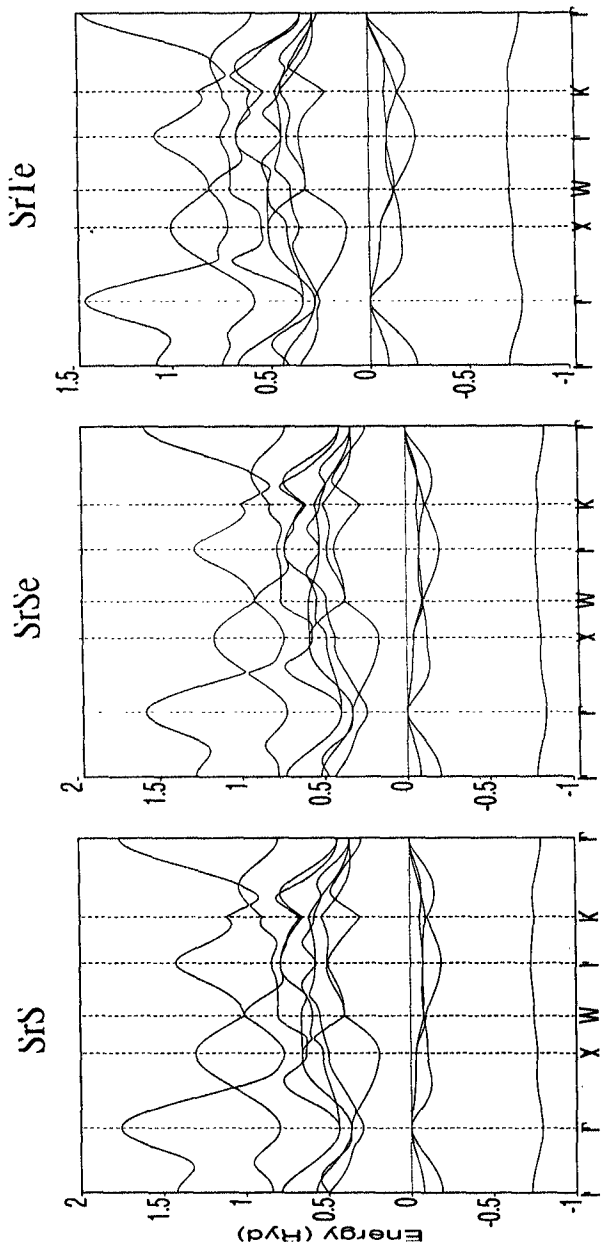

Figure 2.7: The band structures of Sr chalcogenides

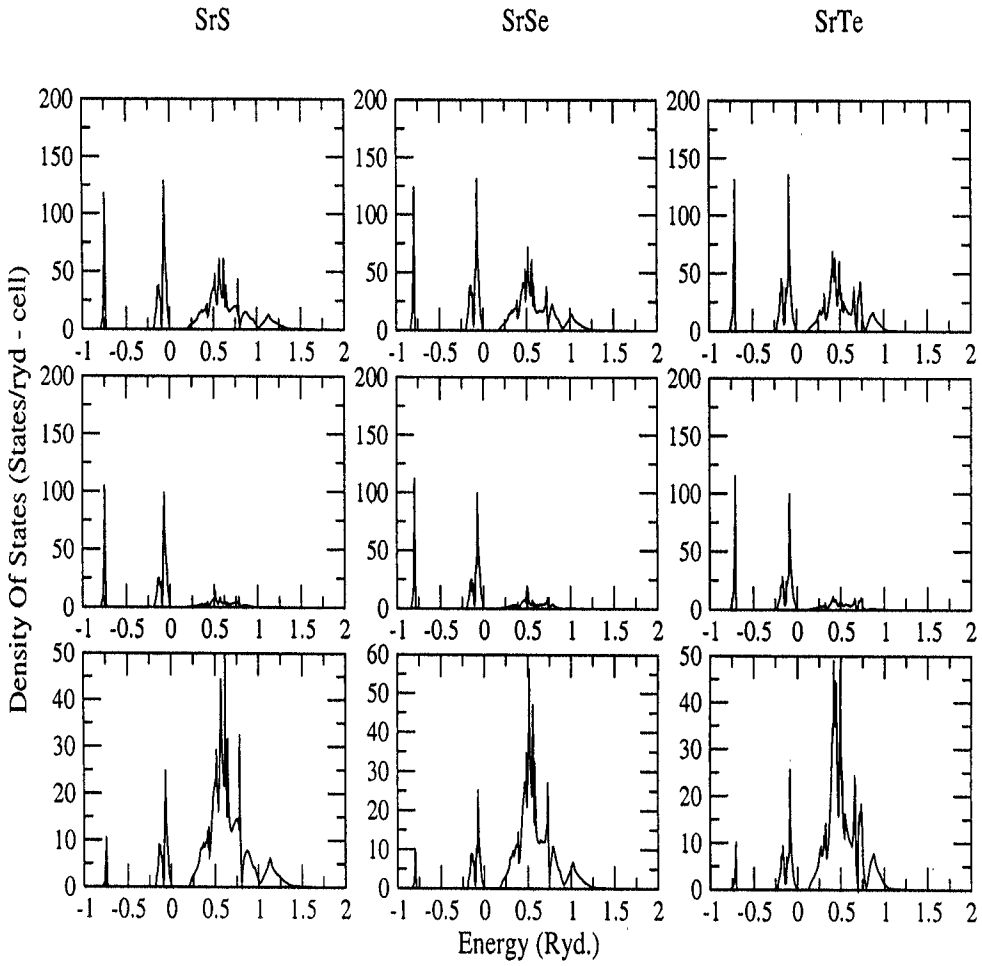

Figure 2.8: (Top) Density of states for SrX (Middle) Partial density of states for the chalcogen X in SrX (Bottom) Partial density of states for Sr in SrX

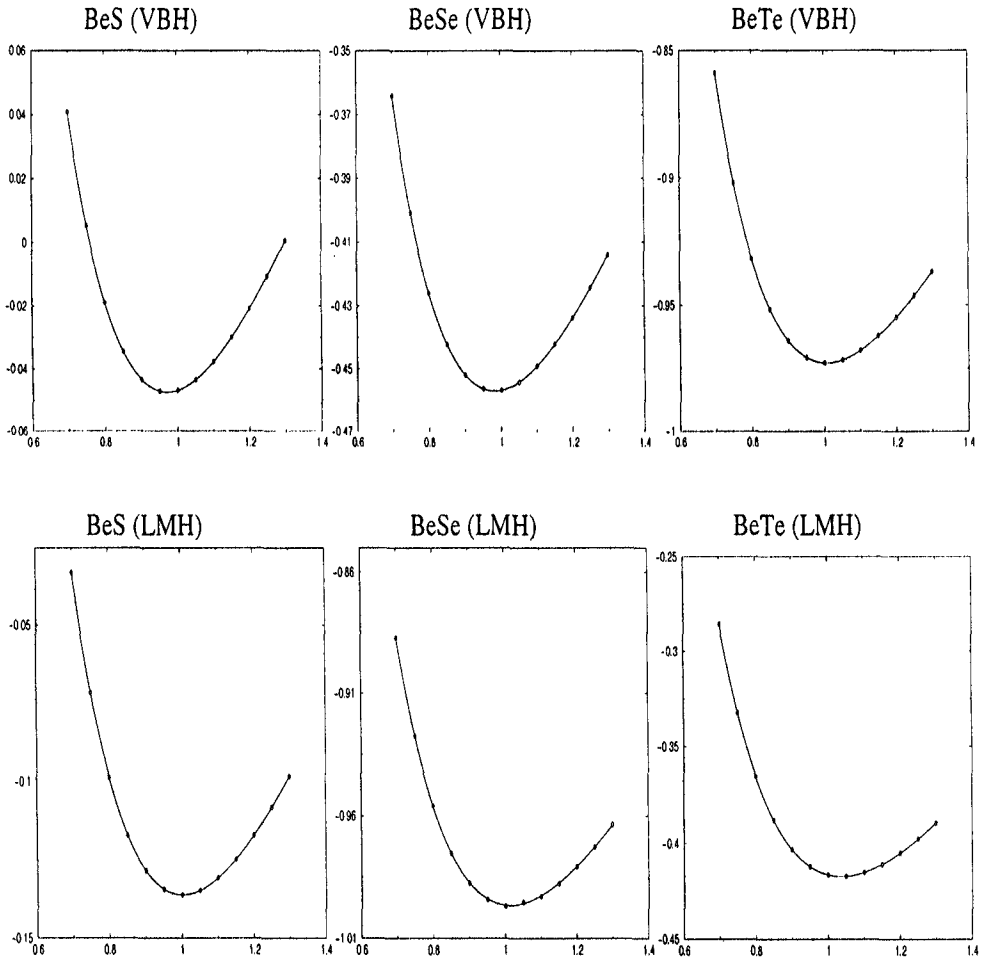

Figure 2.9: Total energy variation with reduced volume for BeX: y-axis shows total energy in Ryd. (with a suitable chosen zero) and x-axis shows reduced volume in units of the equilibrium cell volume (V/V_0)

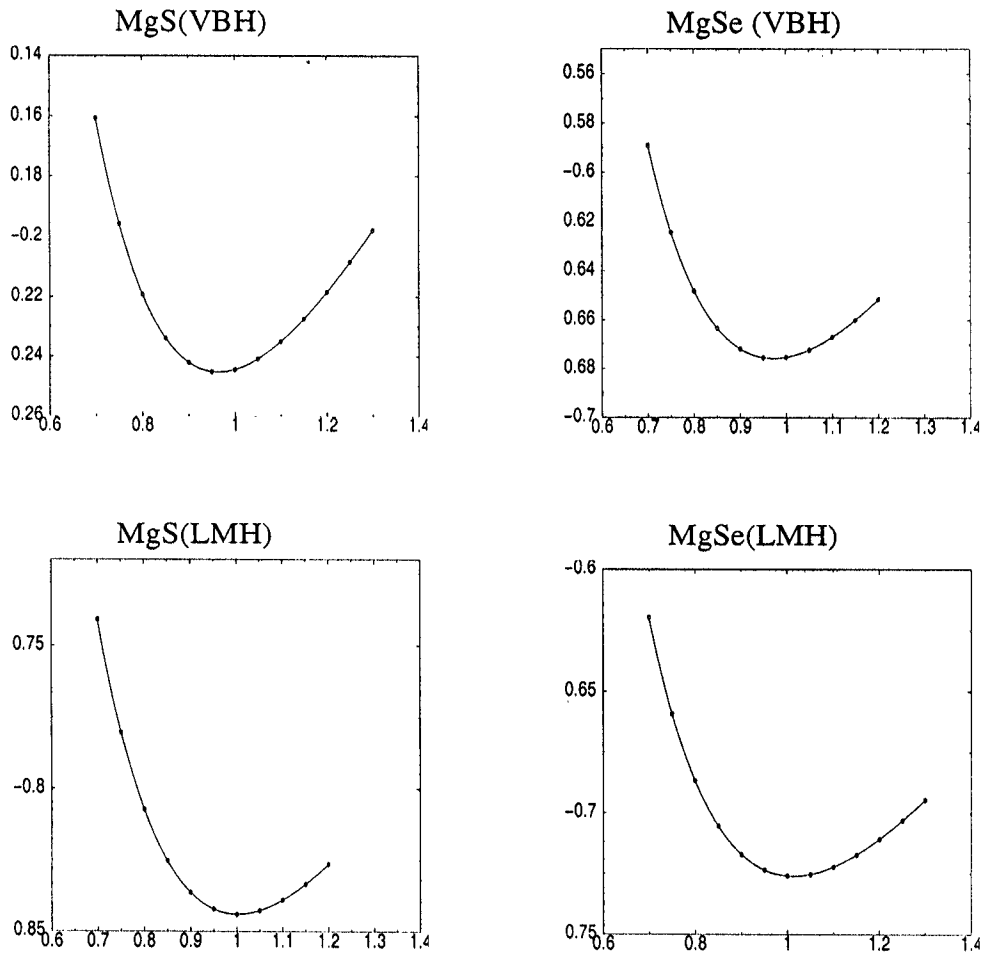

Figure 2.10: Total energy variation with reduced volume for MgX: y-axis shows total energy in Ryd (with a suitable chosen zero) and x-axis shows reduced volume in units of the equilibrium cell volume (V/V_0)

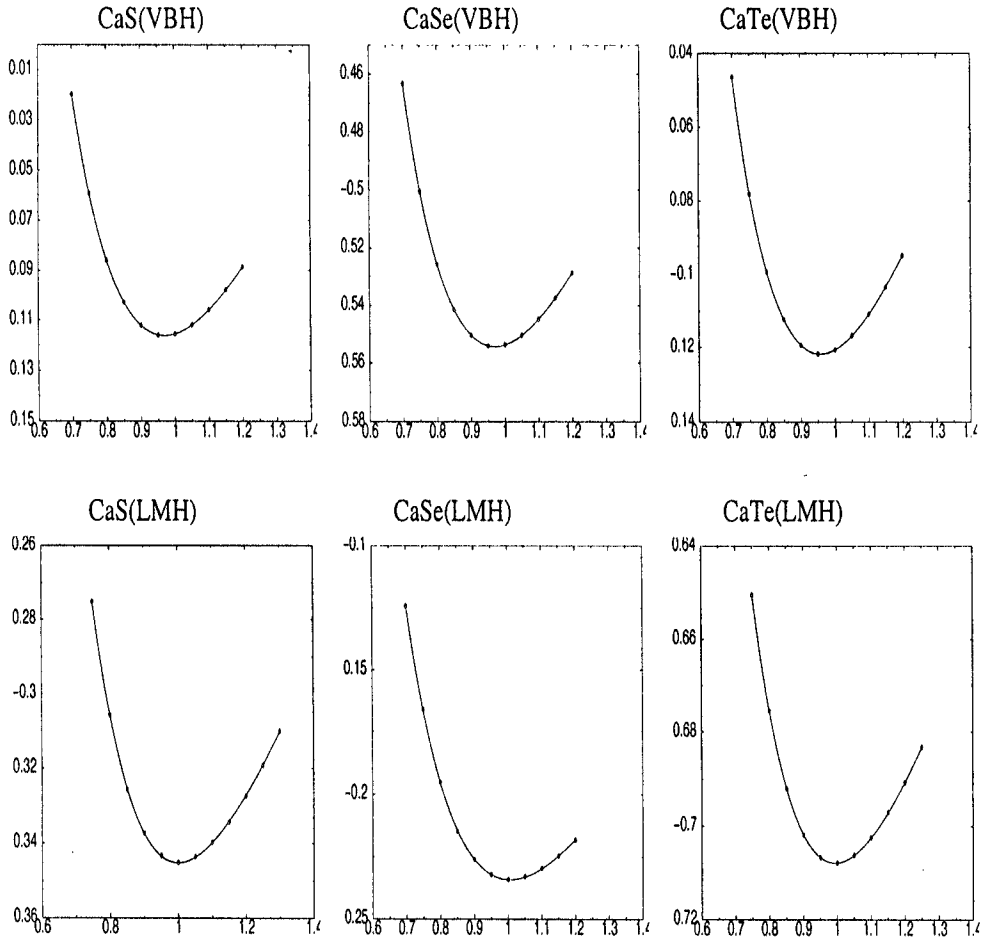

Figure 2.11: Total energy variation with reduced volume for CaX: y-axis shows total energy in Ryd (with a suitable chosen zero) and x-axis shows reduced volume in units of the equilibrium cell volume (V/V_0)

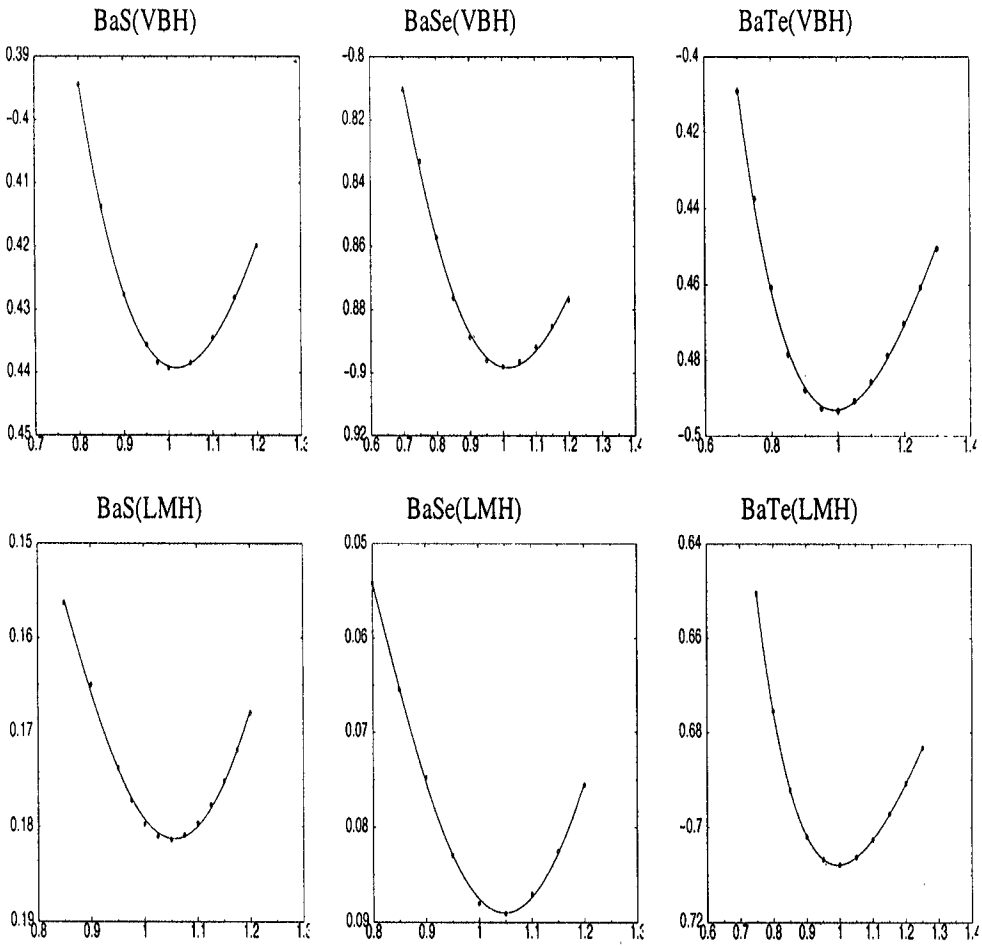

Figure 2.12: Total energy variation with reduced volume for BaX: y-axis shows total energy in Ryd (with a suitable chosen zero) and x-axis shows reduced volume in units of the equilibrium cell volume (V/V_0)

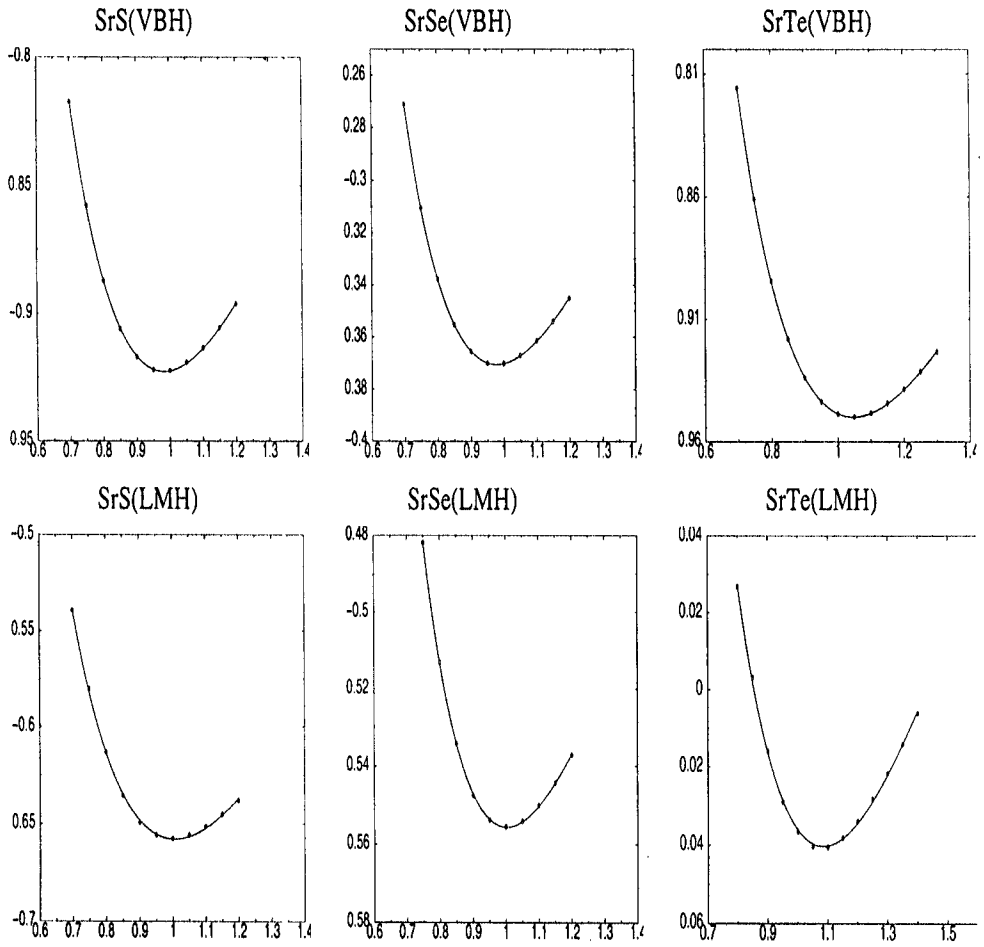

Figure 2.13: Total energy variation with reduced volume for SrX: y-axis shows total energy in Ryd (with a suitable chosen zero) and x-axis shows reduced volume in units of the equilibrium cell volume (V/V_0)

Chapter 3

Study of pressure induced phase transition in MgTe

3.1 Introduction

In the earlier chapter we have discussed the high pressure behaviour of alkaline-earth chalcogenides RX ($R = Be, Mg, Ca, Sr, Ba$; $X = S, Se, Te$). Under normal conditions these compounds crystallize in the rocksalt structure (B1) with sixfold coordination. Chalcogenides of Ca, Sr and Ba undergo structural phase transition from B1 to B2 under pressure. Exceptions are the Be chalcogenides and MgTe. Recently, pressure induced phase transition from the B3 to the $NiAs$ (B8) has also been observed for BeX (Luo *et al* (1994)), MgS (P_c=37.7 GPa) and MgS (Kalpana *et al* (1994)) (P_c=31.7 GPa). MgTe is the only member of the series which seems to behave differently. Further, we note that while CaO shows B1 to B2 structural transition at a relatively low pressure of 61 GPa (Jeanloz *et al* (1979)) and CaTe transforms from the B1 to the B2 phase at even lower pressures of 33 GPa (Luo *et al* (1994)), MgO is stable in the B1 structure even up to 600 GPa (Jackson and Gordon (1988)).

It should be interesting to study the high pressure behaviour of MgTe so that it may help us to understand whether the anomalously high transition pressure

[1]The contents of this chapter has been published in Basu Chaudhuri, Pari, Mookerjee and Bhattacharya *Phys. Rev.* **B60** 11846 (1999)

associated with MgO is also followed by MgTe.

Experimental structural studies on MgTe are less frequently reported mainly because of its high hygroscopicity (Kuhn *et al* (1971)). The pioneering works by Zachariasen (Zachariasen (1927)) and Klemn and Wahl (Klemm and Wahl (1951)) showed that MgTe crystallizes (high temperature phase) in the hexagonal wurtzite structure which has been widely accepted and experimentally reproduced (Kuhn *et al* (1971), Parker *et al* (1971)). But recently the first principles local-density formalism (LDF) based calculations on MgTe by Yeh *et al* and Van Camp and Van Doren (1996) predicted the ground state of MgTe to be B8. Recent high pressure energy-dispersive X-ray diffraction ($EDXD$) experiments by Li *et al* (1995) on MgTe in a diamond anvil cell indicated pressure induced structural phase transition from the wurtzite to the B8 structure at pressures of $\approx$ 1-3.5 GPa and also suggested that the thermodynamic stable phase at normal temperature and pressure to be B8 in support of the earlier theoretical predictions (Yeh *et al* (1992), Van Camp and Van Doren (1996)). They have also suggested that the system may go from the B8 phase to the B2 or the PH_4I and then to the B2 structure at a pressure much higher than 60 GPa. However, no theoretical calculations have been performed for these structures so far. The work presented in this chapter has been aimed to understand the pressure behaviour of MgTe and identify the pressure induced structural phase transformations.

In this chapter we shall examine behaviour of MgTe under pressure using the tight binding linear muffin-tin orbital ($TB\text{-}LMTO$) method (Andersen and Jepsen (1984)). The calculations have been performed in the wurtzite, B8, B2 and PH_4I structures. Our calculations also show that the ground state phase of MgTe to be B8. Our results for the B8 and wurtzite are in excellent agreement with the earlier theoretical calculations. Our calculations indicate that MgTe is semi-conducting in the B8 and wurtzite phases and metallic in the other two phases. The calculated semi-conducting gap (E_g) for the wurtzite structure at its equilibrium is in good agreement with the earlier results (Chadi (1994), Parker *et al* (1971)) and however we find the gap to be very small for the B8 phase. Interestingly we have observed, for the first time, transition from the B8 to the B2 structure with pressure.

3.2 Results and Discussion

We have resorted to the *TB-LMTO* method within the framework of density functional theory(*DFT*) (Hohenberg and Kohn (1964)) in its local density approximation (*LDA*) (Kohn and Sham (1965)) to obtain the electronic structure, total energies and its variation with volume of MgTe in the wurtzite, B8, B2 and PH_4I phases. The exchange-correlation potential has been chosen to be that of the von Barth and Hedin scheme (von Barth and Hedin (1972)). We have taken the ground state volume V_0 to be 674.1797 $(a.u.^3)$ for all the structures under consideration and c/a=1.623, 1.633, 0.729 for B8, wurtzite and PH_4I structures as a guideline from Van Camp and Van Doren (1996).

To understand the ground state properties of MgTe in the stable phase and also identify whether there is a pressure induced structural phase transition as well as an insulator-metal transition as suggested by Li *et al* (1995), we have performed electronic structure and cell volume variation of the total energy calculations for the wurtzite, B8, B2 and PH_4I phases.

The calculated total energy/primitive cell as a function of reduced volume for the B8, wurtzite, B2 and PH_4I phases are shown in figure 3.1. The total energies in these phases were fitted to the Birch equation of state (Birch (1978)) to obtain the pressure-volume relation ($P = dE/dV$). Figure 3.2 represents the variation of P with V/V_0.

The structural phase stability is determined through the Gibb's free energy (Born and Huang (1954)) ($G = E_{tot} + PV + TS$). As our calculations are done at temperature $T = 0$, G and the enthalpy (H) are the same. Thus a stable structure at a given P corresponds to a minimum value in H and the transition pressure (P_c) is calculated from the crossing point of the enthalpies for the two phases. The calculated equilibrium lattice parameters in different phases, cohesive energy (E_{coh}) being the energy required to form the solid from the constituent atoms, B_0, P_c and the volume reduction at the transition from the B8 to B2 phase are given in Table I and are compared with the earlier literature.

From figure 3.1, it is clear that the B8 phase is the stable ground phase of MgTe, in very good agreement with the earlier theoretical and experimental results (Yeh

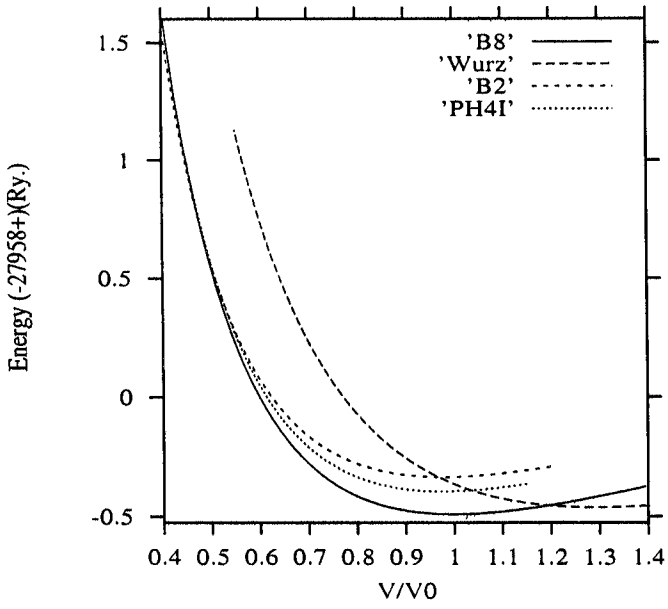

Figure 3.1: Variation of the total energy/primitive cell as a function of the reduced volume for MgTe in the wurtzite, B8, B2 and PH_4I phases. The y-axis represents energy with respect to a reference value -27958 *Ryd*.

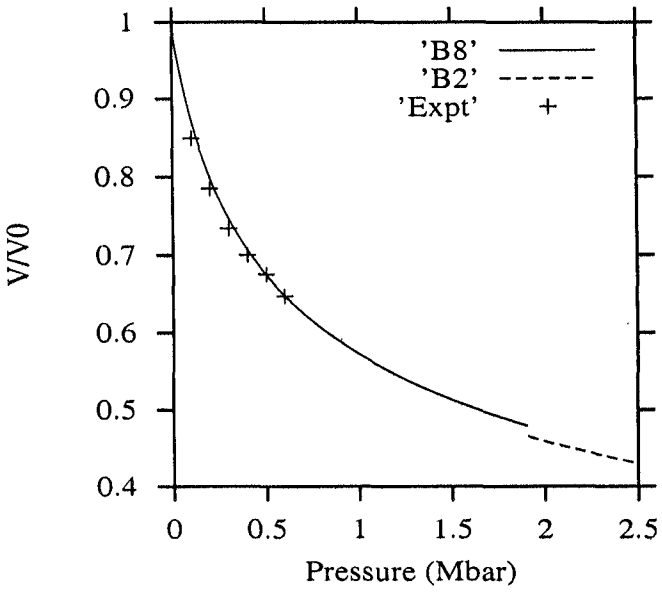

Figure 3.2: The variation of pressure as a function of reduced voulme for the B8 and B2 phases.

et al (1992), Van Camp and Van Doren (1996), Li *et al* (1995)).

It can be seen from the figure 3.1 that the wurtzite phase stabilizes at $V/V_0 > 1.293$, remains to be stable only at the expanded lattice ($V/V_0 > 1.2$), and structural transition from this phase to the B8 occurs just below $V/V_0 = 1.2$, in agreement with the prediction of Li *et al* (1995). It is to be noted that Van Camp and Van Doren (1996) have done the calculations for the structures mentioned above up to only a reduced volume of 0.60. In the low V/V_0 regime, the total energy of Ph_4I is slightly higher than that of B8, but lower than the other two phases. However, just before the B8 to B2 phase transition, the B2 phase becomes lower in energy than that of the Ph_4I. We have calculated the structural transition pressure, from the B8 to B2 phase as P_c=190.8 GPa corresponding to a reduced volume of 0.479 in the B8 phase, where the enthalpy of the both phases are the same. This is consistent with the experimental predictions (Li *et al* (1995)) of $\gg$ 60 GPa. Unlike the case of MgO, which remains stable in the B1 phase till 600 GPa, MgTe shows structural transition

	MgTe			
	Expt.[a]	Present	Pseudo[b]	Pseudo[c]
$a(wurtz)$	8.542	8.510	8.513	8.889
$c(wurtz)$	13.946	13.899	13.902	13.70
$B_0(wurtz)$	-	41.74	-	37.30
$a(B8)$	-	7.822	7.827	7.750
$c(B8)$	-	12.698	12.711	12.661
$B_0(B8)$	-	55.70	-	51.40
$E_{coh}(B8)$	-	0.535	-	-
$a(B2)$	-	6.906	-	-
$B_0(B2)$	-	53.22	-	-
$a(PH_4I)$	-	9.667	-	-
$c(PH_4I)$	-	7.045	-	-
$B_0(PH_4I)$	-	58.04	-	-
$V_1(B8)/V_0$	<0.6	0.479	-	-
$V_2(B2)/V_0$	-	0.465	-	-
$\Delta V\%$	-	2.92	-	-
P_t	>60	190.8	-	-

Table 3.1: The calculated lattice parameters (a, c) in $a.u.$, bulk modulus (B_0) in GPa, E_{coh}, transition volumes $(V_1\ /V_0\ )$ and $(V_2/V_0\ )$ and transition pressure (P_c in GPa) for MgTe in different phases.

[a] Reference Zachariasen (1927).

[b] Reference Yeh *et al* (1992).

[c] Reference Van Camp and Van Doren (1996).

and the value of P_c is much higher than that observed for MgS and MgSe (37.7 and 31.7 GPa) (Kalpana *et al* (1994)). From figure 3.2 it is clear that the calculated $P-V$ relation is in excellent agreement with that of the experiment (Li *et al* (1995))

We predict the volume reduction for the B8 to B2 structural transition to be 2.92% (see table I). Our calculations show that the E_g decreases from the ground state as a function of pressure and before the structural transition there is a semi-conductor to metal transition (indirect band overlap metalization) due to the overlap of the chalcogen *Te-p* valence band at the high symmetry point M with that of the *Mg-s* conduction band at the Γ point. The calculated value of metalization pressure is 145 GPa ($V/V_0 \approx 0.52$). Table I clearly shows that our calculated equilibrium lattice parameters and B_0 for the B8 and wurtzite phases are in very good agreement with the earlier calculations and experiment. In the same table we have given the E_{coh} for the B8 phase and also the equilibrium lattice constants and B_0 for the B2 and PH_4I phases.

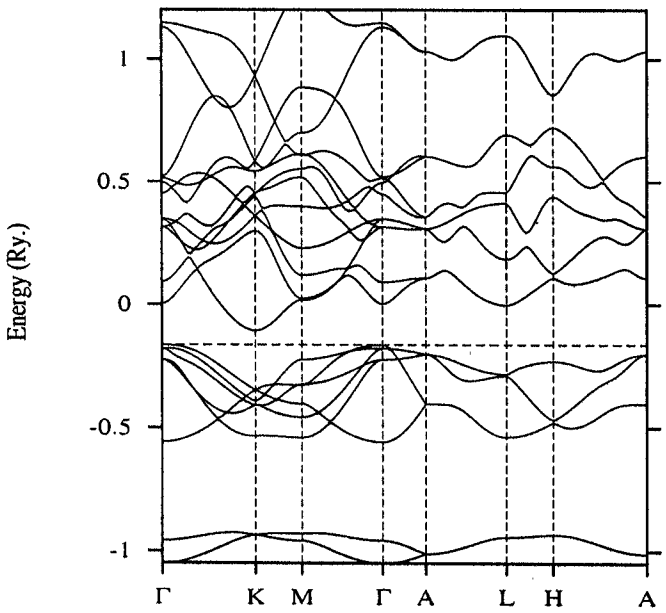

Figure 3.3: The band structure of MgTe in the B8 phase at V/V_0=1.0. In which the horizontal dashed line represents the Fermi energy (E_F).

We have calculated the cell volume ratio of B8 to wurtzite structure to be 77.16% which is in excellent agreement with earlier reported experimental value of 77.8% (Li *et al* (1995)). Figure 3.3 shows the electronic band structure of MgTe in the B8 phase at V/V_0=1.0. The bottom most two bands are predominantly due to the *Te-s* states, the bands above these are due to the *Te-p* states and the unoccupied conduction bands are due the *Mg*-s, p bands. One can also observe from this figure that MgTe is a semi-conductor as there is an indirect insulating gap (E_g) of about 0.775 eV, between the high symmetry $\vec{k}$ points Γ and K and which occurs between the *Te*-p and *Mg*-s bands. This value is very much smaller than that of 3.47 eV, calculated by extrapolation (Parker *et al* (1971)) and other experimental values 3 to 3.3 eV of Gromakov and Partala (1969) and 4.7 eV of Inuoe (1969) (high temperature measurements). Such an underestimation is quite common with LDA, but there is no experimental value available for comparison in the B8 phase. In the wurtzite phase, our calculations predict MgTe to be a wide-gap semiconductor with E_g=2.5 eV.

Chapter 4

A study of MgTe doped with transition metals Mn, Fe, Co, and Ni

4.1 Introduction

There exists extensive literature on II-VI compounds doped with transition metals (M's), specifically for M=Mn, Fe, Co, Ni (Furdyna (1988), Twardowski (1990), Dicarlo *et al* (1990), Wu *et al* (1989), Lawniczak-Jablonska *et al* (1996)). These compounds belong to a special class of materials, called diluted magnetic or semimagnetic semiconductors (DMS's), classified between non-magnetic and magnetic semiconductors. The properties of DMS's are different from those of the host II-VI compounds, mainly due to the substitution of the group-II metal by a magnetic ion (M), which occurs in the cation sublattice. Although M atoms differ from the group II elements by the fact that their $3d$ shell is only partially filled, they can contribute their $4s^2$ electrons to s-p^3 bonding, and can therefore substitutionally replace the group II elements in the II-VI tetrahedral (s-p^3 bonding) structures. The narrow partially filled M-$3d$ bands (strong correlation) are the causes for the special properties. Hybridisation of M-$3d$ states with the host II-VI semiconductor-sp band states changes the band structure and gives rise to electronic and magnetic properties of physical and technological interest. The semiconductor $MgTe$ is both of technological and scientific importance. $MgTe$ is the end point of $Mg_xCd_{1-x}Te$, $Mg_xMn_{1-x}Te$ and $Mg_xZn_{1-x}Te$ ternary systems all of which are promising opto-electronic materials (Waag *et al* (1993), Wang *et al* (1993), Wang *et al* (1994)).

In this chapter we also investigate the ground state properties of $Mg_{1-x}M_xTe$

systems using tight binding linear muffintin orbital method (TB-LMTO) method (Andersen and Jepsen (1984)). Our primary interest is to understand the effects due to the filling of $3d$ bands in M, when stepping up from Mn to Ni with different concentrations. For this we have made systematic electronic structure calculations for $MgTe$ with a large supercell in which one or two atoms are substituted with Mn, Fe, Co, Ni. Our calculated local magnetic moments for the magnetic atoms are consistent with Hund's rule perhaps due to the ionic nature of the system. However, $MgTe$ doped with Mn, Fe and Co for 25% substiution appear to be metallic. This may be due to smaller exchange and crystal field splits for the case of Mn though it has a half filled d states ($3d^5$) and in addition the failure of $SDFT$ to lift the degeneracy present in the down spin t_{2g} (one up spin t_{2g} and e_g are filled for the high spin configuration) of $3d$ bands for Fe and Co. Our calculations also show that the Ni doped systems are nonmagnetic (note that Ni itself is a weak ferromagnetic metal) metals. It is to be emphasised that there are no experimental studies available in the literature, to our knowledge, to compare our results with.

4.2 Results and Discussion

The $TB\text{-}LMTO\text{-}ASA$ method within the framework of density functional theory (DFT) (Hohenberg and Kohn (1964)) in its local density approximation (LDA) (Kohn and Sham (1965)) has been used to obtain the electronic structure, total energies and its variation with volume in B8 structure. In an earlier chapter (Basu Chaudhuri *et al* (1999)) we have shown that the normal pressure ground state structure of $MgTe$ is the B8. We have used $3s$,$3p$, $3d$ for Mg, $4s$, $4p$, $3d$ for $M(M = Mn, Fe, Co, Ni)$ and $5s$,$5p$,$5d$ for Te as the valence states. We have taken the ground state volume $V_0 = 674.1797$ $(a.u.^3)$ and c/a= 1.623, as a guideline from Van Camp and Van Doren (1995).

For the doping studies, we have constructed a supercell with hexagonal symmetry (space group P3m1), by doubling the B8 unit cell along the z-axis. In this we have replaced one (two) Mg atom by one (two) M atom without breaking the symmetry of the atomic positions. We have introduced space filling empty spheres maintaining the same symmetry for the loose packing.

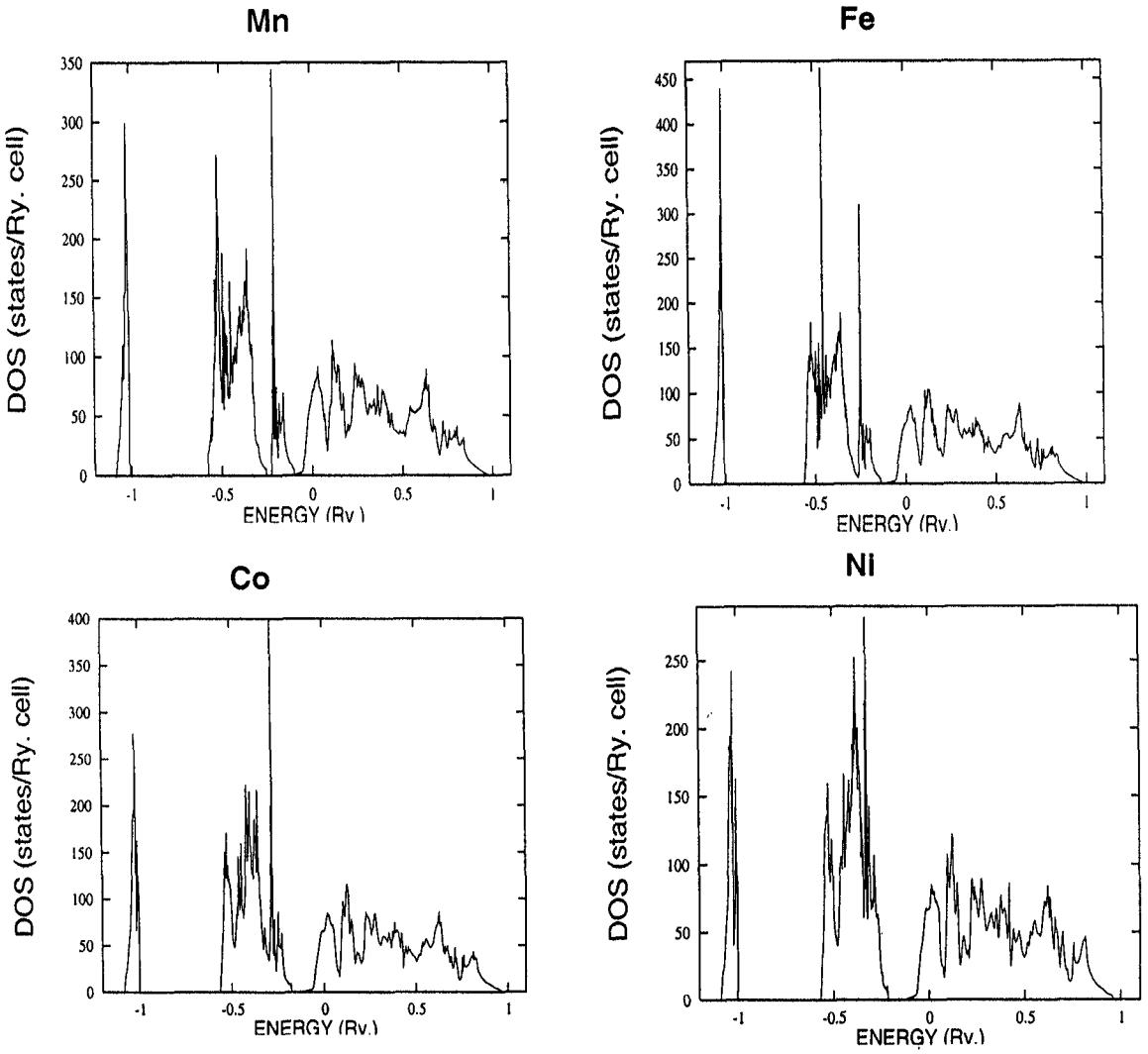

Figure 4.1: The total density of states of singly substituted $MgTe$ with (top) Mn and Fe (bottom) Co and Ni.

The calculated ferromagnetic total density of states (DOS) per primitive cell for the cases of single and double substitution of $M = Mn, Fe, Co$ and the same for the paramagnetic cases of $M = Ni$ are shown in figure 4.1. Our calculated total energies for the $M = Mn, Fe, Co$ doped systems for both the single and double substitutions favour the ferromagnetic phase (high spin configuration).

For the Ni doped systems, our total energy calculations clearly favour the paramagnetic phase (low spin configuration) as the ground state. Further, the calculated local magnetic moment for the Ni ion in the $MgTe$ matrix is zero though by Hund's rule it could have had as high as 2 μ_B, due to the left out unpaired two spins in the ionic system. This is convincing that Ni by itself is a weak ferromagnetic solid.

We have calculated the cohesive energy per formula unit for all the cases and they are 8.589, 7.930, 7.807, 7.648 eV for the Mn, Fe, Co, Ni systems respectively. The decreasing trend in this values reflects the fact of moving away from more than half filling. The calculated local magnetic moment for the singly substituted Mn, Fe, Co systems are 3.899, 2.584, 1.100 μ_B respectively and for the doubly substituted they are slightly less. These values and the decreasing trend are in accordance with the Hund's rule.

If the two magnetic atom substitute Mg in a single unit cell with Mn, they have almost the identical values of magnetic moment of about 3.751 μ_B. The difference between the local moment of the two magnetic ions increases by about 0.1 μ_B for Fe with a higher local moment of 2.185 μ_B. For Co substituted systems, the difference is about 0.25 μ_B, from the higher value of 0.962 μ_B. This difference stems from the fact that the two magnetic atoms have slightly different environments.

The physical and chemical properties of the $3d$ transition metal doped DMS materials are primarily governed by the $3d$ bands as they have the partially filled bands and the Fermi energy (E_F) passes through them. In general, depending on the filling and the crystal fields of these $3d$ bands, the ground state properties of these systems vary. Our previous experience with the perovskite oxides (Pari *et al* (1995), Pari *et al* (1996)) suggests that the $3d$ bands split into triplets and doublets under the octahedral or tetrahedral oxygen legand fields (in the present cases the magnetic ions are having octahedral coordinations of the chalcogen atoms and also two more cations) and depending on the fact whether these t_{2g} or e_g bands are completely

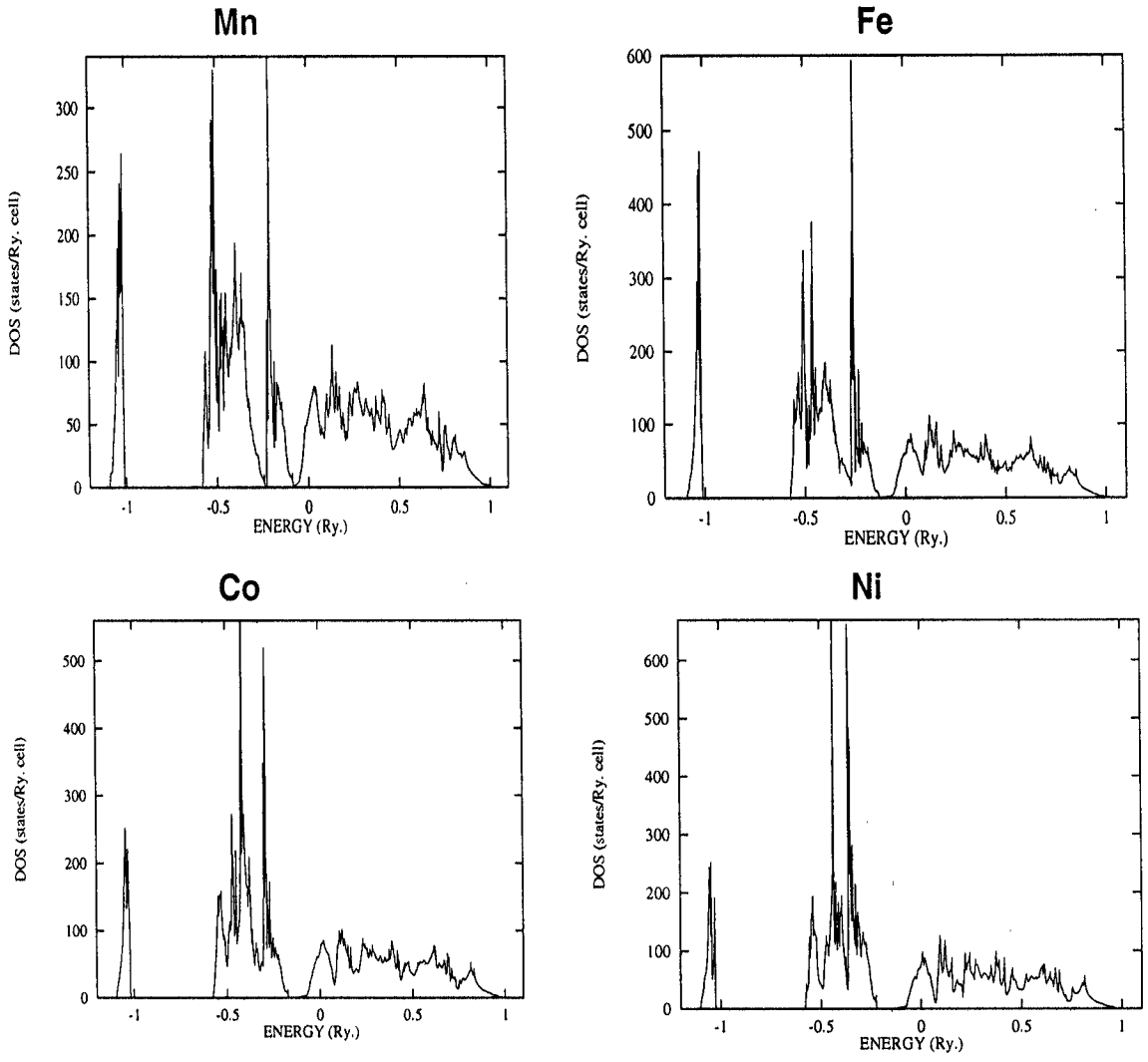

Figure 4.2: The Ferromagnetic total density of states of double substituted $MgTe$ with (top) Mn and Fe (bottom) Co and Ni.

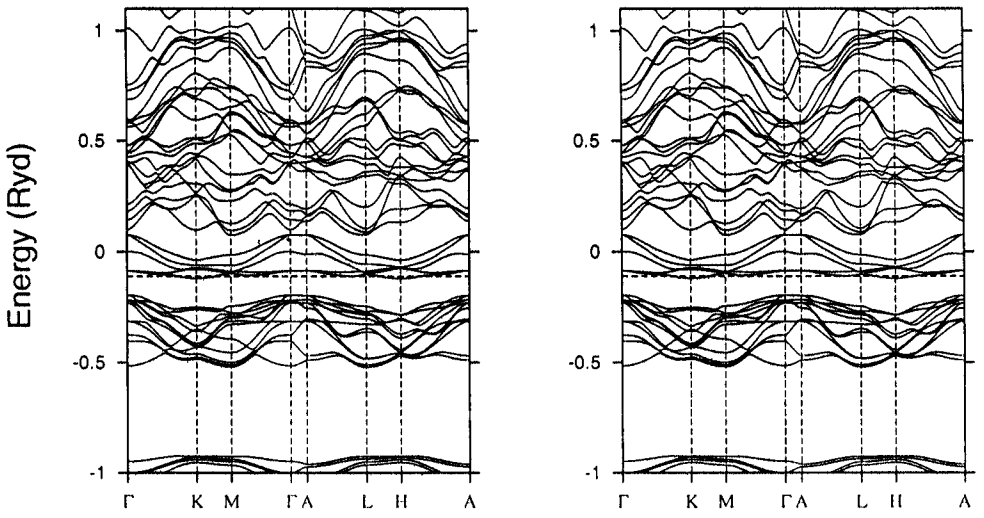

Figure 4.3: The ferromagnetic band structure of $MgTe$ singly substituted by Mn for (left) up-spin (right) down-spin. In which the horizontal dashed line represents the Fermi energy (E_F).

filled or partially filled the ground state has been described as insulating or metallic with low or high spin configurations. It is important also to note that the localised narrow $3d$ bands lead to strong correlation and the values of the Hubbard U and charge transfer energy Δ decide them to be either Mott-Hubbard or charge transfer insulators or simply correlated metals. Further we could do our doped calculations only within LDA (no non-local corrections are included to account for the many body effect) even though these systems could be strongly correlated.

Figure 4.3 show the ferromagnetic up and down spin band structures of singly Mn doped $MgTe$ in the B8 based supercell and the corresponding total DOS is given in the top part of figure 4.1. For simplicity we have not given the band structures for the rest as the band profile remains the same, instead we have shown the density of states for all. Here the bottom most bands are mainly due to the Te-s states, the bands just above them are due to Te-p states and the bands in the upper part of these p states are admixtures of Mn-d t_{2g} and Te-p bands. The supercell construction of course yield d-bands for Mn rather than impurity levels, however

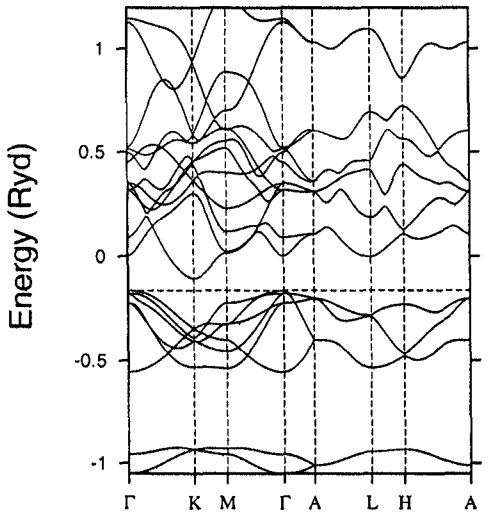

Figure 4.4: The band structure of MgTe in the B8 phase at V/V_0=1.0. In which the horizontal dashed line represents the Fermi energy (E_F).

the width of these bands are rather narrow and arise mainly due to hybridization of the impurity levels with the $Te-p$ bands.

A comparison of these figures with figure 4.4, shows that there is a strong Te-p Mn-d hybridisation and also the Mn-$3d$ bands lie in the gap between the Te-p valence and the cation s conduction bands. It is clear from figures 2(a) and (b) that the up spin Mn-d e_g bands are almost completely filled while the down spin t_{2g} bands are just started occupying. This means that the up spin e_g and spin down t_{2g} are not well separated, implying that the exchange interaction as well as the crystal field effects (split between the triplet and the doublet) are small in these systems.

One can also see from these figures that there is a strong Te-p and Mn-d mixing and this may be due to the smaller crystal field split. It is clear from these figures and the corresponding total DOS plot that the system is metallic as the E_F passes through the e_g bands and also little amount of down spin triplet of the d bands, in accordance with the Hund's rule as Mn takes the configuration of $3d^5$ in $MgTe$ with a charge state of 2+. Figures 4.1 and 4.2 which represent the total DOS, show that all the doped systems are metallic, and the topology for the 25 and 50% are

almost the same. These figures also show that there is a strong $p-d$ hybridization and also the split due to the exchange and crystal field is very small unlike the cases of perovskite oxides (Pari *et al* (1995), Pari *et al* (1996)). It is to be noted that even the ground state insulating gap of pure $MgTe$ in the B8 is small and after doping on par with the works of Albe *et al* (1998), who have shown that the gap, for nanocrystals, increases, perhaps differ for solids, our LDA based calculations show them to be metallic. This we feel to be due to the reason that LDA is not sufficient enough in providing the required exchange split to account for the insulating gap at least for the Mn, Fe, Co doped cases. Though there are no available experimental works for the ground state of the doped systems, the chemical picture tells that M substituted for Mg of valency 2, will give the $4s$ electrons to the chalcogen Te atom, and therefore the topmost filled level could be the $3d$ bands. For Mn with high spin configuration, all the up spin t_{2g} and e_g bands should be filled (half filling) with the $3d$-5 electrons and therefore the insulating gap would be between the filled up spin e_g and the empty down spin t_{2g} bands.

For Fe and Co, all the up spin states are filled completely and the E_F passes through the down spin partially filled t_{2g} bands as evidences from the DOS plots, if the correlation effects are taken into account properly that could have given the required energy to lift the degeneracy present in the t_{2g} bands. Thus the metallic ground state obtained from the LDA calculations for the Fe and Co systems could be due to the reason that the spin DFT with LDA is not sufficient enough to lift the degeneracy present in the t_{2g} state to open up a gap along with the small amount of crystal field splits.

Our 25% ferromagnetic calculations suggest clearly that the reason for the metallic ground state of Mn could be due to the smaller amount of the exchange and crystal field splits. Which may in turn be due to the longer Mn-Te bond length compared to that of the M-O-M bond lengths in the perovskite oxides (Sarma *et al* (1995)).

However, we have repeated the calculations for all the above choices with the equilibrium volume and c/a of the wurtzite phase (expansion of about 20% with respect to the B8 phase), which shows that the Mn systems for both 25 and 50% doping are insulating with a gap of about 1.5 eV, which is typical of DMS materials,

and other systems are shown to be metallic because of the failure of LDA to lift the degeneracy present in the partially filled t_{2g} bands. But the calculated local magnetic moments for these cases are almost the same as that of the actual B8 phase calculations.

Our studies on the $M_xMg_{1-x}Te$ systems with $M = Mn, Fe, Co, Ni$ clearly shows for $M = Mn, Fe, Co$ cases a magnetic (high spin configuration) metallic ground state and for the Ni doped system, a nonmagnetic metallic ground state. The exchange and crystal field splits for the M-$3d$ states are found to be very small and it is so small, irrespective of correlation effects, that the Mn systems are shown to be metallic though it has half filled d band. This we feel to be due to a stronger Te-p and M-d hybridisation which in turn due to longer bond lengths. However, in the expanded volume and c/a as that of wurtzite phase, our calculation shows a magnetic semi-conducting ground state for the Mn doped systems and for the rest as before. Our calculations conclusively show for $M = Fe, Co$ systems that they could be strongly correlated due the narrow $3d$ bands and requires corrections to LDA to lift the degeneracy present in the triplets to describe the correct ground states. The calculated local magnetic moments for the magnetic systems are consistent with the Hund's rule. We expect experiments to confirm our theoretical observations.

Chapter 5

Disorderd Solids : Introduction to Augmented Space and Configuration Averaging.

5.1 Configuration averaging in disordered systems

The idea of taking averages over all possible different states of a system is well understood and commonplace both in quantum mechanics and statistical physics. At finite temperatures different possible states of a canonical ensemble, for example, are occupied with Boltzmann probabilities, and observable physical properties are averages over the ensemble. Similarly, when we wish to measure a given physical observable in a quantum system, the result of the measurement is spread over different possible *states* with probabilities given by squared amplitudes of the wave function projection onto those states. During the last four decades considerable effort has gone into devising methods for carrying out averages of physical observables over different configurations realized by disordered systems. Why do we wish to carry out such averages and is such a procedure meaningful ?

The problem is clearly understood if we examine a specific example. An experimentalist is carrying out energy resolved photoemmission studies on a disordered metallic alloy. Varying the frequency of his incident photon and keeping the energy window of the excited outgoing electrons reasonably narrow, he can map out the density of states of the valence electrons for the alloy. If he carries out the experiment on ten different samples of the same alloy he should obtain slightly different results. The alloy is random and different samples will have different atomic arrangements of its constituents. Yet, the variation the experimenter sees in the different

samples is well within his experimental error bars. What he observes is an average result, averaged over different realizable configurations of atomic arrangements in the alloy. The interesting fact is that he sees the averaged result in a *single* sample. The same is true for other measured properties like the specific heat, conductivity and different response functions.

We note that all these measured properties are properties global to the system. Should there be a difference if we measure local properties with local probes ? Take another example of a magnetically disordered alloy AuFe (with $< 10\%$ of Fe). If we measure the magnetization of a sample it remains zero up to liquid He temperatures. Yet, if we carry out a Mössbauer study on the same alloy, there is clear indication of a frozen local exchange field at low temperatures, indicating that a local magnetization exists. Configuration averaging will be meaningless if we wish to look at local properties. Even here, a degree of averaging over the far environment is relevant. Although the radioactive Fe atom giving rise to the Mössbauer spectrum sits in different environments in different samples, yet experiments yield a unique exchange field distribution.

Why do we observe configuration averaged results in a particular macroscopic sample ? To understand this, we must examine the idea of *spatial ergodicity*. We visualize a macroscopically large system as made up of subsystems, each of which resembles a configuration of the system. Spatial ergodicity implies that, in the limit of the size and number of these subsystems becoming infinitely large, the subsystems of a single sample exactly replicate *all* its possible configurations. A global property which averages over the subsystems becomes the same as the average over all configurations.

We can illustrate this by a random Ising model, where magnetic moments, which take values $+1$ and -1 with equal probabilities, randomly occupy sites of an infinite lattice labeled by $\{R\}$.

$$\ll m_R \gg \; = \; (1/N) \sum_R m_R \; = \; 0$$

Here $\ll \quad \gg$ indicates configuration averaged quantities. Configuration averaging is a relevant subject of study for disordered systems. We have to be careful

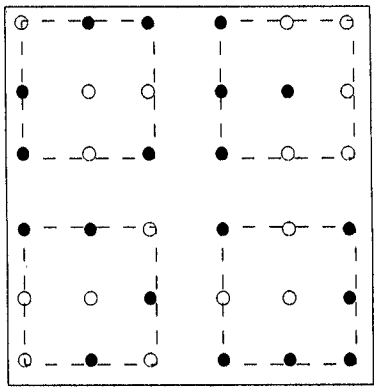

Figure 5.1: Partitioning of the system into subsystems illustrating spatial ergodicity

to ensure that the assumption of spatial ergodicity remains valid. There are situations where this assumption does fail. Chandrasekhar (1960) showed that the intensity of light observed at a point, after it has traveled in a straight line from a source through a randomly varying dielectric medium, has interesting properties. The variance of the intensity diverges as the distance between the source and observer increases. In such a situation, average intensity would be meaningless. He associated this result with the fact that stars are observed to twinkle intrinsically. Kumar and Jayannavar (1985, 1986) used similar arguments to show that, in one dimensional disordered wires of infinite length, averaged resistance is meaningless, since the variance of resistance diverges much faster than its mean. Both these results are specific to randomness and in disordered systems we have to make sure we keep this in mind and talk of configuration averages only in relevant situations.

5.2 The Augmented Space Theorem

5.2.1 Mathematical description of the configuration space

One of the main conceptual hurdles in understanding the augmented space theorem Mookerjee (1973a, b) has been the visualization of the configuration space of a set of random variables. Yet the idea is quite common in other fields. A very simple, yet essentially non trivial example is that of the Ising model. Since most readers seem comfortable enough with this model, we shall illustrate some of the basic ideas behind our description with it.

The model consists of a set of *spins* $\{\sigma_R\}$ arranged on a discrete lattice labeled by R. Each spin σ_R can have two possible *states* or *configurations* which we can denote as $|\uparrow_R\rangle$ and $|\downarrow_R\rangle$. The collection of all linear combinations of these two states : $\{a|\uparrow_R\rangle + b|\downarrow_R\rangle\}$ is called the *configuration space* of σ_R . It is of rank two and is *spanned* by the states $|\uparrow_R\rangle$ and $|\downarrow_R\rangle$. Let us call this space ϕ_R.

The set of, say, N spins then have 2^N possible *configurations* each of which can be written as a *sequence* of m up-states and N–m down-states. The ordering of this sequence is crucial, since different orderings correspond to different configurations. The number N–m is defined as the *cardinality* of the configuration and the sequence $\{C\}$ of sites $\{R_{i_1}, R_{i_2}, \ldots R_{i_k} \ldots R_{i_{N-m}}\}$ where the down-states sit is called the *cardinality sequence* of the configuration. For example, take a particular configuration of 5 spins : $|\uparrow_1\downarrow_2\downarrow_3\uparrow_4\downarrow_5\rangle$. It has cardinality 3 and a cardinality sequence $\{2,3,5\}$. Another configuration $|\downarrow_1\uparrow_2\downarrow_3\downarrow_4\uparrow_5\rangle$ also has a cardinality 3, but its cardinality sequence is $\{1,3,4\}$. These two configurations are distinct from each other.

Note that the cardinality sequence uniquely describes the configuration and is a very convenient way of labeling the different configurations $|\{C_k\}\rangle$ (where k=1,2... 2^N) of the set of N spins. The configuration space Φ is of rank 2^N and can be written as a direct product of the configuration spaces of the individual spins.

$$\Phi = \prod_R {}^{\otimes}\phi_R$$

The generalization of these ideas when the *spins* can have n > 2 states is quite straightforward. The configurations of an individual spin can be labeled as $|k_R\rangle$,

where k_R=1,2,... n. The rank of ϕ_R is now n. The set of N spins has n^N configurations. The cardinality of the configuration of an individual spin is defined as the particular k_R and the cardinality sequence uniquely describes a configuration of the set of N spins is the sequence $\{k_1, k_2, \ldots k_N\}$.

If we now translate our ideas from spins σ_R to the random variables ε_R of the Anderson model, we can immediately visualize the configuration space of the Hamiltonian variables $\{\varepsilon_R\}$. When these terms have a binary distribution, their configuration space is isomorphic to the one for a collection of Ising spins.

Let us now assume that the variables $\{\varepsilon_i\}$ are independently distributed and the probability densities are given by $p(\varepsilon_i)$. We shall take into account only those probability densities which have finite moments to all orders. Physically relevant densities almost all fall in this category. Since the probability densities are positive definite functions, we can always write them as spectral densities of a positive definite operator as follows :

$$\begin{aligned} p(\varepsilon_i) &= (-1/\pi)\, \Im m\, \langle\emptyset|\Big((\varepsilon_i + \imath 0)I \;-\; M_R\Big)^{-1}|\emptyset\rangle \\ &= (-1/\pi)\, \Im m\, g(\varepsilon_i + \imath 0) \end{aligned} \tag{5-1}$$

If ε_i has a binary distribution, taking the values 0 and 1 with probabilities x and y=1−x, then a representation of M is

$$\begin{pmatrix} x & \sqrt{xy} \\ \sqrt{xy} & y \end{pmatrix}$$

We may interpret this in terms of the configuration space ϕ_R introduced earlier. The configuration space is spanned by the states $|0\rangle$ and $|1\rangle$, which are eigenstates of M_R with eigenvalues 0 and 1. This is rather similar to the description in quantum mechanics, where an observable taking a random set of values is associated with an operator whose eigenvalues are the possible values observed and the states of the system in which the observable takes a particular value corresponds to the related eigenstate. The operator M_R in the configuration space ϕ_R will be associated with the random variable ε_i. The representation of M_R shown above is in a different basis :

$$\begin{aligned} |\emptyset\rangle &= \left(\sqrt{x}\,|0\rangle + \sqrt{y}\,|1\rangle\right) \\ |\{R\}\rangle &= \left(\sqrt{y}\,|0\rangle - \sqrt{x}\,|1\rangle\right) \end{aligned}$$

The reason for choosing this particular basis will become clear later. The state $|\emptyset\rangle$ will be called the *average state* of the system.

For a general probability distribution, we may always find the representation of the operator M_R in a similar basis by first expanding the probability density as a continued fraction.

$$g(\varepsilon_i) = -(1/\pi) \cfrac{1}{\varepsilon_i - a_0 - \cfrac{b_1^2}{\varepsilon_i - a_1 - \cfrac{b_2^2}{\ddots}}} \tag{5-2}$$

Here $p(\varepsilon_i) = \Im m\ g(\varepsilon_i)$. Since it is a positive definite function with finite moments to all orders, $p(\varepsilon_i)$ can be expanded as a convergent continued fraction. The required representation of the matrix M_i is given by

$$\begin{pmatrix} a_0 & b_1 & 0 & 0 & \dots \\ b_1 & a_1 & b_2 & 0 & \dots \\ 0 & b_2 & a_2 & b_3 & \dots \\ \dots & \dots & \dots & \dots & \dots \end{pmatrix}$$

The *average state* is defined by $|\emptyset\rangle = \sum_k \sqrt{x_k}|k\rangle$ where k are the random values taken by ε_i with probabilities x_k. The other members of the countable basis $|n\rangle$, in which the above representation of M_R is given, may be obtained recursively from the average state through :

$$\begin{aligned} |0\rangle &= |\emptyset\rangle \\ b_1\,|1\rangle &= M_R|0\rangle - a_0|0\rangle \\ b_n\,|n\rangle &= M_R|n-1\rangle - a_{n-1}|n-1\rangle - b_{n-1}|n-2\rangle \end{aligned}$$

The close relation of the above procedure to the recursion method described in the previous chapter should be noted. This is not surprising, since the projected density of states and the probability density are both positive definite and integrable functions. Convergence of the continued fraction further requires finite moments to all orders in both the cases.

5.2.2 The Augmented Space Theorem

The augmented space theorem was first introduced by Mookerjee (1973a, b). We shall discuss the theorem and its applications in some detail in this section, since it will form the basis of the methodology used in the subsequent chapters.

Let us now consider the average of a well-behaved function $f(\varepsilon_i)$ of ε_i. By definition :

$$\ll f(\varepsilon_i) \gg = \int f(\varepsilon_i) p(\varepsilon_i) d\varepsilon_i \tag{5-3}$$

Equation (5-3) may be rewritten as :

$$\ll f(\varepsilon_i) \gg = \oint f(z)\, g(z)\, dz$$

The integral is taken over a closed contour enclosing the singularities of $g(z)$ but not any of $f(z)$. We assume here that $f(z)$ is well behaved, in the sense that it has no singularities in the neighbourhood of a singularity of $g(z)$.

We now expand the function $g(z)$ in the basis of its eigenstates $\{|\mu\rangle\}$ of M_i. These may be either discrete or continuous. This expansion can be written as a Stielje's integral in terms of the spectral density function $\rho(\mu)$ of M_i

$$\begin{aligned} \ll f(\varepsilon_i) \gg &= \int d\rho(\mu) \langle \emptyset | \mu \rangle \left[\oint f(z)(z-\mu)^{-1} \right] \langle \mu | \emptyset \rangle \\ &= \langle \emptyset | \left[\int d\rho(\mu)\, |\mu\rangle\, f(\mu)\, \langle \mu | \right] | \emptyset \rangle \end{aligned}$$

The second line requires the function to be well behaved at infinity. The expression in brackets on the right side of the bottom equation is, by definition, the

operator $f(M_R)$. It is the same functional of M_R as $f(\varepsilon_i)$ was of ε_i. For example, if $f(\varepsilon_i)$ is ε_i^2 then $f(M_R)$ is M_R^2 .

This yields the central equation of the augmented space theorem :

$$\ll f(\varepsilon_i) \gg \; = \; \langle \emptyset | f(M_R) | \emptyset \rangle \tag{5-4}$$

The result is significant, since we have reduced the calculation of averages to one of obtaining a particular matrix element of an operator in the configuration space of the variable. Since we have applied the theorem to a single variable alone, the power of the above theorem is not apparent. Let us now go back to the Andersøn model where we have a set of random variables $\{\varepsilon_i\}$ which we have assumed to be independently distributed. The joint probability distribution is given by :

$$P(\varepsilon_{R_1}, \varepsilon_{R_2}, \ldots \varepsilon_{R_i} \ldots) \; = \; \prod_i p(\varepsilon_{R_i}) \tag{5-5}$$

The generalization of the above theorem to averages of functions of the set of random variables is straightforward.

$$\ll f(\{\varepsilon_i\}) \gg \; = \; \langle \emptyset | \tilde{f}(\{\widetilde{M_R}\}) | \emptyset \rangle \tag{5-6}$$

All operators in the full configuration space Φ will be denoted by tilde variables. The operators $\widetilde{M_R}$ are built up from the operators M_R as :

$$\widetilde{M_R} \; = \; I \otimes I \otimes \ldots \otimes M_R \otimes I \otimes \ldots \tag{5-7}$$

This is the *augmented space theorem* (Mookerjee (1973a, b)).

If we wish to carry out the configuration averaging of, say, the Green function element

$$G_{RR}(z) \; = \; \langle R | \, (zI \; - \; H(\{\varepsilon_{R'}\}))^{-1} \, | R \rangle$$

The theorem leads to :

$$\ll G_{RR}(z) \gg \; = \; \langle R \otimes \emptyset | \left(z\tilde{I} \; - \; \widetilde{H}(\{\widetilde{M_{R'}}\}) \right)^{-1} | R \otimes \emptyset \rangle \tag{5-8}$$

where,

$$\tilde{H} = \sum_R \mathcal{P}_R \otimes \widetilde{M_R} + \sum_R \sum_{R'} V_{ij} \mathcal{T}_{ij} \otimes \tilde{I}$$

The power of the theorem now becomes apparent. The average is seen to be a particular matrix element of the Green function of an augmented Hamiltonian. This is constructed out of the original random Hamiltonian by replacing the random variables by the corresponding configuration space operators built out of their probability distributions. This augmented Hamiltonian is an operator in the augmented space $\Psi = \mathcal{H} \otimes \Phi$ where $\mathcal{H}$ is the space spanned by the tight binding basis and Φ the full configuration space. The result is *exact*. Approximations can now be introduced in the actual calculation of this matrix element in a controlled manner. The augmented Hamiltonian has no randomness in it and therefore various techniques available for the calculation of the Green functions for non-random systems may be resorted to. In particular we shall show that the recursion method described in the earlier chapter is ideally suited for obtaining matrix elements in augmented space. Since configuration averaging is an intrinsically difficult problem, we must pay the price for the above simplification. This comes in the shape of the enormous rank of the augmented space. For some time it was thought that recursion on the full augmented space was not a feasible proposition. However, we shall describe later that, if randomness is homogeneous in the sense that $p(\varepsilon_i)$ is independent of the label R, then the augmented space has a large number of local point group and lattice translational symmetries. These can be utilized to reduce vastly the rank of the effective space on which the recursion can be carried out. Recursion on augmented space can be done with ease, even on desktop computers.

5.3 The recursion method

The recursion method was introduced by Haydock *et al* (1972) for the study of electronic structure for systems without lattice translational symmetery.

The recursion method is a constructive form of von Laue's theorem in that it expands solutions to the Schrödinger equation in a sequence of increasingly delocalized functions. Taking $|u_0\rangle$ to be the orbital on which the solutions are to be

projected, the recursion method uses the electronic Hamiltonian operator H to generate a sequence of orbitals $|u_1\rangle, |u_2\rangle, \ldots, |u_n\rangle, \ldots$ which are the successively less localized electronic states. These orbitals are related to one another by H according to the three-term recurrence relation,

$$H|u_n = a_n|u_n + b_{n+1}\rangle|u_{n+1}\rangle + b_n|u_{n-1}\rangle \tag{5-9}$$

where $|u_{-1}\rangle$ is taken to be zero, and the dependence of these orbitals on position, spin and other coordinates has been suppressed. The projection of the solution onto $|u_0\rangle$, the projected density of states (PDOS), is the imaginary part of the Green function or the resolvent

$$G_{00}(E) = \langle u_0|(EI - H)^{-1}|u_0\rangle$$

which is expanded as a continued fraction :

$$G(E) = \cfrac{1}{E - a_0 - \cfrac{b_1^2}{E - a_1 - \cfrac{b_2^2}{E - a_2 - \cfrac{b_3^2}{\ddots}}}} \tag{5-10}$$

Determination of the parameters $\{a_n, b_n\}$ and the properties of the continued fraction are discussed below.

Von Laue's theorem follows from the convergence of the continued fraction, namely that only a few moments of the PDOS determine a few levels of the fraction which bound integrals over the PDOS.

The construction of a three-term recurrence and its solution as a continued fraction will be carried out numerically.

5.4 Augmented Space Recursion

We shall propose a different path to implement the incorporation of the effects of environment fluctuation in disordered system. We wish to apply the recursion method, described by Haydock in the accompanying section directly on the augmented space

without carrying out any mean-field like approximations. We shall describe the method in a realistic model for binary alloys.

5.4.1 The Hamiltonian in augmented space

The starting point for the augmented space recursion is the most localized, sparse, tight-binding Hamiltonian, derived systematically from the LMTO-ASA theory and generalized to substitutionally disordered random binary alloys :

$$\begin{aligned} H^{\alpha}_{RL,R'L'} &= \hat{C}_{RL}\delta_{RR'}\delta_{LL'} + \hat{\Delta}^{1/2}_{RL} S^{\alpha}_{RL,R'L'} \hat{\Delta}^{1/2}_{R'L'} \\ \hat{C}_{RL} &= C^{A}_{RL} n_R + C^{B}_{RL}(1-n_R) \\ \hat{\Delta}^{1/2}_{RL} &= (\Delta^{A}_{RL})^{1/2} n_R + (\Delta^{B}_{RL})^{1/2}(1-n_R) \end{aligned} \tag{5-11}$$

Here R labels the lattice sites and L=(ℓ m) are the orbital indices (for transition metals ℓ <2), C^{A}_{RL}, C^{B}_{RL} and Δ^{A}_{RL} ,Δ^{B}_{RL} are the potential parameters of the constituents A and B of the alloy. n_R are the local site occupation variables which randomly take values 1 and 0 according to whether the site is occupied by an A atom or not. From the earlier discussion it is clear that the Hamiltonian in augmented space $\tilde{H}$ consists of replacing the local site occupation variables $\{n_R\}$ by $\{M_R\}$, and is given by :

$$\begin{aligned} \tilde{H} = \sum_{RL} \left(C^{B}_{RL}\tilde{I} + \delta C_{RL}\tilde{M}_R \right) \otimes \mathcal{P}_R + \ldots \\ + \sum_{RL}\sum_{R'L'} \left((\Delta^{B}_{RL})^{1/2}\tilde{I} + \delta\Delta_{RL}\tilde{M}_R \right) S^{\alpha}_{RL,R'L'} \left((\Delta^{B}_{R'L'})^{1/2}\tilde{I} + \delta\Delta_{R'L'}\tilde{M}_{R'} \right) \otimes \mathcal{T}_{RR'} \end{aligned}$$

where,

$$\delta C_{RL} = (C^{A}_{RL} - C^{B}_{RL})$$
$$\delta\Delta_{RL} = \left((\Delta^{A}_{RL})^{1/2} - (\Delta^{B}_{RL})^{1/2} \right)$$

Other parameters have their usual meaning and $\tilde{I}$ is the identity operator defined in the augmented space, $\tilde{M}_R$ is given by:

$$\tilde{M}^R = x\,\mathcal{P}_R^0 + y\,\mathcal{P}_R^1 + \sqrt{xy}\,\left(\mathcal{T}_R^{01} + \mathcal{T}_R^{10}\right) \tag{5-12}$$

$\mathcal{P}_R^0$ and $\mathcal{T}_R^{10}$ are projection and transfer operators in the augmented space, where each site R is characterized by two states labeled 0 and 1 , which may be identified with the up and down states of an Ising system . The configuration states are stored extremely efficiently in bits of words and the algebra of the Hamiltonian in the configuration space mirrors the multi-spin coding techniques used in numerical works with the Ising model.

The augmented Hamiltonian is an operator in a much enlarged space $\Phi = \mathcal{H} \otimes \prod \phi^R$ (the augmented space), where $\mathcal{H}$ is the Hilbert space spanned by the countable basis set $\{|R\rangle\}$ (the real space). The enlarged Hamiltonian does not involve any random variables but incorporates within itself the full information about the random occupation variables. If we substitute for M_R, then with the aid of little algebra we can show that the augmented space Hamiltonian contains operators of the following types :

(a) $\mathcal{P}_R \otimes \tilde{I}$ and $\mathcal{T}_{RR'} \otimes \tilde{I}$. These operators acting on a vector in the augmented space changes only the real space label, but keeps the configuration part unchanged.

(b) $\mathcal{P}_R \otimes \mathcal{T}_R^{01}$, $\mathcal{P}_R \otimes \mathcal{T}_{R'}^{01}$, $\mathcal{T}_{RR'} \otimes \mathcal{T}_R^{01}$ and $\mathcal{T}_{RR'} \otimes \mathcal{T}_{R'}^{01}$. These operators acting on an augmented space vector may or may not change the real space label. In addition, they may also change the configuration at the site R or R'. This resembles a single spin-flip Ising operator in configuration space.

(c) $\mathcal{P}_R \otimes \mathcal{T}_R^{01} \otimes \mathcal{T}_{R'}^{01}$ and $\mathcal{T}_{RR'} \otimes \mathcal{T}_R^{01} \otimes \mathcal{T}_{R'}^{01}$. These operators may change the real space label, as well as the configuration either at R or R' or both. This resembles a double spin flip Ising operator in the configuration space.

A basis $|\,m\rangle$ in the Hilbert space $\mathcal{H}$ is represented by a column vector C_m with zeros everywhere except at the m-th position. The inner products are defined as

$$\langle m|n\rangle = C_m^T C_n$$

$$\mathcal{P}_m C_p = \delta_{mp} C_p$$

$$\mathcal{T}_{mn}C_p = \delta_{np}C_m$$

We may represent this basis by a collection of binary words (strings of 0's and 1's) . As described earlier, the number of 1's define the cardinality of the basis and the sequence of positions at which we have 1's { $\mathcal{C}$ } called the cardinality sequence labels the basis . Thus a binary sequence B[{ $\mathcal{C}$}] is a representation of the member of the basis in the configuration space. The inner product between the basis members is then

$$(B[\{\mathcal{C}\}], B[\{\mathcal{C}'\}]) = \delta(\{\mathcal{C}\}, \{\mathcal{C}'\})$$

A careful examination of the operations (a)-(c) defined on the configuration space, reveals that these operations change the cardinality and the cardinality sequence . Since the operations are defined on the bits of words, one can easily employ the logical functions in a computer, to define these operations.

5.4.2 Symmetry reduction of the augmented space rank

The idea of reducing the rank of the Hilbert space on which the Hamiltonian acts during recursion was described by Haydock (1982). It was used extensively by Saha (1997), Dasgupta (1997) for applications to disordered alloys. We shall also use these ideas in our subsequent work.

We should note that the recursion basis $|u_n\rangle$ is generated from the starting state $|u_0\rangle$ by repeated application of the Hamiltonian. If the starting state belongs to an irreducible subspace of $\mathcal{H}$ then all subsequent recursion generated states will belong to the same irreducible subspace. Physically we may understand this as follows : the recursion states $|u_n\rangle$ carry information of distant environment of the starting state. For example, $|u_1\rangle$, which, apart from the orthogonalization subtractions, is essentially $H|u_0\rangle$, is a combination of states in the nearest shell with which $|u_0\rangle$ couple via the Hamiltonian. Similarly, $|u_n\rangle$ is a combination of n-th neighbour shell with which $|u_0\rangle$ is coupled via the Hamiltonian. If $\mathfrak{R}$ is a point group symmetry of the Hamiltonian, then all n-th neighbour shell states which are related to one another through the symmetry operator must have equal coupling to $|u_0\rangle$. Hence, it is useful to consider among the n-th neighbour shell states of which $|u_n\rangle$ is a

linear combination, only those belonging to the irreducible subspace and redefine the Hamiltonian operation.

As an example, take a nearest neighbour s-state Anderson model on a square lattice. The starting state $|(00)\rangle$ belongs to the one dimensional representation of the square lattice point group. This state then couples with linear combinations of states on neighbour shells which are symmetric under square rotations :

$$\begin{aligned}
|(0m)\} &= \left(|(0m)\rangle + |(m0)\rangle + |(\overline{m}0)\rangle + |(0\overline{m})\rangle\right)/2 \\
|(11)\} &= \left(|(11)\rangle + |(1\overline{1})\rangle + |(\overline{1}1)\rangle + |(\overline{1}\overline{1})\rangle\right)/2 \\
|(nm)\} &= \left(|(nm)\rangle + |(\overline{n}m)\rangle + |(n\overline{m})\rangle + |(\overline{n}\overline{m}\rangle + \ldots\right. \\
&\qquad \left. |(mn)\rangle + |(\overline{m}n)\rangle + |(m\overline{n})\rangle + |(\overline{m}\overline{n}\rangle\right)/(2\sqrt{2})
\end{aligned}$$

If we go up to N shells (if N is large) there are about $2N^2$ states in the diamond shaped nearest neighbour cluster. However there are only $(N^2/4 + N/2) \sim N^2/4$ states with square symmetry. We need only to work in 1/8 of the lattice but attach correct weights to the states to reproduce correct matrix elements. This reduction is standard in Brilluoin zone integrations in reciprocal space, but not so prevalent in real space calculations.

If $|I\rangle$ and $|J\rangle$ are two states coupled to each other via the Hamiltonian, and both belong to the same irreducible subspace, and let $|I_1\rangle, |I_2\rangle \ldots |I_{W_I}\rangle$ be states obtained by operating on $|I\rangle$ by the symmetry group operations of the real space lattice. W_I is called the *weight* associated with the state labeled by I. If we wish to retain only the states in the irreducible subspace and throw out the others and yet obtain the same results, we redefine the Hamiltonian matrix elements as follows :

$$\langle I|H|J\rangle \rightarrow \sqrt{\frac{W_J}{W_I}}\beta_J(LL')\langle I|H|J\rangle$$

The factor $\beta_J(LL')$ requires explanation. The new irreducible basis, which is a linear combination of the tight-binding basis , reflects not only the symmetries of the underlying lattice, but the symmetry of the starting orbital (spherical if it is a s-state, cylindrical if it a p-state and an e_g or t_{2g} symmetry if it is a d-state) also. This symmetry of the starting orbital prohibits overlap at particular sites.

These positions we shall define to be the *symmetry positions* with respect to the overlapping orbitals. These position depends on the L and L' content of I and J. If the state J is a symmetry position with respect to LL' then $\beta_J(LL')$ is 0 otherwise it is 1.

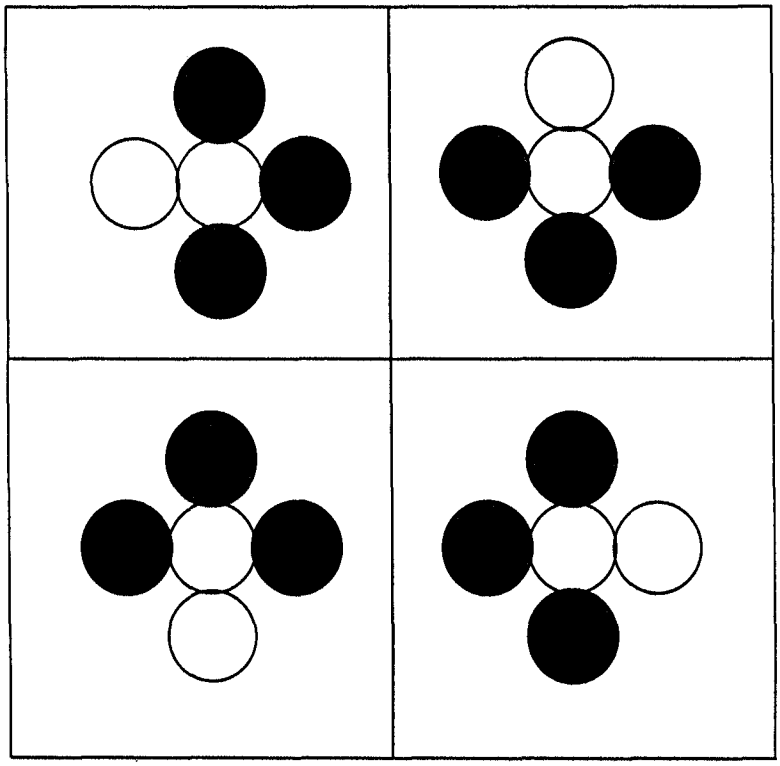

Figure 5.2: Equivalent configurations on a square plaquette

If disorder is homogeneous, then the cardinality sequence in configuration space itself has the symmetry of the underlying lattice. For example, in figure 5.2, since the lattice is infinite, the four configurations shown above are equivalent. It is obvious they are related to one another by the symmetries of the square lattice. Thus in augmented space equivalent states are $|R \otimes \{C\}|$ and the set $|\Re R \otimes \{\Re\{C\}\}|$ for all different symmetry operators $\Re$ of the underlying lattice.

The following table gives us an idea of the reduction of the rank of augmented space and the saving in computing CPU time for a simple s-state tight-binding Hamiltonian for a binary alloy.

Once we have defined the reduced Hamiltonian, recursion on the full augmented

shells	N_{full}	N_{red}	t_{full}	t_{red}
5	70	17	4.73	1.69
7	610	103	5.62	1.73
9	4838	691	6.87	1.77

Table 5.1: Comparison between system size and CPU time in seconds on a HP9000/300 machine for a full square lattice binary alloy and the reduced lattice in augmented space

space with starting state $|u_0\rangle = |RL \otimes \{\emptyset\}\rangle$ gives the configuration averaged Green function directly. The recursion coefficients a_n and b_n are generated by

$$\begin{aligned} \tilde{H}|u_n\rangle &= a_n|u_n\rangle + b_{n+1}|u_{n+1}\rangle + b_n|u_{n-1}\rangle \\ a_n &= \langle u_n|\tilde{H}|u_n\rangle \\ b_n &= \langle u_{n-1}|\tilde{H}|u_n\rangle \end{aligned}$$

The configuration averaged Green function then can be written as a continued fraction

$$\ll G_{RL,RL}(z) \gg = \cfrac{1}{z - a_0 - \cfrac{b_1^2}{z - a_1 - \cfrac{b_2^2}{\ddots \cfrac{b_N^2}{z - a_N - b_{N+1}^2 T(z)}}}}$$

For an infinitely large system the continued fraction does not terminate at any finite step. The continued fraction approach is meaningful only if we can estimate what its asymptotic part would be from a set of initial coefficients. This asymptotic part is called the *terminator*. The theory of convergent continued fractions indicates that the asymptotic part determines the essential singularities of the Green function, *i.e.* the band edges and the band weights. The band edges can be determined, first

crudely, from a few initial continued fraction coefficients and then refined by noting how they converge as we include a few more coefficients. Once the band edges e_{min} and e_{max} and the band weight w are estimated, the model herglotz function is generated as :

$$F(z) = 8\,w\left[z - \frac{e_{max}-e_{min}}{2} - \sqrt{(z-e_{min})(z-e_{max})}\right]/(e_{max}-e_{min})^2$$

The continued fraction coefficients which yield F(z) are

$$\begin{aligned} \hat{a}_n &= (e_{max}+e_{min})/2 \qquad \text{for all n} \\ \hat{b}_n &= (e_{max}-e_{min})/4 \qquad \text{for all n} \end{aligned}$$

Luchini and Nex (1987) suggested that rather than butt-joining of the terminator coefficients to the first n_1 exactly calculated coefficients, we splice them it smoothly as follows :

$$\hat{a}_n = \begin{cases} a_n & n < n_1 \\ 1/2\,\{(1-sin\{\delta(n+\phi)\}a_n + (1+sin\{\delta(n+\phi)\}\hat{a}_n\} & n_1 < n < n_2 \\ \hat{a}_n & n_2 < n \end{cases}$$

$$\hat{b}_n = \begin{cases} b_n & n < n_1 \\ 1/2\left\{(1-sin\{\delta(n+\phi)\}b_n + (1+sin\{\delta(n+\phi)\}\hat{b}_n\right\} & n_1 < n < n_2 \\ \hat{b}_n & n_2 < n \end{cases}$$

where $\delta = \pi/(n_2\text{-}n_1)$ and $\phi = -(n_1+n_2)/2$.

We now proceed to obtain run two further recursions. The first one obtains two sets of orthogonal polynomials corresponding to the three term recursion :

$$\begin{aligned} P_{n+1}(z) &= (z-a_n)P_n(z) - b_n^2 P_{n-1}(z) \\ Q_{n+1}(z) &= (z-a_n)Q_n(z) - b_n^2 Q_{n-1}(z) \end{aligned}$$

where $P_1(z) = 0 = Q_0$ and $P_0 = 1 = Q_{-1}$.

The second one, starts with a state $|0> = F(z)$ and obtains a set of coefficients $\{\gamma_n\ ,\ \delta_n\}$ from :

$$|n+1\rangle \ = \ (z-\gamma_n)|n\rangle - \delta_n^2|n-1\rangle$$

where the inner product is defined by a union of Gauss-Chebyshev quadrature :

$$\langle f|g\rangle \ = \ \sum_i \omega_i f(\alpha_i) g(\alpha_i)$$

with

$$\begin{aligned} \omega_i &= \frac{\pi w}{n+1} sin^2\vartheta_i \\ \alpha_i &= a_i + (1 - cos\vartheta_i)(e_{max} - e_{min})/2 \\ \vartheta_i &= \frac{i\pi}{n+1} \end{aligned}$$

From these continued fraction coefficients, exactly as above, we generate two sets of orthogonal polynomials

$$\begin{aligned} R_{n+1}(z) &= (z-\gamma_n)R_n(z) - \delta_n^2 R_{n-1}(z) \\ S_{n+1}(z) &= (z-\gamma_n)S_n(z) - \delta_n^2 S_{n-1}(z) \end{aligned}$$

The terminator is then

$$T(z) \ = \ \frac{S_{n_2-2}(z) - F(z)R_{n_2-1}(z)}{\delta_{n_2-1}^2 \left[S_{n_2-3}(z) - F(z)R_{n_2-2}(z)\right]} \qquad (5\text{-}13)$$

Since F(z) is a herglotz function and $R_n(z)$ and $S_n(z)$ are polynomials, the above equation shows that the terminator T(z) is also herglotz. The Green function is then given by

$$G(z) \ = \ \frac{Q_{n_2-2}(z) - b_{n_2-1}^2 T(z) Q_{n_2-3}(z)}{P_{n_2-1}(z) - b_{n_2}^2 T(z) P_{n_2-2}(z)} \qquad (5\text{-}14)$$

There is an extensive literature on the construction of terminators (Luchini and Nex (1987)). We refer the reader to these for further mathematical details. All terminators are herglotz and require no further input other than the first n_1 continued fraction coefficients.

Chapter 6

Electronic structure and magnetism in disordered bcc Fe alloys

6.1 Introduction

Iron, being one of the ferromagnets among the late transition metals, have drawn considerable attention for investigating its magnetic properties. Apart from studies on elemental Fe which include the studies on structural (Ishikawa (1978)) and magnetic phase stability (Andersen (1977), Pinski *et al* (1986), Hiraki (1989))there are numerous investigations on magnetism in Fe based ordered and disordered alloys, both theoretically and experimentally. The experimental investigations have provided a variety of informations about the magnetic properties of these systems like variation of magnetisation with band filling (Shull (1955), Bardos (1969)), moment distribution in dilute Fe alloys in low (Collins (1965)) as well as in finite temperatures (Child (1976)), local environmental effects on magnetic properties (Radhakrishnan and Livet (1978), Kajzar and Parette (1980)), spatial distribution and thermal variation of hyperfine fields (Arp *et al* (1952), Johnson *et al* (1963), Koi *et al* (1964), Lutgemeir and Dubiel (1982)), concentration dependence of high field susceptibility (Stoelinga (1966)), low temperature specific heat (Cheng *et al* (1960), Schroder (1962)) and magnetic phase stability leading eventually to magnetic phase diagrams

[1]The contents of this chapter has been published in Ghosh, Sanyal, Basu Chaudhuri and Mookerjee, *Eur. J. Phys.* **B23** 455 (2001)

(Van Baal (1973)).

The earlier explorations on theoretical side started depending on various models of band structure calculations (Hasegawa and Kanamori (1971), Jo (1982)). Though these calculations were successful to certain extent in explaining the experimental observations, they suffered from the drawback of having too many adjustable parameters which limit the reliability of the results. But, with the recent progresses in first principles electronic structure techniques the possibility of predicting and explaining the properties of magnetic alloys efficiently and accurately has increased quite a lot. In recent times there have been substantial amount of investigations on Fe based alloys using various first principles techniques which have been able to throw lights on different aspects of magnetism in both ordered and disordered phases overcoming the limitations of experiments and earlier model calculations (James (1999), Burke (1983), Ebert *et al* (1990), Martinez-Herrera (1985), Asano *et al* (1978), Akai (1993), Bluegel (1987), Turek (1994), Paduani (1998), Kasper (1983)). In this chapter, we aim at a systematic study of electronic structure and magnetic properties of substitutionally disordered Co_xFe_{1-x}, Cr_xFe_{1-x} and Mn_xFe_{1-x} alloys using self consistent TBLMTO-ASR technique. As a pure element, bcc iron is a ferromagnet whereas bcc chromium is a weak noncommensurate antiferromagnet, manganese has a very complicated crystal (unit cell of 58 atoms) and magnetic structures and cobalt is a ferromagnet. This naturally leads to the appearance of many interesting magnetic configurations in these alloys. For FeCr, iron atoms stabilize the commensurate antiferromagnetic (B2) order at Cr-rich side (x>0.8) although Cr_xFe_{1-x} with x>0.8 are ferromagnets and stabilize in bcc lattice (Kulikov and Demangeat (1997), Fawcett (1994), Furuska (1986)). In case of MnFe alloys, ferromagnetic phase is stable only upto x=0.2 and the crystal stabilises in bcc lattice. For x>0.2, several phases with anti-ferromagnetic ordering get stabilized (Endoh (1971)). In FeCo alloys, however, the ferromagnetic phase is stable for the full range of concentrations and the crystal too stabilises in bcc. All these systems exhibit some unusual and interesting magnetic properties. For these reasons, they have been thoroughly investigated. But, to our knowledge, no systematic studies together on these three systems has been done so far though they are the four successive members on the same row of periodic table. This motivated us to perform a systematic investigation of these systems

to have a deep understanding of the properties of transition metal alloys. In this work, we have restricted ourselves only to ferromagnetic phases of these systems. Moreover, no chemical clustering or short-range order effects have been taken into account.

6.2 Theoretical Details

To study these alloys we will use the methodology of the augmented space recursion (ASR) technique (Mookerjee and Prasad (1993), Saha *et al* (1994), Sanyal *et al* (1998)) in the first principles framework of tight-binding linearized muffin tin orbital theory (Andersen *et al* (1985)). Extensive details of the description of the effective augmented-space Hamiltonian have been given in an earlier chapter (Biswas *et al* (1995)). Here we shall quote the key results of generalised TBLMTO-ASR .

$$\begin{aligned} H &= \sum_{RL} \hat{C}_{RL}\mathcal{P}_{RL} + \sum_{RL}\sum_{R'L'} \hat{\Delta}^{1/2}_{RL} S^{\beta}_{RL,R'L'} \hat{\Delta}^{1/2}_{R'L'} \mathcal{T}_{RL,R'L'} \\ \hat{C}_{RL} &= C^{B}_{RL} + \left(C^{A}_{RL} - C^{B}_{RL}\right) n_R \\ \hat{\Delta}^{1/2}_{RL} &= \Delta^{B1/2}_{RL} + \left(\Delta^{A1/2}_{RL} - \Delta^{B1/2}_{RL}\right) n_R \end{aligned} \tag{6-1}$$

Here $\mathcal{P}_{RL}$ and $\mathcal{T}_{RL,R'L'}$ are projection and transfer operators in the hilbert space spanned by the tight binding basis $|RL\rangle$ and n_R is a random occupation variable which is 1 if the site R is occupied by an atom of the A type and 0 if not. C^{Q}_{RL} and Δ^{Q}_{RL} are potential parameters describing the scattering properties of the constituents (Q=A, B) of the alloy and $S^{\beta}_{RL,R'L'}$ is the screened structure constant describing the geometry of the underlying lattice. The augmented space hamiltonian replaces the random occupation variable by operators M_R of rank 2. For models without any short-range order

$$M_R = x\mathcal{P}^{R}_{\uparrow} + (1-x)\mathcal{P}^{R}_{\downarrow} + \sqrt{x(1-x)}\left(\mathcal{T}^{R}_{\uparrow\downarrow} + \mathcal{T}^{R}_{\downarrow\uparrow}\right)$$

$$\begin{aligned} |\uparrow\rangle &= \left(\sqrt{x}|0\rangle + \sqrt{1-x}|1\rangle\right) \\ |\downarrow\rangle &= \left(\sqrt{1-x}|0\rangle - \sqrt{x}|1\rangle\right) \end{aligned}$$

The recursion method then expresses the Green functions as continued fraction expansions. The continued fraction coefficients are exactly obtained upto eight levels and the terminator suggested by Luchini and Nex (Luchini and Nex (1987)) is used to approximate the asymptotic part. The convergence of this procedure has been discussed by Ghosh *et al* (Ghosh *et al* (1997)). The local charge densities are given by :

$$\rho_\sigma^\lambda(r) \;=\; (-1/\pi)\Im m \sum_L \int_{-\infty}^{E_F} dE \ll G_{LL}^{\lambda,\sigma}(r,r,E) \gg \qquad (6\text{-}2)$$

Here λ is either A or B. The local magnetic moment is

$$m^\lambda \;=\; \int_{r<R_{WS}} d^3r \; [\rho_\uparrow(r) \;-\; \rho_\downarrow(r)]$$

The Curie temperature T_C can be calculated using Mohn-Wolfarth model Mohn and Wohlfarth (1987) from the expression

$$\frac{T_C^2}{T_C^{S^2}} + \frac{T_C}{T_{SF}} \;-\; 1 \;=\; 0$$

where, T_c^S is the stoner Curie temperature calculated from the relation

$$\langle I(E_F)\rangle \int_{-\infty}^{\infty} N(E) \left(\frac{\delta f}{\delta E}\right) dE \;=\; 1 \qquad (6\text{-}3)$$

$\langle I\ (E_F)\rangle$ is the concentration averaged Stoner parameter. The parameters of pure elements are obtained from the earlier calculations (Janak (1977)) , $N(E)$ is the density of states per atom per spin (Gunnarson (1976)) and f is the Fermi distribution function. T_{SF} is the spin fluctuation temperature given by,

$$T_{SF} \;=\; \frac{m^2}{10 k_B \langle\chi_0\rangle} \qquad (6\text{-}4)$$

$\langle\chi_0\rangle$ is the concentration weighted exchange enhanced spin susceptibility at equilibrium and m is the averaged magnetic moment per atom. χ_0 (pure elements) is calculated using the relation by Mohn (Mohn and Wohlfarth (1987)) and Gersdorf (Gersdorf (1962)):

$$\chi_0^{-1} \;=\; \frac{1}{2\mu_B^2}\left(\frac{1}{2N^\uparrow(E_F)} \;+\; \frac{1}{2N^\downarrow(E_F)} \;-\; I\right)$$

I is the stoner parameter for pure elements and $N^{\uparrow}(E_F)$ and $N^{\downarrow}(E_F)$ are the spin-up and spin-down partial density of states per atom at the Fermi level for each species in the alloy.

6.3 Calculational Details

For the calculation of the component projected averaged density of states of the ferromagnetic phase we have used a real space cluster of 400 atoms and an augmented space shell upto the sixth nearest neighbour from the starting state. Eight pairs of recursion coefficients were determined exactly and the continued fraction terminated by the analytic terminator due to Luchini and Nex (Luchini and Nex (1987)). In a paper Ghosh *et al* (Ghosh *et al* (1997)) have shown the convergence of the related integrated quantities, like the Fermi energy, the band energy, the magnetic moments and the charge densities, within the augmented space recursion. The convergence tests suggested by the authors were carried out to prescribed accuracies. We noted that at least eight pairs of recursion coefficients were necessary to provide Fermi energies and magnetic moments to required accuracies. We have reduced the computational burden of the recursion in the full augmented space by using the local symmetries of the augmented space to reduce the effective rank of the invariant subspace in which the recursion is confined (Saha *et al* (1996)) and using the seed recursion methodology (Ghosh *et al* (1999)) with fifteen energy seed points uniformly across the spectrum.

We have chosen the Wigner-Seitz radii of the two constituent atoms in such a way that the average volume occupied by the atoms is conserved. Within this constraint we have varied the radii so that the final configuration has neutral spheres. This eliminates the necessity to include the averaged Madelung Energy part in the total energy of the alloy. The definition and computation of the Madelung Energy in a random alloy had faced controversy in recent literature and to this date no satisfactory resolution of the problem exists. Simultaneously we have made sure that the sphere overlap remains within the 15% limit prescribed by Andersen.

The calculations have been made self-consistent in the LSDA sense, that is, at each stage the averaged charge densities are calculated from the augmented space

recursion and the new potential is generated by the usual LSDA techniques. This self-consistency cycle was converged in both total energy and charge to errors of the order 10^{-5}. The exchange-correlation potential of Von Barth and Hedin has been used, s, p and d orbitals were used to construct the basis functions and scalar relativistic corrections were included. We have also minimized the total energy with respect to the lattice constant. The quoted results are those for the minimum configuration. In these calculations, any lattice distortions due to the size differences between the two constituents has been neglected.

6.4 Results and Discussion

In our approach we emphasize on interrelations of magnetism and charge transfer behaviour. While describing magnetic properties of alloys one has to always keep in mind the role of charge transfer. Since in our calculations we have maintained local charge neutrality, we have to deal with the question of strong variation of magnetic moments. Within the itinerant electron theory of magnetism this can be understood in terms of a redistribution of local electronic charge either between two spin directions. Together with Coulomb interaction which determines the positions of atomic d levels of the constituents and thus the charge transfer in case of a transition metal alloy, magnetic exchange and hybridisation play very important role in determining the magnetic properties. This has already been observed in certain cases (Richter (1988), Schwarz (1982)). Here also we will try to explain the variations in magnetic properties of the three systems considering these facts.

These facts can be expressed in a more quantitative form using d-orbital potential parameters $C^Q_{d\sigma}$ obtained from TBLMTO for both alloy components (Q=A, B) and for both spin directions (σ=$\uparrow$, $\downarrow$). These quantities are equivalent to the atomic d levels.

The spin dependent diagonal disorder in a random binary alloy A_xB_{1-x} can be defined as Turek (1997) ,

$$\delta_\sigma = C^A_{d\sigma} - C^B_{d\sigma} \tag{6-5}$$

The local exchange splitting can be defined as Turek (1997),

$$\Delta_e^Q = C_{d\downarrow}^Q - C_{d\uparrow}^Q \tag{6-6}$$

In our discussions we will show that the behaviour of these quantities determine the magnetic properties of the alloys.

Figure (6.1) shows the compositional dependence of local and average magnetic moments for Co_xFe_{1-x}. The filled triangles denote the average moments while the filled circles denote Fe moment and filled squares denote Co moments. The open triangles denote the experimental values of average moment (Bardos (1969)) while the open circles denote experimental Fe moments (Collins and Forsyth (1963)) and the open squares denote experimental Co moments (Collins and Forsyth (1963)). It is clear that our results agree well with the experiments, in particular the qualitative trend of local as well as average magnetic moments. The results suggest that the Fe moment increases rapidly with increasing Co content upto x=0.3 beyond which it tends towards a saturation while the Co moment remains almost constant for the whole range of concentrations. As a result, the average magnetisation reaches a maximum at 30% of Co beyond ehich it starts decreasing. Similar behaviour has been observed in previous studies using LCAO-CPA (Richter (1988)) and LMTO-CPA (Turek (1994)).

This nonmonotonic variation of average magnetisation can be explained from the variation of local number of electrons (Figure 6.2) and density of states (Figure 6.3). In this case, a transition from weak ferromagnetism (incompletely filled majority *d* band) for Fe-rich side to strong ferromagnetism (majority *d* band completely filled) for alloy with a higher Co content (x>0.3) is seen. The initial increase of alloy magnetisation corresponds to a continuous filling of majority bands while the minority bands remain almost constantly occupied. The linear decrease of alloy magnetisation with increasing x for x>0.3 reflects a strong ferromagnetic region in which majority bands are fully occupied whereas the minority bands accommodate more electrons with increasing Co content.The filling of majority band upto x=0.3 mainly occurs due to incompletely filled majority *d* band of weak ferromagnet Fe (Figure 6.2 (b)) while the rise in the minority band filling beyond x=0.3 is essentially due to a fall in Fe minority electrons and an almost constant nature of Co minority

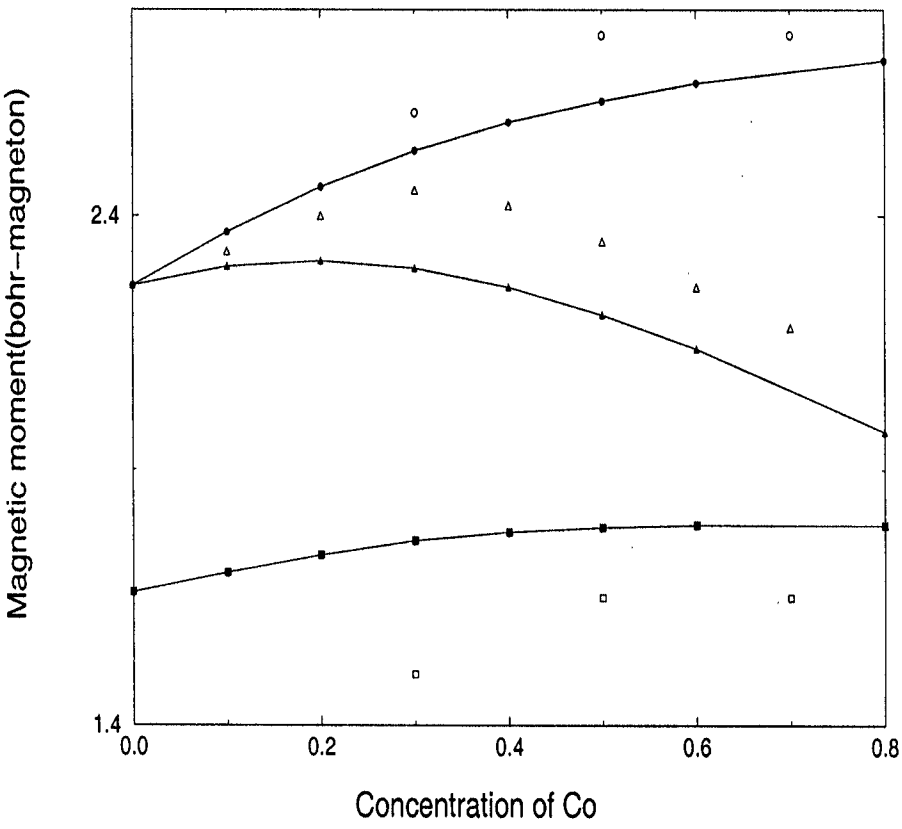

Figure 6.1: Partial and averaged magnetic moments (in Bohr-magneton/atom) vs. concentration of Co for Co_xFe_{1-x} alloy. The solid line with up triangles represents calculated averaged values, the solid line with filled circles represents calculated Fe moments, the solid line with filled squares represents calculated Co moments. The open up triangles are the experimental values of average moments, the open circles are the experimental Fe moments and the open squares are the experimental Co moments.

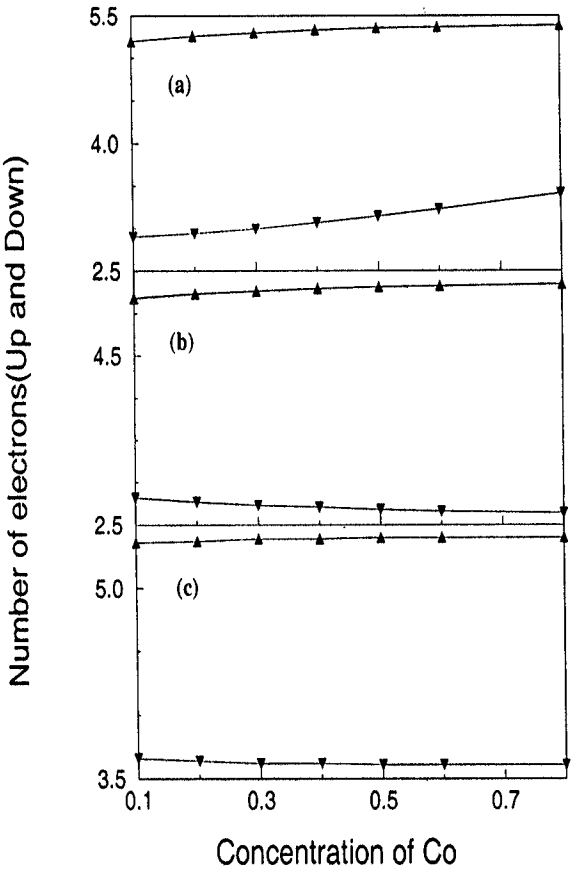

Figure 6.2: (a) represents average number of valence electrons for both spins vs. concentration of Co for Co_xFe_{1-x} alloy. The up triangles are for spin-up electron number and the down triangles are for spin-down electron number. (b) represents number of electrons at Fe site for both spins vs. concentration of Co. The up and down triangles stand for up and down spin electrons respectively. (c) represents number of electrons at Co site for both spins. The symbols represent identical things as (a) and (b).

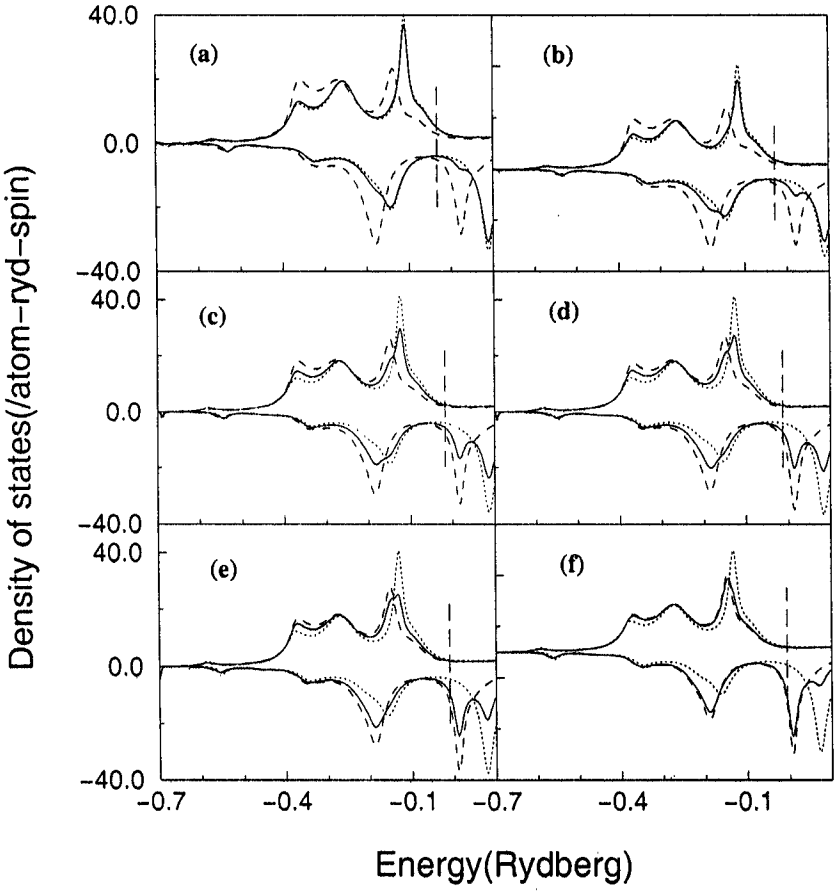

Figure 6.3: Spin projected partial and averaged densities of states/atom of Co_xFe_{1-x} alloy. The various panels are for different concentrations of Co- (a)10% (b)20% (c)40% (d)50% (e)60% (f)80%. In all the cases, the solid line represents averaged density of states while the dashed and the dotted line stand for Co and Fe partial density of states respectively. The vertical dashed lines are the Fermi levels.

x_{Co}	Δ_e^{Fe}	Δ_e^{Co}
0.1	0.179	0.136
0.2	0.185	0.139
0.3	0.190	0.140
0.4	0.194	0.142
0.5	0.196	0.142
0.6	0.199	0.142
0.8	0.201	0.138

Table 6.1: Local exchange splitting values (in Ryd) in Co_xFe_{1-x} with varying concentration of Co

electron number variation (Figure 6.2 (c)).

This is reflected in features of density of states (Figure 6.3) as well as variation of density of states of fermi level $n(E_F)$ (Figure 6.4 (a)). For majority spin states the filling of *d* band occurring at Fe sites is accompanied by a steady decrease of $n(E_F)$. This process is finished at x=0.3. Up to this, fermi level is pinned to the minimum of minority spin density of states (Figure 6.3 (a)- (b)). Increasing Co content which essentially means gradual filling, shifts fermi level to regions of low spin up density of states and above x=0.3 to increasing spin down density of states (Figure 6.3 (c)-(f)). Thus $n(E_F)$ for up spin (shown by up triangles in Figure 6.4 (a)) decreases while nE_F) for down spin (shown by down triangles) increases continuously beyond x=0.3. As a result, average $n(E_F)$ (shown by squares) goes through a minimum around x=0.3.

All these phenomena are a consequence of local charge neutrality, exchange and hybridisation. Since bcc Co is already a saturated ferromagnet, there is hardly any possibility to increase substantially the number of majority spin electrons and thereby the local magnetic moment of Co. Because of small *sp*-density of states at fermi level (Figure 6.3) compared with *d* contribution, the transfer of minority spin *d* electrons to *sp*-states is expected to be very small. Thus, Co moment is almost independent of alloy concentration and the possible exchange splitting of Co *d* level remains almost constant throughout the con centration regime (Table 6.1).

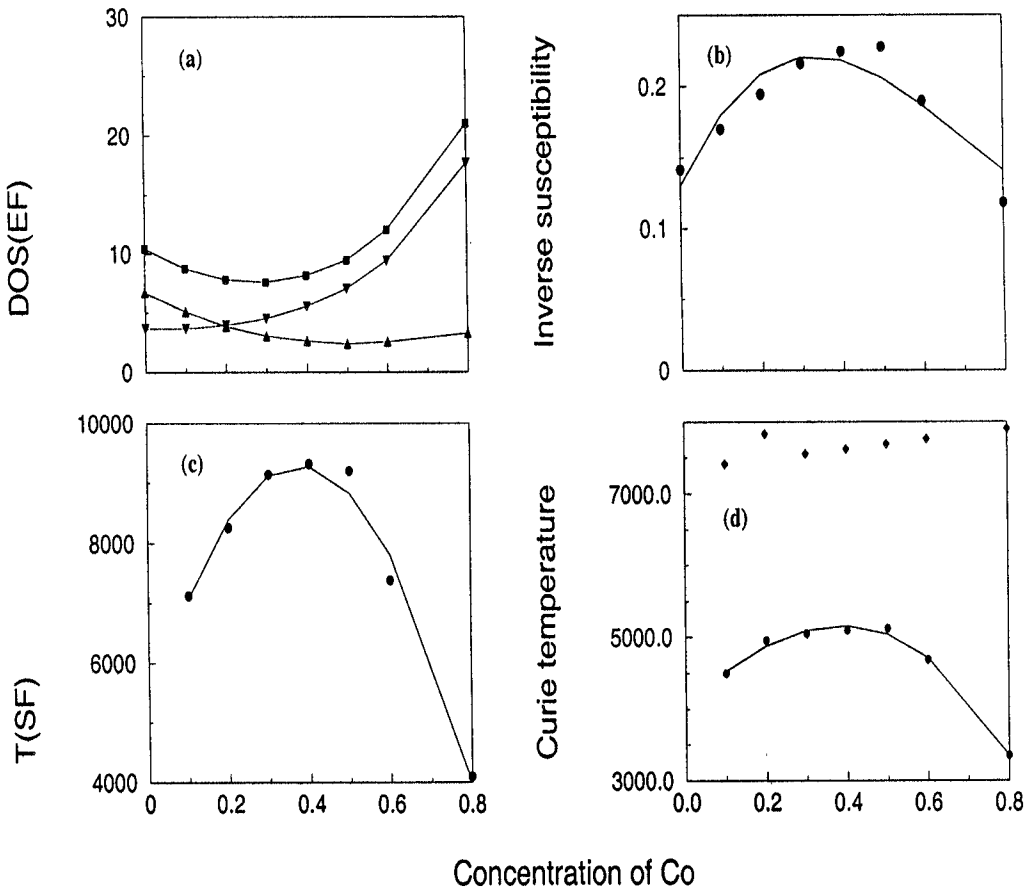

Figure 6.4: (a) Density of states at the Fermi level (b) Inverse susceptibility (c) Spin Fluctuation temperature and (d) Curie Temperature as a function of the concentration of Co in CoFe alloys. In (d) the solid line and the filled circles represent the variation of Curie temperature (T_c) in kelvin calculated using MW model vs Co concentration in Co_xFe_{1-x}. The diamonds stand for the values of Stoner Curie temperature (T_c^S) in kelvin.

On the other hand, the weak ferromagnetism of Fe gives rise to the possibility of filling approximately 0.3 majority spin holes with minority spin electrons. Thus, local Fe moment increases as a result of increase in local exchange splitting (Table 6.1). Hence, in spite of being nearest neighbours in the periodic table the exchange makes their behaviour so different.

The role of hybridisation influencing the local magnetic properties can be explained in terms of BCT model (Richter (1987)). As is evident from the density of states, the disorder in the minority spin band is more prominent which is also realised quantitatively from δ^{σ} variation. While $\delta^{\uparrow}$ varies from 40 mRy from Fe-rich side to 6 mRy in Co-rich side, $\delta^{\downarrow}$ remains $\simeq$ 0.8 Ry for the whole range of concentrations. According to BCT idea, different positions of atomic $d^{\downarrow}$-levels of Fe and Co cause bonding charge transfer (BCT) in the minority spin band. An inspection of densities of states at various concentrations (Figure 6.3) shows that the bonding part of spin-up density of states has a larger Co weight whereas Fe dominates the anti-bonding part. A transition of minority spin electrons from Fe to Co occurs. To maintain local charge neutrality, mainly Co minority spin electrons are transferred to Fe majority band causing an increase of exchange splitting and magnetic saturation. As a result, a net electron redistribution from $Fe^{\uparrow}$ to $Fe^{\downarrow}$ state occurs only to increase Fe moment.

So, to conclude, the magnetisation behavior of CoFe is characterised on the Fe-rich side by the magnetic saturation due to hybridisation whereas the Co- rich side is determined simply by filling of minority band.

Figure 6.4 (b)-(d) respectively show the variation of inverse susceptibility, spin fluctuation temperature and Curie temperature calculated using MW model. The variation of inverse susceptibility is exactly reverse in nature to that of $n(E_F)$. This is due to the fact that inverse susceptibility is dependent on $n(E_F)^{-1}$ only as stoner parameter is a constant quantity. The variation of spin fluctuation temperature follows the same nature as of magnetisation and inverse susceptibility which are alike and this nature is reflected in Curie temperature because though in the calculations of Curie temperature Stoner Curie temperature was also involved. The diamonds in Figure 6.4 (d) represent the results of Stoner Curie temperature (T_c^S). Apart from much larger values the nature of variation is also non-linear. This is due to the

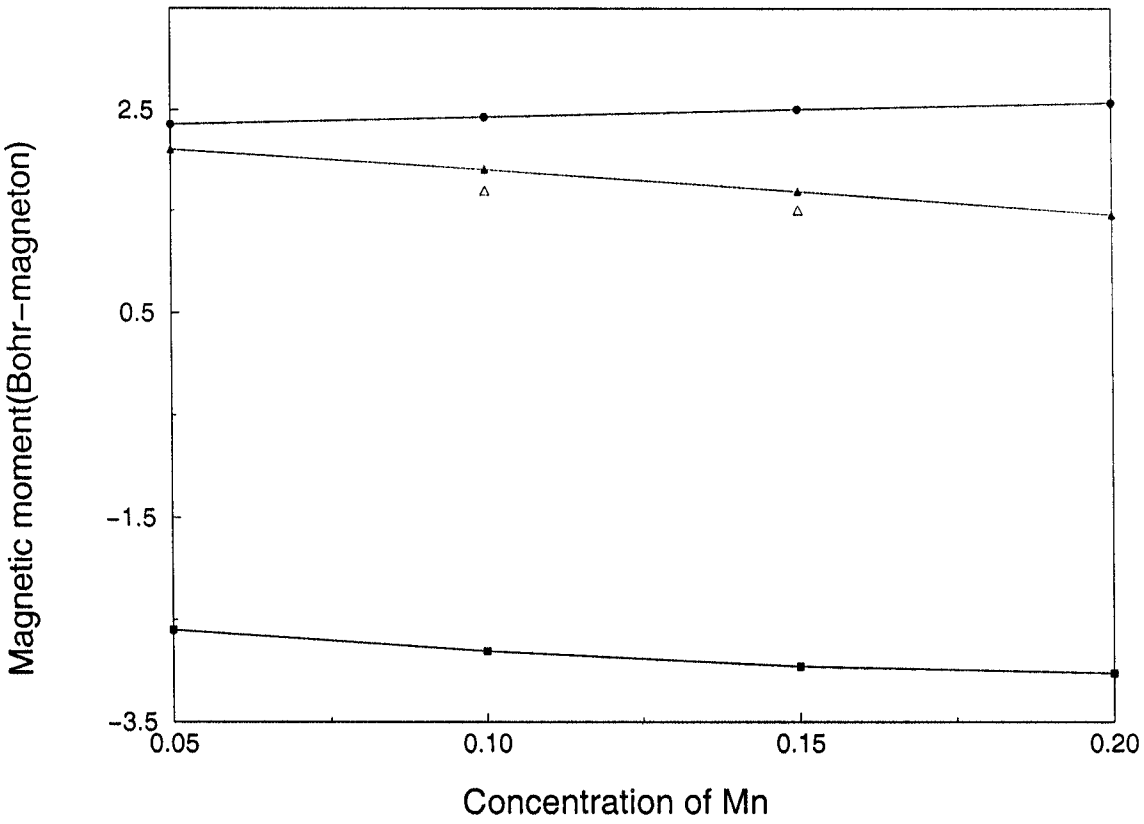

Figure 6.5: Partial and averaged magnetic moments (in Bohr-magneton/atom) vs. concentration of Mn for Mn_xFe_{1-x} alloy. The solid line with up triangles represents calculated averaged values, the solid line with filled circles represents calculated Fe moments, the solid line with filled squares represents calculated Mn moments. The open up triangles are the experimental values of average moments.

fact that T_c^S measures the temperature at which the paramagnetic state becomes unstable rather than the magnetic transition temperature.

Figure 6.5 shows the variation of average and local magnetisation in Mn_xFe_{1-x} alloys with Mn concentration.The filled triangles stand for average value while the filled circles and filled squares represent Fe and Mn local moments respectively. Unfortunately, enough experimental data is not available in this region to support our results. The experimental results so far available (shown by open triangles) (Fisher (1995)) agree well with our results. Our results also agree to a reasonable

extent with the calculations based on Hartree-Fock-CPA (Hasegawa and Kanamori (1972)) qualitatively but the variation of Mn local moment doesn't agree qualitatively with KKR-CPA results (Kulikov and Demangeat (1997)). In our case the Mn local moment linearly decreases with increasing Mn concentration, a feature obtained in Hartree-Fock-CPA calculations, too but the KKR-CPA results predict opposite trend for Mn moment. The Fe moment weakly increases and the average moment decreases with the Mn concentration, which is in qualitative agreement with the experimental Slater-Pauling curve (Fisher (1995)).

These variations can be explained once again using band filling (Figure 6.6) and density of states (Figure 6.7) results. Figure 6.6 (b) shows an almost constantly filled Fe up and down bands across the concentration regime thereby supporting the weak variation in Fe local moment. In case of Mn, the filling accommodates more number of electrons in the minority band (Figure 6.6 (c)). As a result, the minority band of the alloy gets gradually filled up while a loss of electrons from majority bands occur (Figure 6.6 (a)).

This feature is manifested in density of states as well as in variation of $n(E_F)$ (Figure 6.8 (a)). For majority spin states the filling of majority band at Fe site reduces $n(E_F)$ for the corresponding band while increasing Mn content shifts fermi level to regions of low spin up density of states and high spin down density of states because of gradual filling of minority electrons.

Once again, these phenomena can be explained on the basis of interplay of local charge neutrality, hybridisation and magnetic exchange. Unlike Co, Mn d level exchange splitting varies quite considerably of the order of 30 mRy due to gradual filling of minority band and de-populating of majority band. As a result, Mn local moment decreases as one goes to Mn rich region. In Fe, since both the bands are nearly filled and a very weak variation of number of local electrons is observed the local exchange splitting varies of the order of 14 mRy only (Table 6.2). Hence Fe local moment increases, though quite weakly compared to Mn.

The role of hybridisation and charge re-distribution can be addressed as follows. A close look at density of states reveals that unlike FeCo, the disorder is appreciable in both the bands. For the majority band, δ increases upto 50 mRy while $\delta^{\downarrow}$ increases around 8 mRy only. As Mn concentration is increased, the bonding part of spin-up

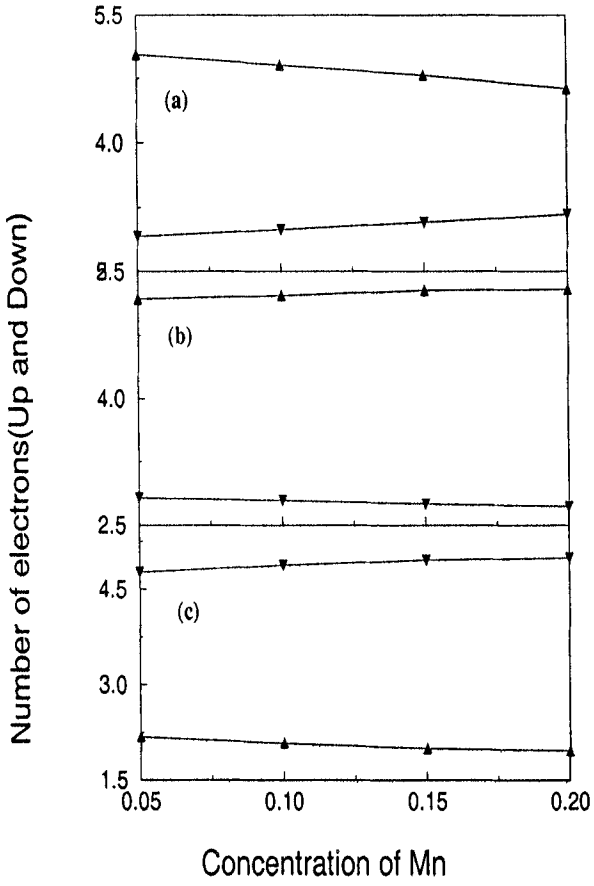

Figure 6.6: (a) represents average number of valence electrons for both spins vs. concentration of Mn for Mn_xFe_{1-x} alloy. The up triangles are for spin-up electron number and the down triangles are for spin-down electron number. (b) represents number of electrons at Fe site for both spins vs. concentration of Mn. The up and down triangles stand for up and down spin electrons respectively. (c) represents number of electrons at Mn site for both spins. The symbols represent identical things as (a) and (b).

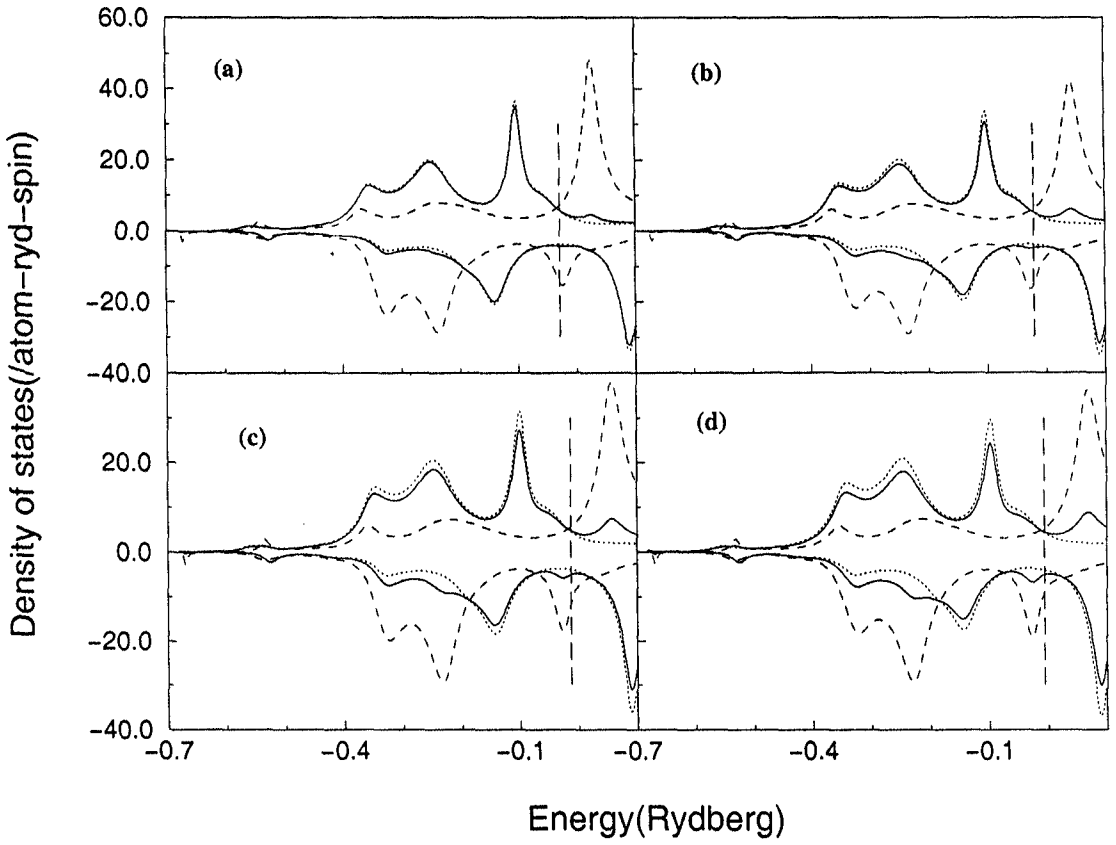

Figure 6.7: Spin projected partial and averaged densities of states/atom of Mn_xFe_{1-x} alloy. The various panels are for different concentrations of Mn- (a)5% (b)10% (c)15% (d)20% . In all the cases, the solid line represents averaged density of states while the dashed and the dotted line stand for Mn and Fe partial density of states respectively.

x_{Mn}	Δ_e^{Fe}	Δ_e^{Mn}
0.05	0.177	-0.170
0.1	0.183	-0.187
0.15	0.188	-0.197
0.2	0.191	-0.202

Table 6.2: Local exchange splitting values (in Ryd) in Mn_xFe_{1-x} with varying concentration of Mn

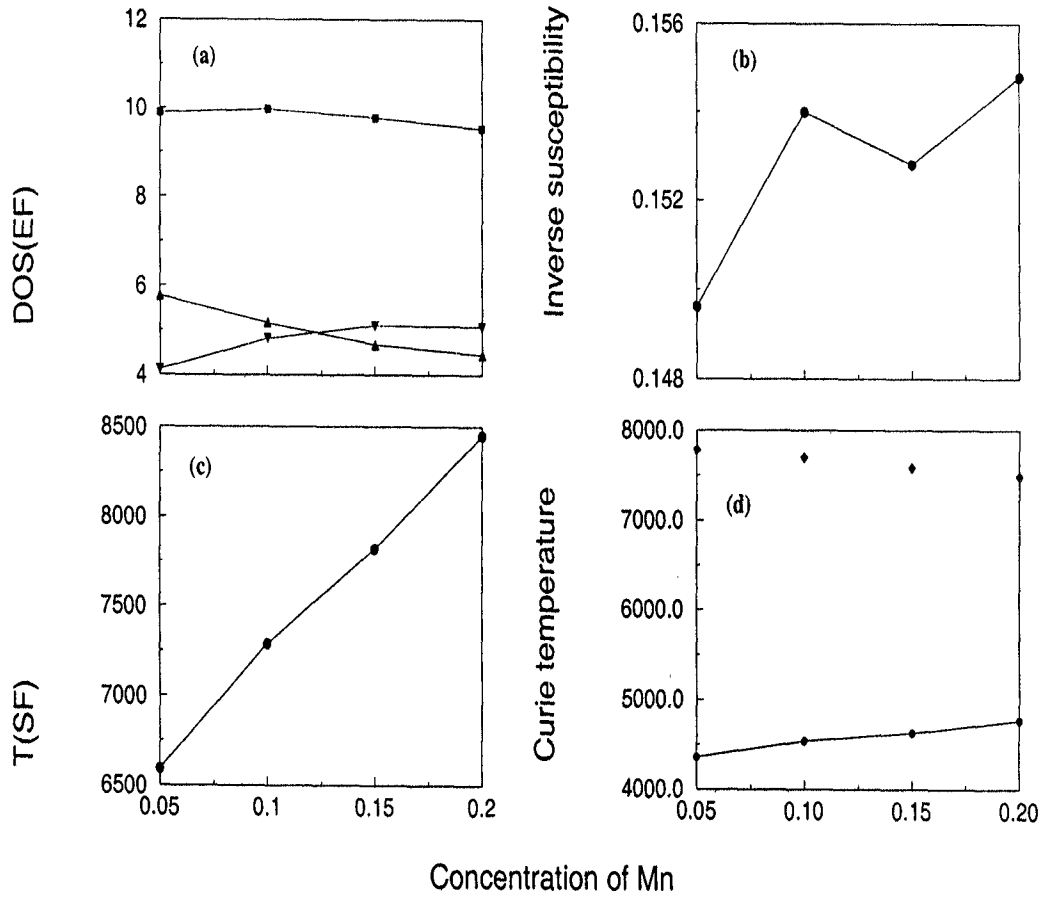

Figure 6.8: (a) represents density of states at fermi level for both spins as well as the averaged values vs. concentration of Mn in Mn_xFe_{1-x} alloy. The up and down triangles stand for values of up and down spins respectively while the squares stand for averaged values. (b) represents averaged inverse spin susceptibilities ($2\mu_B^2/\chi$ in Ryd-atom vs. concentration of Mn in Mn_xFe_{1-x} alloy. The circles represent the calculated values. (c) represents variation of spin fluctuation temperature (T_{SF}) in kelvin vs concentration of Mn in Mn_xFe_{1-x} (d) the solid line and the filled circles represent the variation of Curie temperature (T_c) in kelvin calculated using MW model vs Mn concentration in Mn_xFe_{1-x}. The diamonds stand for the values of Stoner Curie temperature (T_c^S) in kelvin.

density of states is dominated by Fe while the anti-bonding part is dominated by Mn. The reverse situation is observed for spin down density of states. As a result, majority spins from Mn migrate to Fe and minority spins from Fe migrate to Mn. Thus an increase in Fe local moment is observed.Finally a transition of electrons from $Mn^{\uparrow}$ to $Mn^{\downarrow}$ state occurs reducing the Mn moment gradually.

Figure 6.8 (b)- (d) respectively show the results on inverse susceptibility, spin fluctuation temperature and T_c. The inverse susceptibility shows a non-linear behaviour and as a result unlike FeCo, we observe a variation of spin fluctuation temperature exactly opposite to that of magnetic moment. But, once again like FeCo, T_c reflects the behaviour of spin fluctuation temperature though T_c^S (shown by filled circles in Figure 6.8 (d)) behaves in a opposite way. These discrepancies are due to limitations of T_c^S itself which has been discussed in FeCo case.

Figure 6.9 shows the concentration dependence of local and average magnetic moments in Cr_xFe_{1-x} alloy. The solid up triangles represent the calculated average values while the solid circles and solid squares denote the Fe and Cr local moments respectively. Our average magnetisation results agree well with the experimental values (shown by open up triangles) (Ling (1995)) and other theoretical results (Kulikov and Demangeat (1997), Butler (1995), Hasegawa and Kanamori (1972)). In fact, for higher Cr concentrations the experimental points almost fall on the theoretical curve establishing good agreement. In case of local moments, our results for Fe agree considerably well with available experimental (Butler (1995)) results but there is quantitative difference in Cr moment values with those of earlier calculations (Kulikov and Demangeat (1997), Dedrichs (1991)). In our case, we obtain a larger negative value of Cr moment which though increases rapidly in the Cr-rich region but never changes its sign which has been observed in earlier theoretical calculations around x=0.7. However, this slight discrepancy doesn't affect the average properties at all as is seen from the quantitative agreement with the experiments. Even the qualitative nature of variation of local as well as average moments is well reproduced. As is seen from the figure, Fe moment remains almost constant upto around x=0.4 and then it decreases in the Cr-rich side but the nature of variation is pretty weak. The Cr moment on the other hand increases rapidly as Cr content is increased making the average value to drop down very fast and approaching zero in accordance

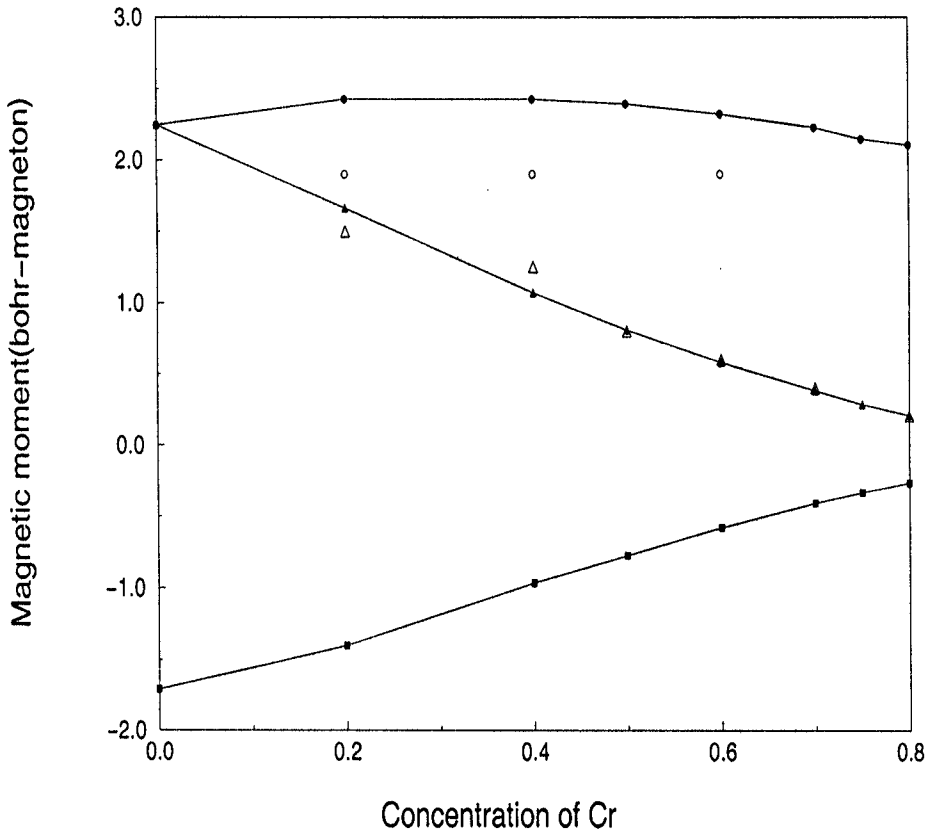

Figure 6.9: Partial and averaged magnetic moments (in Bohr-magneton/atom) vs. concentration of Cr for Cr_xFe_{1-x} alloy. The solid line with up triangles represents calculated averaged values, the solid line with filled circles represents calculated Fe moments, the solid line with filled squares represents calculated Cr moments. The open up triangles are the experimental values of average moments and the open circles are the experimental Fe moments.

with the established observation that the average moment collapses around x=0.8 due to transition from ferromagnetic to anti-ferromagnetic state.

Once again, we take recourse to the density of states (Figure 6.11) and variation of local and average number of electrons as number of valence electrons is decreased (Fe-rich to Cr-rich side) (Figure 6.10) to explain these behaviours. A thorough inspection of density of states for various concentrations show that E_F is positioned in a valley between the bonding-antibonding minority spin density of states. This feature explains the reason for linear variation of average moment because as we keep on increasing Fe content electrons are added to the majority spin states without much affecting minority spins. This feature is very clear in Figure 6.10 (a). The weak variation of Fe magnetic moment can also be explained likewise. The partial Fe density of states for both spins show little variation across the whole range of concentrations whereas the Cr minority density of states vary appreciably as we scan through the concentration regime. This is understandable if one looks into the variation of majority and minority electrons at each site. In case of Fe (Figure 6.10 (b)), both the majority and minority bands are almost completely filled while in case of Cr (Figure 6.10 (c)), the majority band accommodates more and more electrons as Cr-content is increased while the minority band looses and eventually they vary in such a way that at a certain critical concentration there will be more number of electrons in the majority band. Due to this behaviour of Cr, the average number of up electrons decrease (Figure 6.10 (a)) rapidly in contrast to almost constantly filled minority band in such a way that around x=0.8, the number of electrons in the majority band will be same as that of minority one establishing a collapse of magnetic moment when ferro-antiferro transition will take place.

The $n(E_F)$ variation supports this (Figure 6.12 (a)). Initially the fermi level is situated near the *d*-level peak in the majority band but as the Cr content is increased and majority band starts loosing electrons fermi level starts moving away from high density of states though initially in the Fe-rich region due to increase in Fe majority band electrons upto x=0.4 $n(E_F)$ had a weak rise. But as we step into Cr-rich region this effect is completely washed out. On the other hand since minority band is almost filled there is almost no variation in $n(E_F)^{\downarrow}$. As a result, the average $n(E_F)$ has a maxima around x=0.4.

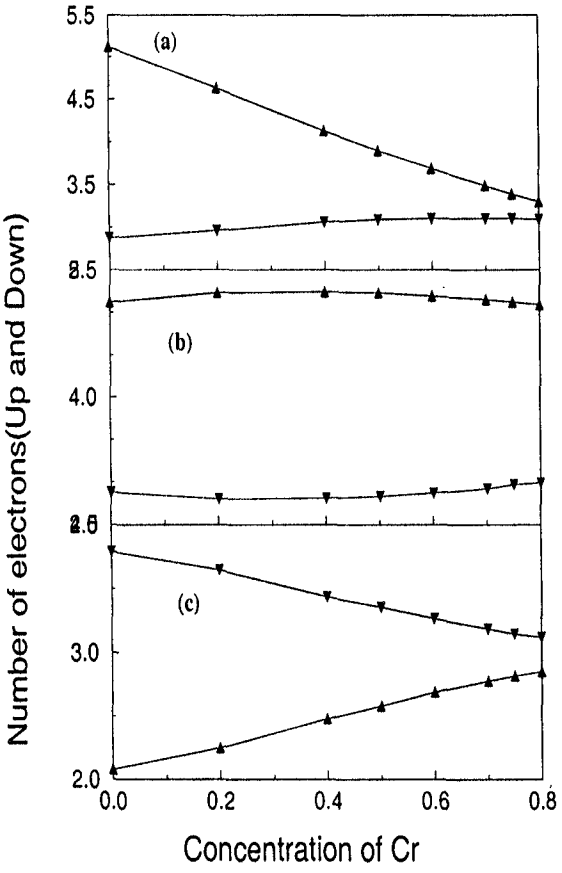

Figure 6.10: (a) represents average number of valence electrons for both spins vs. concentration of Cr for Cr_xFe_{1-x} alloy. The up triangles are for spin-up electron number and the down triangles are for spin-down electron number. (b) represents number of electrons at Fe site for both spins vs. concentration of Cr. The up and down triangles stand for up and down spin electrons respectively. (c) represents number of electrons at Cr site for both spins. The symbols represent identical things as (a) and (b).

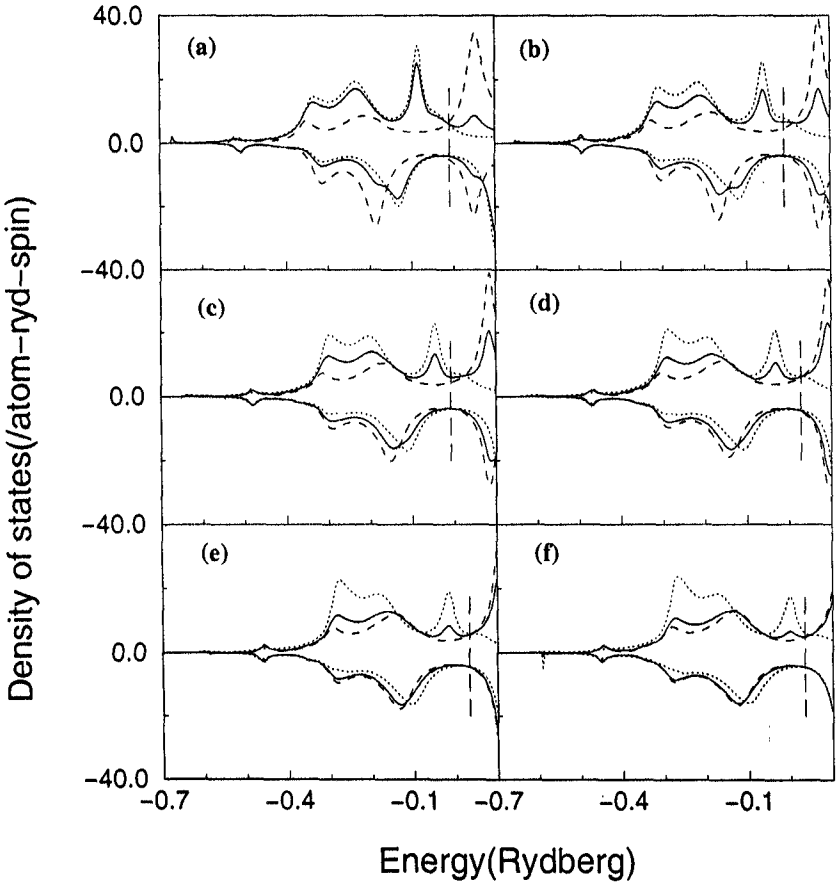

Figure 6.11: Spin projected partial and averaged densities of states/atom of Cr_xFe_{1-x} alloy. The various panels are for different concentrations of Cr- (a)25% (b)40% (c)50% (d)60% (e)70% (f)80%. In all the cases, the solid line represents averaged density of states while the dashed and the dotted line stand for Cr and Fe partial density of states respectively.

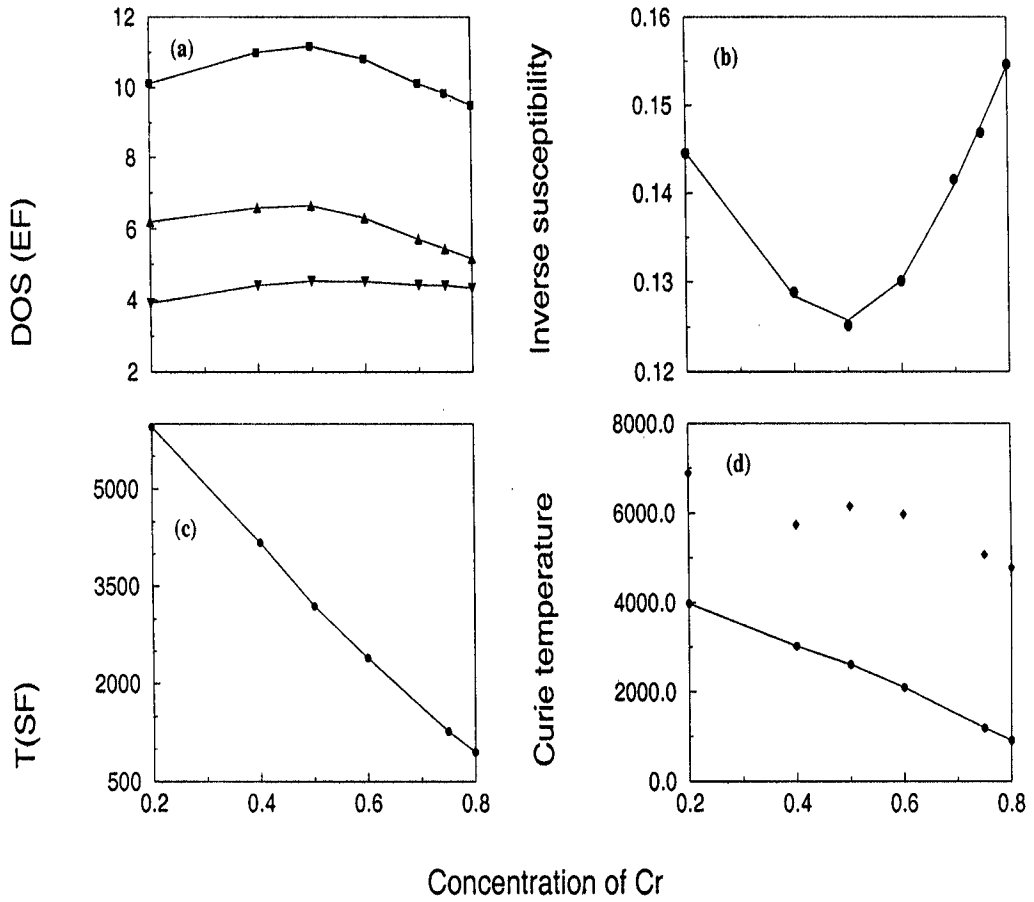

Figure 6.12: (a) represents density of states at fermi level for both spins as well as the averaged values vs. concentration of Cr in Cr_xFe_{1-x} alloy. The up and down triangles stand for values of up and down spins respectively while the squares stand for averaged values. (b) represents averaged inverse spin susceptibilities ($2\mu_B^2/\chi$ in Ryd-atom vs. concentration of Cr in Cr_xFe_{1-x} alloy. The circles represent the calculated values. (c) represents variation of spin fluctuation temperature (T_{SF}) in kelvin vs concentration of Cr in Cr_xFe_{1-x} (d) the solid line and the filled circles represent the variation of Curie temperature (T_c) in kelvin calculated using MW model vs Cr concentration in Cr_xFe_{1-x}. The diamonds stand for the values of Stoner Curie temperature (T_c^S) in kelvin.

x_{Cr}	Δ_e^{Fe}	Δ_e^{Cr}
.25	0.182	-0.080
0.4	0.179	-0.059
0.5	0.176	-0.047
0.6	0.171	-0.035
0.7	0.163	-0.024
.75	0.158	-0.020
0.8	0.154	-0.016

Table 6.3: Local exchange splitting values (in Ryd) in Cr_xFe_{1-x} with varying concentration of Cr

We now look for investigating the role of hybridisation, exchange etc and the type of charge distribution within the constraint of local charge neutrality. In Cr, the local exchange splitting varies more strongly than Mn and also in a opposite way. In case of Mn, exchange splitting decreased towards Mn-rich region whereas in this case, it increases as Cr content is increased (Table 6.3). The variation in the local exchange splitting for Cr varies of the order of 64 mRy from a Fe-rich to a Cr-rich region. This is due to the rapid de-filling of Cr minority band. In Fe, since both the bands are nearly filled, the local exchange splitting does not vary as much like that of Cr. Nevertheless, unlike Mn, it decreases and the variation is of the order of 28 mRy, explaining the decrease of Fe moment.

The charge-redistribution procedure in this case is quite different. Like FeCo, here the disorder in minority bands is stronger as is seen from the δ^σ values. $\delta^\downarrow$ varies from 9 mRy to 2 mRy from Fe-rich to Cr-rich side while $\delta^\uparrow$ remains around a value of -0.15 Ry. This stronger disorder in minority bands indicate a localization of majority electrons. As is seen from the density of states (Figure 6.11) both the bonding and anti-bonding part of spin down density of states is dominated by Cr. In case of majority band the bonding part is dominated by Fe and anti-bonding by Cr. Alongwith this the nature of variation of number of electrons for both spins at both the constituents (Figure 6.10) suggest that in this case, unlike the previous two, the electron redistribution occurs mainly between $Cr^\uparrow$ and $Cr^\downarrow$ states. Electrons from

Cr minority band migrate to Cr majority band explaining the rapid increase of Cr moment.

Figure 6.12 (b) shows the variation of inverse spin susceptibility of the system with increasing Cr content. Since $n(E_F)$ has a maxima around x=0.4, this curve shows a minima around the same region. However, in the case of spin fluctuation temperature variation (Figure 6.12 (c)) there is no signature of this nature because the effect of magnetic moment variation is much stronger across the concentration region and hence the variation of Spin fluctuation temperature reflects the nature of variation of magnetic moment only. As is seen in the previous two systems, the MW Curie temperature too has a similar nature of variation (shown by solid line in Figure 6.12 (d)) while T_c^S values are much higher.

6.5 Conclusions

We have studied the magnetism in bcc based Fe alloys where the three constituents belong to the same row of the periodic table and consecutive nearest neighbours of Fe. We have restricted ourselves to the ferromagnetic regions of these alloys only. Our study reveals quite different natures of electronic redistributions among the constituents as we go along from Co to Cr producing different nature of variation of magnetisation, Curie temperature,spin susceptibility etc. We have shown the dominant role of hybridisation and magnetic exchange under the constraint of local charge neutrality to explain successfully the variations in magnetic properties of the alloys of nearest neighbours in periodic table.

Chapter 7

Effect of short range order on electronic and magnetic properties of disordered Co based alloys

7.1 Introduction

The magnetic and chemical interactions in solid solutions, their interdependence and the role they play in determining the electronic and magnetic properties of transition metal alloys have been the subject of extensive experimental investigation (Cadeville and Morán-Lopéz (1987)). Several phenomenological models based on statistical thermodynamic aspects of phase stability are available to describe the interplay between magnetism and spatial order (Sato *et al* (1959), Swalin (1962), Vonsovskii (1974), Hennion (1983), Bieber *et al* (1981), Bieber and Gautier (1981), Bieber and Gautier (1986)).

Apart from this, there is one more approach of understanding the interplay between magnetism and ordering in transition metal alloys which involves investigation of the influence of local environment on electronic and magnetic properties of these alloys. A considerable amount of literature exists concerning the local (short-range) order in transition metal alloys obtained through measurements of X-ray or neutron diffuse scattering, nuclear magnetic resonance and Mössbauer spectroscopies (Mirebeau *et al* (1982), Pierron-Bohnes *et al* (1985), Mirebeau *et al* (1985), Pierron-

[1] The contents of this chapter has been published in Ghosh, Basu Chaudhuri, Sanyal and Mookerjee, *J. Magn. Magn. Mater.* **234** 100 (2001)

Bohnes *et al* (1982)). In order to explain the experimental results and describe the inhomogeneous character of magnetism in these alloys many phenomenological models (Jaccarino and Walker (1965), Marshall (1968), Hicks (1970)) as well as electronic structure calculations based on both zero and finite temperature models (Hasegawa and Kanamori (1971), Butler (1973), Jo and Miwa (1976), Jo (1976), Hasegawa (1979), Hamada (1979), Kakehashi (1982)) have been elaborated. The effect of local environment in disordered alloys can be described in terms of short-range order(SRO) because the degree of SRO determines the extent to which spatial correlations exist in these systems. This approach has been adopted by many workers in recent times in the framework of *ab-initio* electronic structure calculations (Borici-Kuqo *et al* (1998), Lu *et al* (1997), Wolverton *et al* (1998), Abrikosov (1996)).

The macroscopic state of SRO for a disordered binary alloy is characterized by Warren-Cowley SRO parameter (Cowley (1950)), which is given by

$$\alpha_r^{AB} = 1 - \frac{P_r^{AB}}{y} \tag{7-1}$$

where the A atom is at the center of the r^{th} shell, y denotes the macroscopic concentration of species B and P_r^{AB} is the pair probability of finding a B atom anywhere in the r^{th} shell around an A atom.

In the above mentioned approach, the workers either calculated the SRO parameters for a certain degree of disorder using first principles techniques and investigated the effect on ordering behavior of the systems (Lu *et al* (1997), Wolverton *et al* (1998), Staunton (1994), Johnson (1994)) or extracted the SRO parameters from experiments and observed its effect on electronic structure and properties (Borici-Kuqo *et al* (1998), Abrikosov (1996)).

In this chapter, we present the effect of SRO on the magnetic properties and the ordering behaviour of Co based alloys. For our investigations, we have chosen Co_xPt_{1-x} and Co_xPd_{1-x} alloys. Both the systems have been studied extensively over the years. In recent times they have received special attention due to their potentiality of being used as a recording medium in a new generation of storage devices. For these reasons lots of work on optical and magneto-optical characterization of these

systems are available in recent literatures (Uba (1998), Geerts (1994), Weller *et al* (1994)). Theoretical calculations include anisotropic electrical resistivity studies by Ebert *et al* (1996), investigation of electronic structure and magnetic properties of ordered CoPt alloys by Kashyap *et al* (1999), study of magnetism in disordered CoPt alloys by Ebert *et al* (1992) and calculation of ground state properties of CoPt by Shick *et al* (1996). But, the interesting problem of interrelations of magnetism and local ordering has failed to draw much attention. The interplay between these two phenomena is quite complicated which has been studied experimentally by Sanchez and Morán-López (1989). To our knowledge no such investigation has been done so far for CoPd. Hence,in this work we make an attempt to understand the influence of short-range order on magnetic and electronic properties in these systems from a first principles viewpoint. Our purpose is to understand and compare these iso-electronic systems with respect to their responses to degree of short range ordering. In particular, we look at the behaviour of partial and average magnetic moments, Curie temperatures and band energies with varying alloy compositions and degrees of SRO.

7.2 Theoretical Details

Our calculations are based on the generalized augmented space recursion (ASR) technique (Mookerjee and Prasad (1993), Saha *et al* (1994), Sanyal *et al* (1998)). The effective one electron Hamiltonian within the local spin density approximation (LSDA is constructed in the framework of the tight-binding linearized muffin tin orbitals (TB-LMTO) method (Andersen *et al* (1985)). The Hamiltonian is sparse and therefore suitable for the application of the recursion method of Haydock *et al* (1972) and Haydock (1982). The ASR allows us to calculate the configuration of the Green functions including short ranged ordering in the Hamiltonian parameters. It does so by augmenting the Hilbert space spanned by the tight-binding basis by the configuration space of the random Hamiltonian parameters. The configuration average is expressed *exactly* as a matrix element in the augmented space. Details of this methodology has been presented in the previous chapter. Here we shall quote the key results of generalized TBLMTO-ASR for short-ranged ordering. The

augmented space Hamiltonian with short range order is written as

$$\begin{aligned}
\hat{H} &= H_1 + H_2 \sum_R P_R \otimes P_\downarrow^R + H_3 \sum_R P_R \otimes (T_{\downarrow\uparrow}^R + T_{\uparrow\downarrow}^R) + \ldots \\
&+ H_4 \sum_R \sum_{R'} T_{RR'} \otimes \mathcal{I} + \alpha H_2 \sum_{R''} P_{R''} \otimes P_\downarrow^1 \otimes (P_\uparrow^{R''} - P_\downarrow^{R''}) + \ldots \\
&+ H_5 \sum_{R''} P_{R''} \otimes P_\downarrow^1 \otimes (T_{\uparrow\downarrow}^{R''} + T_{\downarrow\uparrow}^{R''}) + \ldots \\
&+ H_6 \sum_{R''} P_{R''} \otimes P_\downarrow^1 \otimes (T_{\uparrow\downarrow}^{R''} + T_{\downarrow\uparrow}^{R''}) + \ldots \\
&+ \alpha H_2 \sum_{R''} P_{R''} \otimes (T_{\uparrow\downarrow}^1 + T_{\downarrow\uparrow}^1) \otimes (P_\uparrow^{R''} - P_\downarrow^{R''}) + \ldots \\
&+ H_7 \sum_{R''} P_{R''} \otimes (T_{\uparrow\downarrow}^1 + T_{\downarrow\uparrow}^1) \otimes (T_{\uparrow\downarrow}^2 + T_{\downarrow\uparrow}^2) \qquad (7\text{-}2)
\end{aligned}$$

where R'' belongs to the set of nearest neighbours of the site labelled 1, at which the local density of states will be calculated. P's and T's are the projection and transfer operators either in the space spanned by the tight-binding basis $\{|R\rangle\}$ or the configuration space associated with the sites R , $\{|\uparrow_R\rangle, |\downarrow_R\rangle\}$ as described by Biswas *et al* (1995). The different terms of the Hamiltonian are given below.

$$\begin{aligned}
H_1 &= A(C/\Delta)\Delta_\lambda - (EA(1/\Delta)\Delta_\lambda - 1) \\
H_2 &= B(C/\Delta)\Delta_\lambda - EB(1/\Delta)\Delta_\lambda \\
H_3 &= F(C/\Delta)\Delta_\lambda - EF(1/\Delta)\Delta_\lambda \\
H_4 &= (\Delta_\lambda)^{-1/2} S_{RR'} (\Delta_\lambda)^{-1/2} \\
H_5 &= F(C/\Delta)\Delta_\lambda [\sqrt{(1-\alpha)x(x+\alpha y)} + \sqrt{(1-\alpha)y(y+\alpha x)} - 1] \\
H_6 &= F(C/\Delta)\Delta_\lambda [y\sqrt{(1-\alpha)(x+\alpha y)/x} + x\sqrt{(1-\alpha)(y+\alpha x)/y} - 1] \\
H_7 &= F(C\Delta)\Delta_\lambda [\sqrt{(1-\alpha)y(x+\alpha y)} - \sqrt{(1-\alpha)x(y+\alpha x)} \\
A(Z) &= xZ_A + yZ_B \\
B(Z) &= (y-x)(Z_A - Z_B) \\
F(Z) &= \sqrt{xy}(Z_A - Z_B) \qquad (7\text{-}3)
\end{aligned}$$

α is the nearest neighbour Warren-Cowley parameter described earlier. λ labels the constituents. C's and Δ's are the potential parameters describing the atomic

scattering properties of the constituents and S is the screened structure constant describing the underlying lattice which is fcc in the present case. For convenience, all the angular momentum labels have been suppressed, with the understanding that all potential parameters are 9×9 matrices. First of all, we note that in absence of short-ranged order ($\alpha = 0$), the terms H_5 to H_7 disappear and the Hamiltonian reduces to the standard one described earlier (Biswas *et al* (1995)).

The initial TB-LMTO potential parameters are obtained from suitable guess potentials as described in the article by Andersen and Jepsen (1984). In subsequent iterations the potentials parameters are obtained from the solution of the Kohn-Sham equation,

$$\left\{-\frac{\hbar^2}{2m}\nabla^2 + V^{\nu\sigma} - E\right\}\phi^{\nu}_{\sigma}(r_R, E) \;=\; 0 \qquad (7\text{-}4)$$

where,

$$V^{\lambda\sigma}(r_R) \;=\; V^{\lambda\sigma}_{core}(r_R) + V^{\lambda\sigma}_{har}(r_R) + V^{\lambda\sigma}_{xc}(r_R) + V_{mad} \qquad (7\text{-}5)$$

here λ refers to the species of atom sitting at R and σ the spin component. The electronic position within the atomic sphere centered at R is given by $r_R = r - R$. The core potentials are obtained from atomic calculations and are available for most atoms. For the treatment of the Madelung potential, we follow the procedure suggested by Drchal *et al* (1994). We choose the atomic sphere radii of the components in such a way that they preserve the total volume on the average and the individual atomic spheres are almost charge neutral. This ensures that total charge is conserved, but each atomic sphere carries no excess charge. In doing so, we had to be careful so that the spheres do not overlap much to violate the atomic sphere approximation.

The local magnetic moment, Curie temperature and the Spin-Fluctuation temperatures have been described in the earlier chapter.

7.3 Computational Details

For all the calculations, we have used a real space cluster of 400 atoms and an augmented space shell up to the sixth nearest neighbour from the starting state. Eight pairs of recursion coefficients were determined exactly and the continued fraction was appended with the analytic terminator of Luchini and Nex (1987). In the paper, Ghosh *et al* (1997) have shown the convergence of the related integrated quantities, like the Fermi energy, the band energy, the magnetic moments and the charge densities, within the augmented space recursion. The convergence tests suggested by the authors were carried out to prescribed accuracies. We noted that at least eight pairs of recursion coefficients were necessary to provide Fermi energies and magnetic moments to required accuracies. We have reduced the computational burden of the recursion in the full augmented space by using the local symmetries of the augmented space to reduce the effective rank of the invariant subspace in which the recursion is confined (Saha *et al* (1996)) and using the seed recursion methodology (Ghosh *et al* (1999)) with fifteen energy seed points uniformly across the spectrum. The exchange-correlation potential of Von Barth and Hedin has been used. s, p and d orbitals were used to construct the basis functions and scalar relativistic corrections were included.

7.4 Results and Discussion

We have performed total energy calculations for CoPd and CoPt alloys for several concentrations of Co to obtain the ground state lattice parameters. Energy convergence was set for 0.01 mRy. The results are shown in figure 7.1. It is seen that for both CoPd and CoPt, there is a deviation from Vegard's law values(shown by dashed lines) though the trends are same. In both the cases, equilibrium lattice parameters decrease with the increase in Co concentrations. Shick *et al* (1996) obtained the equilibrium lattice parameter for $Co_{50}Pt_{50}$ to be 7.049 a.u. using fully relativistic TBLMTO-CPA in frozen core approximation. Both their value and our calculated value of 6.921 a.u. are less than the experimental lattice parameter of 7.10 a.u. (Wijn and Landolt-Bornstein (1986)). This is not surprising as LSDA

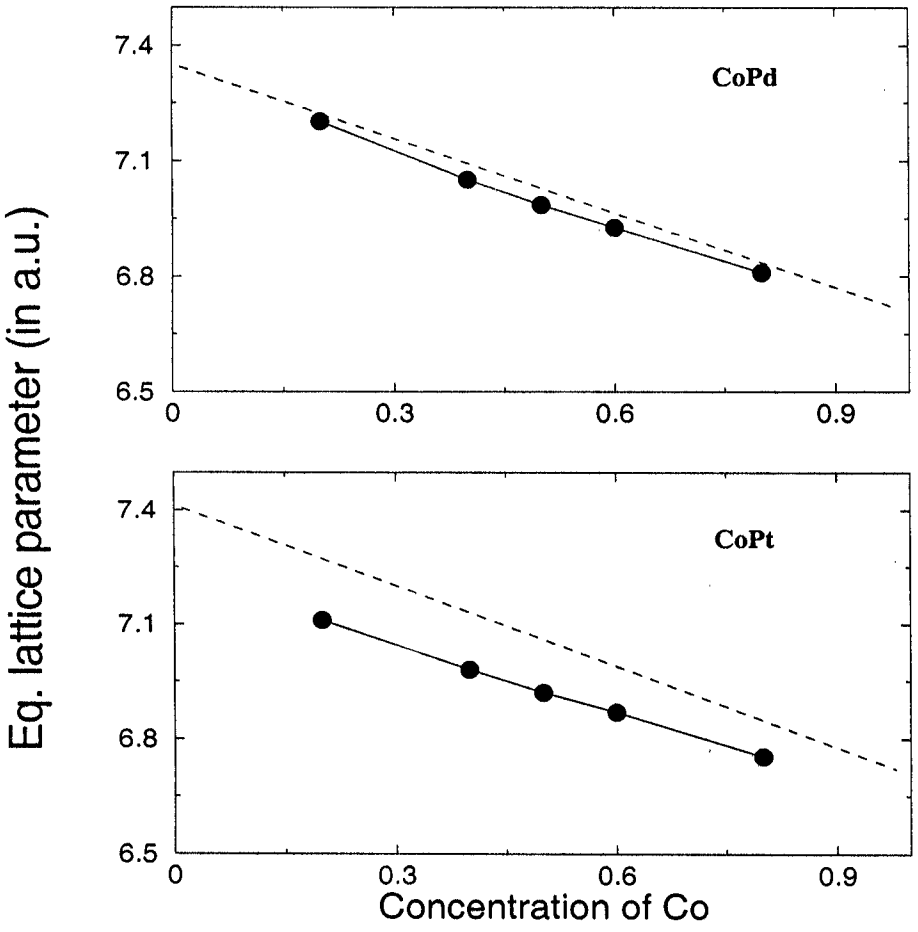

Figure 7.1: Equilibrium lattice parameters (in a.u.) vs. concentration of Co for (top) CoPd (bottom) CoPt alloys. The circles represent the calculated values whereas the dashed lines denote Vegard's law values.

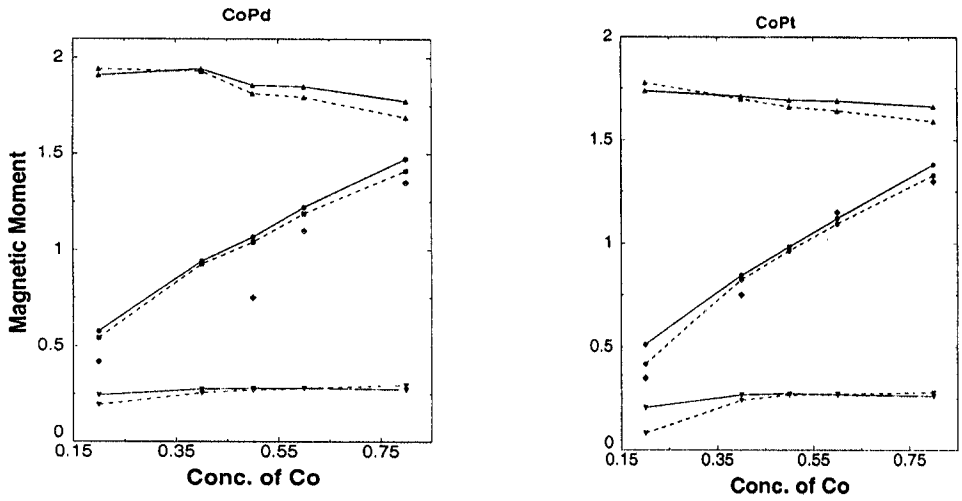

Figure 7.2: Partial and averaged magnetic moments (in Bohr-magnetons/atom) vs. concentration of Co in (a) CoPd (b) CoPt alloys. The full line is for disordered case and the dotted one for SRO state with α= -0.2. The symbols represent : filled up traingles, filled circles and filled down traingles are for Co partial moments, averaged moments and Pd/Pt partial moments respectively. Diamonds represent the experimental values of average magnetic moment in fully disordered case.

invariably overestimates bonding.

Results for magnetic moments of Co_xPd_{1-x} are shown in figure 7.2(a) while that of Co_xPt_{1-x} are shown in figure 7.2(b). It is seen that both Pd and Pt sites also acquire some induced moments from Co. Local magnetic moments of Co go down with increasing Co concentration but the changes are not significant. This is observed in ordered alloys too (Kashyap *et al* (1999)). This is a signature of weak local environmental effects on electronic structure. According to the calculation of Shick *et al* , the averaged and partial moments of Co and Pt in $Co_{50}Pt_{50}$ are 1.066, 1.787 and 0.345 μ_B respectively. We get the values of 1.049, 1.852 and 0.24 μ_B for

the same while both of the values for averaged magnetic moments are close to the experimental value of 1.05 μ_B (Wijn and Landolt-Bornstein (1986)). Theoretical results using other techniques are not available for Co_xPd_{1-x} systems. But,our results for both the systems agree well with experiment (Wijn and Landolt-Bornstein (1986)). As expected the LSDA estimate of the exchange field and hence the local magnetic moment is always larger than experimental values.

The value of Warren-Cowley SRO parameter for A_xB_y alloy is given by $-(x/y) \leq \alpha < 1$ where α=$-(x/y)$ implies full short-range ordering and α=1 implies complete segregation. In our case we have taken our α= -0.2 which is valid for the whole range of concentrations. The results for magnetic moments of CoPd and CoPt systems have been shown in dashed lines of figures 7.2 (a) and (b) respectively. The results show that the effect of SRO included through the given value of α on average magnetic moment is pretty weak. The difference in values of partial moments in the SRO state and fully disordered state is not uniform across the concentration axis for both the systems though the average moment in the SRO state is always less than that of fully disordered state. In case of CoPd, there is a crossover of partial moment value of both Co and Pd at certain concentrations with respect to the disordered value. At around 35%, the Co partial moment in the SRO state becomes less than that of disordered phase and this trend follows for the higher concentrations of Co. For Pd, however, the change is observed at around 55% but the quantitative difference with disordered phase in case of Pd is almost negligible. Exactly the same trend is observed in case of CoPt systems.

Results for MW and Stoner Curie temperatures for CoPd and CoPt are shown in figures 7.3 (a) and (b) respectively. MW Curie temperatures for both the systems are in good agreement with the experiments (Wijn and Landolt-Bornstein (1986)). On the other hand Stoner Curie temperatures are highly overestimated. This is not surprising since we should realize that Stoner Curie temperature measures the temperature at which the paramagnetic state becomes unstable rather than the magnetic transition temperature. This overestimation is much reduced in the MW model (Mohn and Wohlfarth (1987)) which combines two extreme theories- the single particle excitation and collective particle excitations. Again, the theoretical Curie temperatures are higher than experimental values due to the same reason as

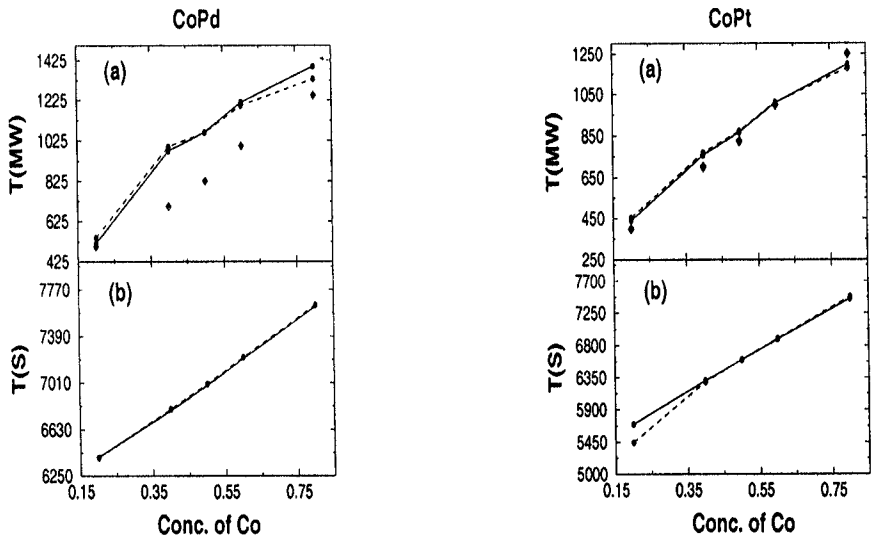

Figure 7.3: Curie temperature (in Kelvin) vs. concentration of Co in (a) CoPd and (b) CoPt alloys. Panel(a): MW Curie temperature results. Full line represents fully disordered case. Dashed line represents SRO state characterized by α=-0.2. Diamonds represent experimental points for fully disordered case. Panel(b): Stoner Curie temperature results. Full and dashed lines refer to the same results as in (a).

described in case of magnetic moments.

The results for Curie temperatures in SRO state of CoPd and CoPt are shown in figures 7.3 (a) and (b) by dashed lines. The Stoner Curie temperatures for both the systems are almost unaffected by SRO. The influence in MW Curie temperatures is also less. Yet, there is a difference in behaviour (quantitatively) with respect to fully disordered state at around 50% for both the systems. Around 50% of Co, the difference in magnitude of Curie temperature of SRO state and disordered state changes from positive to negative value.

Figure 7.4 shows the partial densities of states for equi-atomic CoPd and CoPt alloys with SRO parameter -1.0, 0.0 and 1.0. While going from the short-ranged ordering side (-1.0) to the segregation side (1.0) we find distinct changes in local DOS. The DOS for majority and minority electrons shift relative to each other and bring change in magnetic moments. For CoPd alloy, the average magnetic moment is increased from 0.96 μ_B/atom to 1.24 μ_B/atom while going from α= -1.0 to 1.0. The change is from 0.88 μ_B/atom to 1.09 μ_B/atom in case of CoPt.

To have a complete understanding of the ordering tendency and effect of local ordering on magnetism in these systems we now carry out calculations for the full range of α at different concentrations. Figures 7.5 show the panels containing results for magnetic moments, electronic band energies and MW Curie temperatures for $Co_{20}Pd_{80}$, $Co_{50}Pd_{50}$ and $Co_{80}Pd_{20}$ respectively. It is observed that while at 20% concentration of Co, Co partial moment decreases towards the segregation side,it shows a reverse tendency at 50% and 80%. The Pd partial moment shows a rise toward the segregation side at 20% while at 50% and 80% it remains almost at a constant magnitude. To understand this behavioral difference of Co moment at different concentrations we present results of magnetic moment at 10% and 40% of Co in figures 7.6 (left) and (right) respectively. The results for 10% mimic that of 20% but the 40% case almost follows the higher concentration trends. This can be understood in the following way: As the system goes from ordering to the segregation side, more and more Co atoms club together to build up magnetic moment of Co but at lower concentrations (<40%) a Co atom finds itself in a completely non-magnetic Pd surrounding. Therefore the situation is like a magnetic impurity in a non-magnetic host which instead of building up rather subdues its moment as it

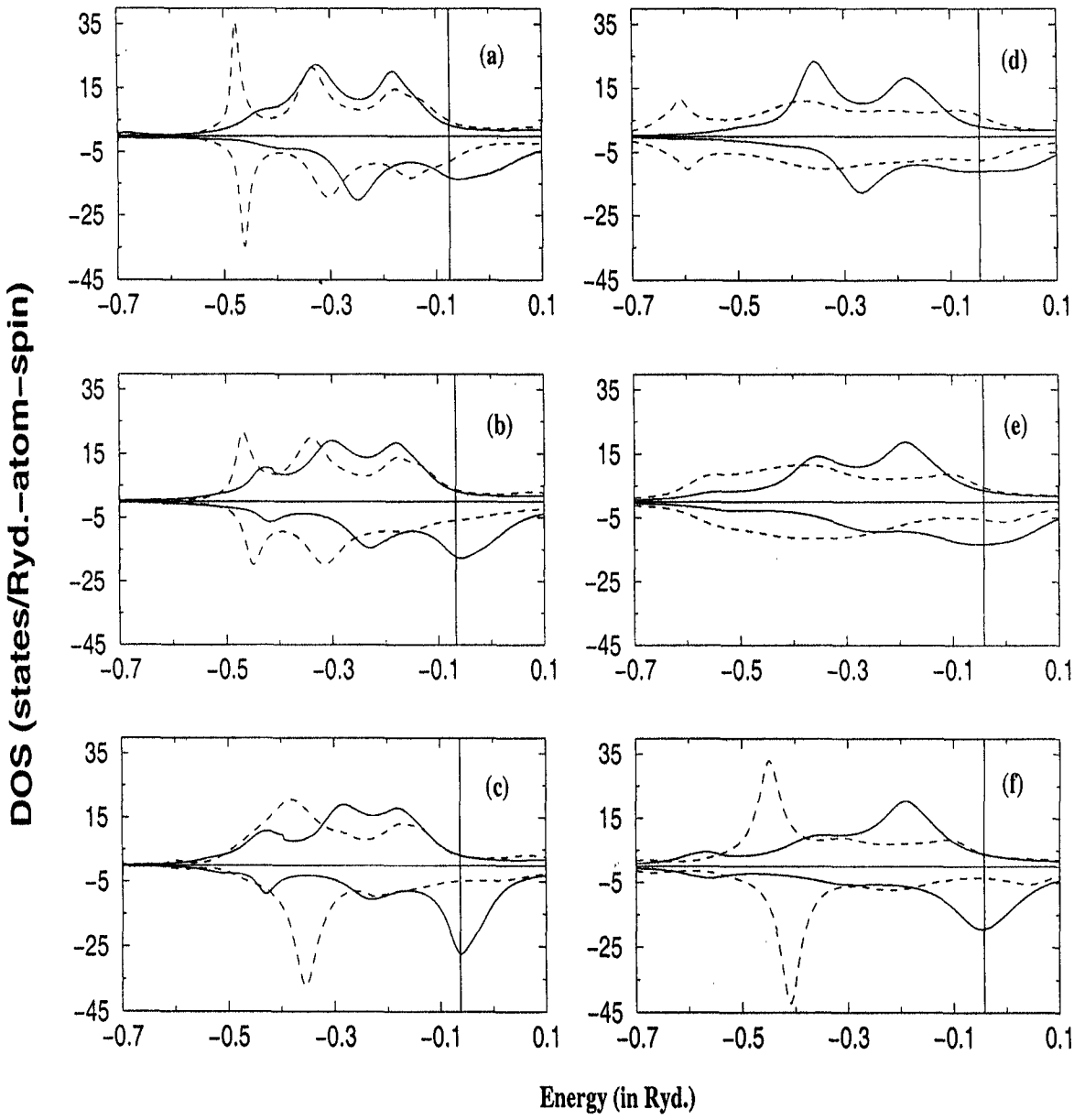

Figure 7.4: Spin and component projected local densities of states/atom of (a)-(c) $Co_{50}Pd_{50}$ and (d)-(f) $Co_{50}Pt_{50}$ alloys for SRO parameter equal to [(a) and (d)] -1.0 [(b) and (e)] 0.0 [(c) and (f)] 1.0. In all cases, the solid lines are for Co and the dashed lines are for Pd/Pt components. Vertical lines show the positions of Fermi levels.

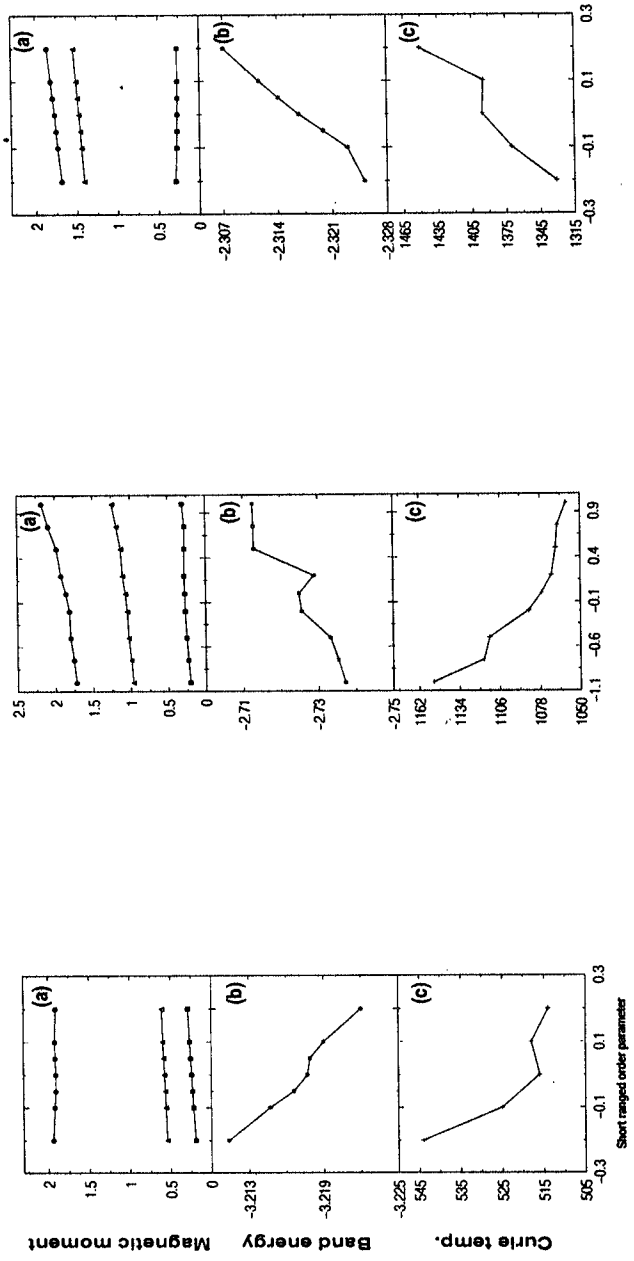

Figure 7.5: Variation of properties of CoPd alloys with Warren-Cowley short ranged order parameter. (left) $Co_{20}Pd_{80}$ (centre) $Co_{50}Pd_{50}$ and (right) $Co_{80}Pd_{20}$ alloys. Panels : (a) variation of partial and average magnetic moments (in Bohr magnetons /atom); symbols : filled circles, triangles and squares are for Co,average and Pd moments respectively. (b) variation of band energies (in Ryd.) (c) variation of MW Curie temperatures (in Kelvin).

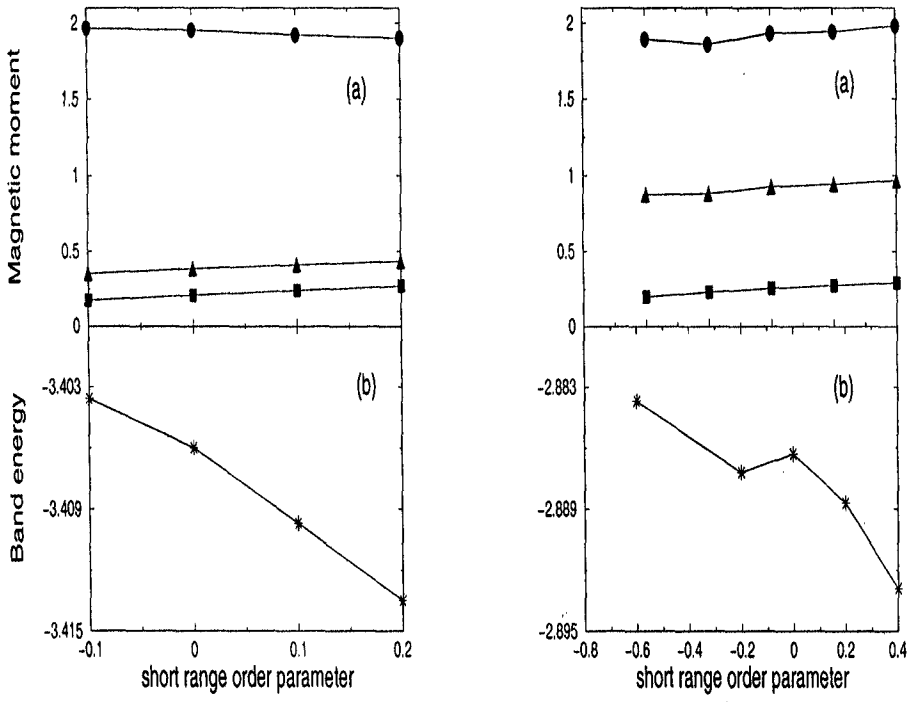

Figure 7.6: Variation of properties with SRO parameter for (left) $Co_{10}Pd_{90}$ and (right) $Co_{40}Pd_{60}$ alloys. Panels : (top) variation of partial and average magnetic moments ; symbols : filled circles, triangles and squares are for Co, average and Pd moments respectively. (bottom) variation of band energy.

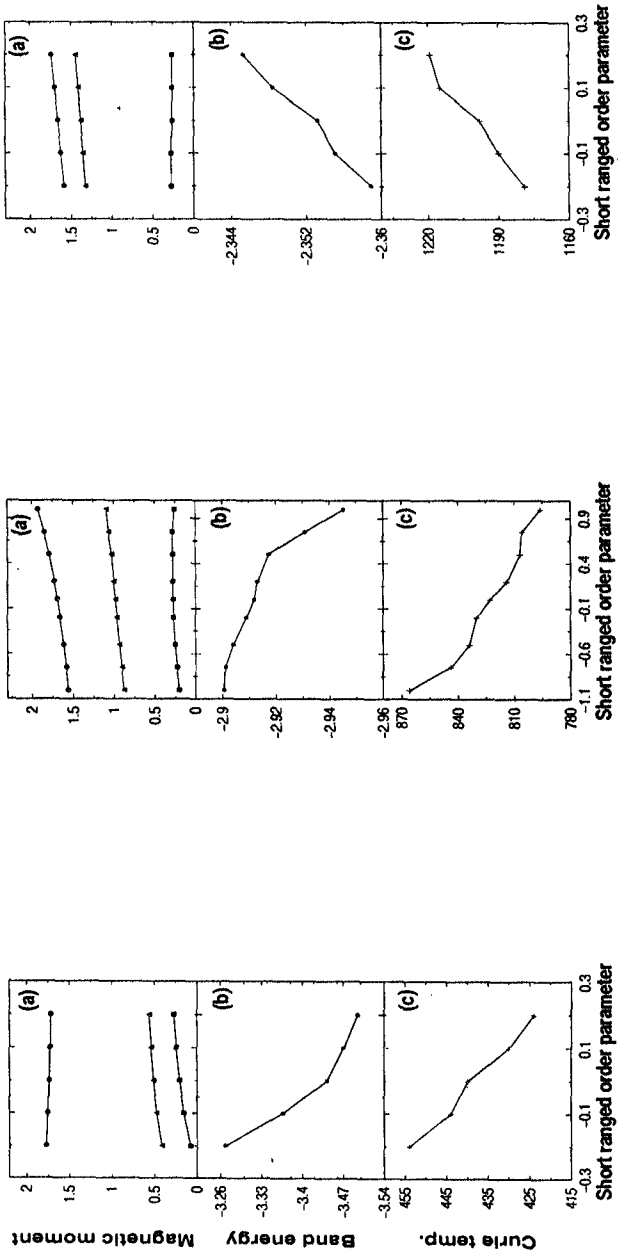

Figure 7.7: exactly as described for fig.7.5 but for CoPt alloys.

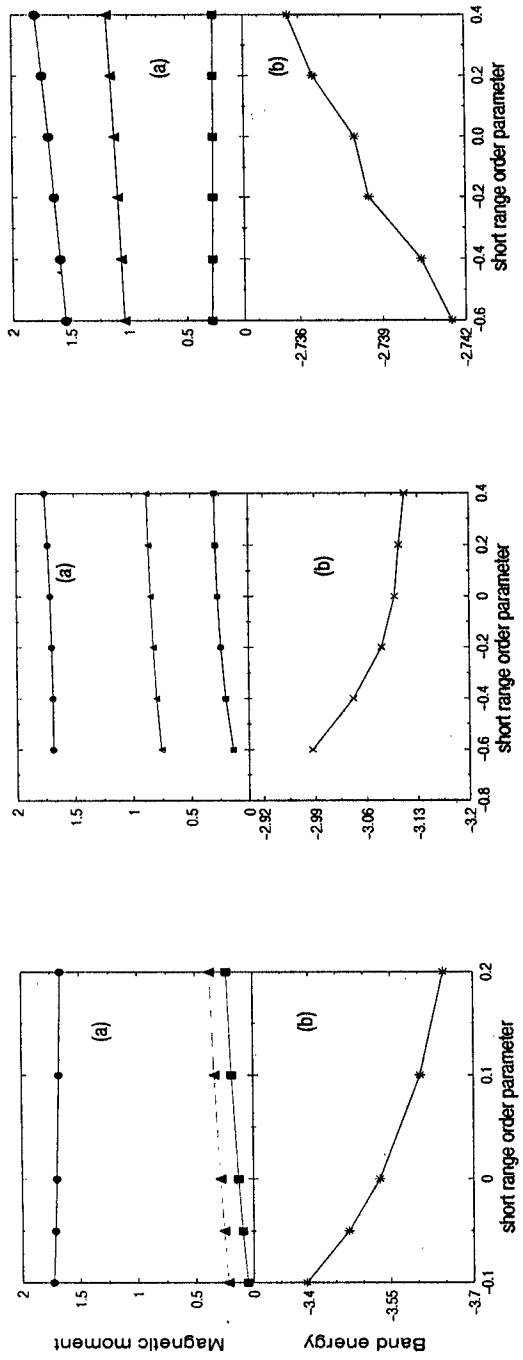

Figure 7.8: Variation of properties with SRO parameter for (left) $Co_{10}Pt_{90}$ (middle) $Co_{40}Pt_{60}$ and (right) $Co_{60}Pt_{40}$ alloys. Panels : (top) variation of partial and average magnetic moments ; symbols : filled circles, triangles and squares are for Co, average and Pt moments respectively. (bottom) variation of band energy.

goes toward the segregation side.

The middle panels containing the results for the band energies show that at 20% the system shows a tendency towards segregation while at 50% and 80% the tendency is towards ordering. To locate the region of the transition, figure 7.6 can be investigated which presents results on band energy for 40% Co. It is seen that at this concentration the system shows tendency toward segregation which means that the ordering behavior of the system changes between 40% and 50% of Co concentration.

The bottom panels show the variation of Curie temperature with SRO parameter. At 20% and 50% concentrations Curie temperatures are higher toward ordering side while the trend is opposite at 80%. In other words, at 20% and 50% ferromagnetic phases are stable up to higher temperatures in the ordering side while at 80% they are stable up to higher temperatures in the segregation side.

Figures 7.7 present the results for the same properties but for CoPt alloys. The nature of variation of the moments are exactly same as those of CoPd and hence can be explained using the same logic. The results for the band energies show that at 20% and 50% of Co, the system shows the tendency towards ordering while at 80% it tends to segregate. Once again to locate the region of transition the bottom panels of figures 7.8 are referenced. Here, the change in ordering behavior is observed at 60% of Co which indicates that unlike CoPd, this system has a tendency to segregate between 50% and 60% of Co. From the bottom panels of figures 7.7, it is seen that at all concentrations, Curie temperature is higher at higher band energy sides. It is indicative of the possibility that the ferromagnetic phases are stable up to a lower temperature at the minimum energy state of this system.

7.5 Conclusions

We have studied the effects of short range order on the magnetic and electronic properties of the Co_xPd_{1-x} and Co_xPt_{1-x} alloys using fully self consistent first principles techniques. Our results for completely disordered phases agree reasonably well with the experiments. The effect of SRO on magnetic moments, electronic band energies and Curie temperatures have been investigated in detail. CoPt shows a tendency to go to ordering state from clustering(segregation) state at around 60% of Co while

CoPd shows this tendency at around 40%. The response of Curie temperature to short-range ordering is linear in CoPt in the sense that at all concentrations it attains higher value at the energetically higher SRO states. For CoPd, the response is not that linear. At 20% and 80% concentrations higher values are observed at energetically higher SRO states.

Chapter 8

Conclusion

In this thesis we have used three different methodologies of electronic structure calculations : the tight-binding LMTO, the recursion method and the augmented space method. We have studied both the electronic and magnetic properties of a series of compounds and alloys. The aim was twofold : an in-depth understanding of the various methodologies available with us with their advantages and drawbacks ; and also to apply these to interesting systems of compounds and alloys. We have developed now a computationally efficient TB-LMTO based augmented space recursion package which is self-consistent in the LDA sense, incorporating different exchange-correlation functionals and including the GGA corrections. With this package we can deal not only with homogeneously disordered systems, but also include effects of short-ranged order and local structural disorder due to large size mismatch between the constituents. Charge transfer effects are effective and accurately taken into account.

The drawbacks of our methodology are all those of the basic ingredients.

Firstly, it has all the drawbacks of the LDA. Although metals are well described, semiconductor band gaps are severely underestimated. It is basically a ground state technique. Excited states are not described to any satisfactory detail. One way out will be to generalize our method to the GW technique. This is one of the aims of further research in our group.

Secondly, it has some of the drawbacks of the second generation TB-LMTO. Our application is within the atomic sphere approximation (ASA). Within the

recursion method, which requires a sparse, real space representation of the Hamiltonian, combined corrections has not been possible to be implemented. We are looking into the new third generation TB-LMTO as the basis of our representation. A fully LDA self-consistent version of this is still not available.

Technical improvements of the recursion method needs incorporation of the dynamical recursion ideas introduced by Haydock and co-workers. We intend to implement this in future.

It is our intention to pursue further work in these lines for the future.

Bibliography

Abrikosov I. A., *Phys. Rev. Lett.* **76** 4203 (1996)

Albe V., Jouanin C., and Bertho D., *Phys. Rev.* **B 57**, 8778 (1998)

Akai H. and Dederichs P.H., *Phys. Rev.* **B47** 8739 (1993)

Andersen O.K. *et al* Physica **B+C 86-88** 249-256 (1977)

Andersen O. K. and Jepsen O., *Phys. Rev. Lett.* **53**, 2581 (1984)

Andersen O.K., Jepsen O. and Glotzel G., *Highlights of Condensed-Matter Theory*, edited by Bassani F., Fumi F. and Tosi M. P. (North-Holland, New York), p. 59 (1985)

Arp V., Edmomnds D. and Petersen R. *Phys. Rev. Lett.* **3** 212 (1952)

A Asano, N. Yamashita, and Y. Naka, *Phys. Status Solidi* 663 (1978).

Bardos D.I., *J. Appl. Phys.* **40** 1371 (1969)

Basu Chaudhuri C., Pari G., Mookerjee A. and Bhattacharya A.K., *Phys. Rev.* **B60** 11846 (1999)

Bieber A., Gautier F., Treglia G. and Ducastelle F. *Solid state comm.* **39** 149 (1981)

Bieber A. and Gautier F. *Solid state comm.* **38** 1219 (1981)

Bieber A. and Gautier F. *Journal of Magnetism and Magnetic Materials* **54-57** 967 (1986)

Birch F., *Geophys. Res.* **83**, 1257 (1978).

Biswas P.P., Sanyal B., Fakhruddin M., Halder A., Mookerjee A. and Ahmed M., *J. Phys.: Condens. Matter* **7** 8569 (1995)

Blöchl P., Ph.D. Dissertation, Stuttgart University (1989)

Bluegel S., Akai H., Zeller R. and Dederichs P. H., *Phys. Rev.* **B 35** 3271 (1987)

Borici-Kuqo M., Monnier R. and Drchal V., *Phys. Rev.* **B58** 8355 (1998)

Born M. and Huang K., in *Dynamical Theory of Crystal Lattices*, (Clarendon, Oxford, 1954)

Burke S.K. and Rainford B.D., *J. Phys. F: Met. Phys.* **13** 441 (1983)

Butler W.H., *Phys. Rev.* **B8** 4499 (1973)

Butler W.H., Zhang X-G, Nicholson D. M. C. and MacLaren J. M., *Journal of Magnetism and Magnetic Materials* **151** 354 (1995)

Cadeville M.C.and Morán-López J. L., *Physics Reports* **153** 331(1987)

Carlsson A.E. and Wilkins J.W., *Phys. Rev.* **B29** 5836 (1984)

Ceperly D.M. and Alder B.J., *Phys. Rev. Lett.* **45** 566 (1980)

Cervantes P. and Williams Q., *Phys. Rev.* **B58** 9793 (1998)

Chadi D. J., *Phys. Rev. Lett.* **72**, 534 (1994)

Chandrasekhar S., *Radiative Transfer* (Dover, New York, 1960)

Cheng C.H., Wei C.T. and Beck P.A., *Phys. Rev.* **2** 426 (1960)

Child H.R. and Cable J.W. , *Phys. Rev.* **B13** 227 (1976)

Collins M.F. and Forsyth J.B., *Phil. Mag.* **8** 401 (1963)

Collins M.F. and Low G.G. , *Proc. Phys. Soc.* 2 **86** 535 (1965)

Cowley J.M., *J. Appl. Phys.* **21** 24 (1950)

Dandrea R.G. and Duke C.B., *Appl. Phys. Lett.* **64** 2145 (1994)

Dasgupta I., in Ph.D. thesis submitted to Calcutta University (1997)

Dederichs P.H., Zeller R., Akai H. and Ebert H., *Journal of Magnetism and Magnetic Materials* **100** 241 (1991)

Dicarlo J., Albert M., Dwight K., and Wold A., *J. Solid. State Chem.* **87**, 443 (1990)

Drchal V., Kudrnovský J. and Weinberger P., *Phys. Rev.* **B50** 7903 (1994)

Duffy T.S., Hemley R.J. and Mao H., *Phys. Rev. Lett.* **74** 1371 (1995)

Ebert H., Winter H., Johnson D. D., and Pinski F. J., *J. Phys.: Condens. Matter* **2** 443 (1990)

Ebert H., Drittler B. and Akai H., *Journal of Magnetism and Magnetic Materials* **104-107** 733 (1992)

Ebert H., Vernes A. and Banhart J., *Phys. Rev.* **B 54** 8479 (1996)

Endoh Y. and Ishikawa Y., *J. Phys. Soc. Japan* **30** 1614 (1971)

Fawcett E., Alberts H. L., Galkin V. Yu., Noakes D. R. and Yakhmi J.V., *Rev. Mod. Phys.* **66** 25 (1994)

Fernando G. W., Cooper B. R., Ramana M. V., Krakauer H. and Ma C. Q., *Phys. Rev. Lett.* **56** 2299 (1986)

Fisher H. *et al* in *Magnetic Ultrathin Films, Multilayers and Surfaces*, edited by A. Fert *et al*, MRS symposia proceedings No. 384 (Materials Research Society, Pittsburgh, 1995)

Furdyna J.K., *J. Appl. Phys.* **64**, R29 (1988)

Furuska M., Ishikawa Y., Yamaguchi Y. and Fujino Y., *J. Phys. Soc. Japan* **55** 2253 (1986)

Geerts W., *Phys. Rev.* **B 50** 12581 (1994)

Gersdorf R., *J. Phys. Radium* **23** 726 (1962)

Ghosh S., Das N. and Mookerjee A., *J. Phys.: Condens. Matter* **9** 10701 (1997)

Ghosh S., Das N. and Mookerjee A., *Modern Physics Letters* **B13** 723 (1999)

Gonser U., Krische K. and Nasu S., *Journal of Magn and Magn Materials* **15-18** 1145 (1980)

González-Díaz M., Rodríguez-Hernández P. and Muñoz A., *Phys. Rev.* **B55** 14043 (1997)

Gromakov S. D. and Partala A. I., *Zh. Fiz. Khim.* **43**, 267 (1969)

Grzybowski T.A. and Ruoff A.L. , *Phys. Rev.* **B27** 6502 (1983)

Grzybowski T.A. and Ruoff A.L. , *Phys. Rev. Lett.* **53** 489 (1984)

Gunnarson O., *J. Phys. F* **6** 587 (1976)

Hamada N., *J. Phys. Soc. Japan* **46** 1759 (1979)

Hasegawa H. and Kanamori J., *J. Phys. Soc. Japan* **31** 382 (1971)

Hasegawa H. and Kanamori J., *J. Phys. Soc. Japan* **33** 1607 (1972)

Hasegawa H., *J. Phys. Soc. Japan* **46** 1504 (1979)

Hasegawa H. and Pettifor D.G., *Phys. Rev. Lett.* **50** 130 (1983)

Haydock R., Heine V. and Kelly M.J., *J. Phys. C: Solid State Phys.* **5** 2845 (1972)

Haydock R., in *Solid State Physics*, **35** (Academic Press, New York) (1982)

Hennion M. *J. Phys. F: Met. Phys.* **13** 2351 (1983)

Hicks T.J., *Physics Letters* **A32** 410 (1970)

Hiraki K., *Journal of Phys. Soc. Japan* **58** 4288 (1989)

Hohenberg P. and Kohn W., *Phys. Rev.* **136** 864 (1964)

Hu C.D. and Langreth D.C., *Phys. Rev.* **B33** 943 (1986)

Inoue M., *J. Phys. Soc. Japan* **26**, 1186 (1969)

Ishikawa Y. in *Physics and Applications of INVAR Alloys*, edited by H. Saito, Honda Memorial Series on Materials Science No. 3 (Moruzen, Tokyo, 1978)

Jaccarino V. and Walker J.L., *Phys. Rev.* **15** 258 (1965)

Jackson M.D.and Gordon R.G., *Phys. Rev.* **B 38** 5654 (1988)

James P., Eriksson O., Johnson B. and Abrikosov I. A., *Phys. Rev.* **B 59** 419 (1999)

Janak J.F., *Phys. Rev.* **B 16** 255 (1977)

Jeanloz R., Ahrens T., Mao H. K. , and Bell P. M., *Science* **206**, 829 (1979)

Jo T., *J. Phys. Soc. Japan* **40** 715 (1976)

Jo T. amd Miwa H., *J. Phys. Soc. Japan* **40** 706 (1976)

Jo T., *J. Phys. Soc. Japan* **3** 794 (1982)

Johnson C.E., Ridout M.S. and Cranshaw T.E. 1963 *Proc. Phys. Soc.* **81** 1079 (1963)

Johnson D.D., Staunton J.B. and Pinski F.J., *Phys. Rev.* **B50** 1473 (1994)

Kajzar F. and Parette G., *Phys. Rev.* **B22** 5471 (1980)

Kakehashi Y., *J. Phys. Soc. Japan* **51** 94 (1982)

Kalpana G., Pari G., Mookerjee A. and Bhattacharyya A. K., *Int. J. Mod. Phys.* **B.**, (1998) (in press).

Kalpana G., Palanivel B. and Rajagopalan M., *Phys. Rev.* **B50** 12318 (1994)

Kaspar J. and Salahub D.R., *J. Phys. F: Met. Phys.* **13** 311 (1983)

Kashyap A., Garg K. B., Solanki A. K., Nautiyal T. and Auluck S., *Phys. Rev.* **B60** 2262 (1999)

Kerker G.P., *J. Phys. C: Solid State Phys.* **13** L189 (1980)

Kleinman L. and Bylander D.M., *Phys. Rev. Lett.* **48** 1425 (1982)

Klemm W. and Wahl K., *Z. Anorg. Allg. Chem.* **266** 289 (1951)

Kohn W. and Sham L. J., *Phys. Rev.* **A 140**, 1133 (1965)

Koi Y., Tsujimura T. and Hihara T. *J. Phys. Soc. Japan* **19** 1493 (1964)

Kubler J., *Physics Letters* **81A** 81 (1981)

Kudrnovský J., Drachal V. and Masek J., *Phys. Rev.* **B 35**, 2487 (1987)

Kudrnovský J. and Drachal V., *Phys. Rev.* **B 41**, 7515 (1990)

Kudrnovský J. and Drchal V., *Phys. Rev.* **B 41** 7515 (1990)

Kulikov N.I. and Demangeat C., *Phys. Rev.* **B55** 3533 (1997)

Kumar N. and Jayannavar A. M.*Phys. Rev.* **B32** 3345 (1985); *J. Phys. C: Solid State Phys.* **C19** 5513 (1986)

Kuhn A., Chevy A. and Naud M. J., *J. Cryst. Growth* **9**, 263 (1971)

Lambrecht W. R. L. and Andersen O. K. *Phys. Rev.* **B 34** 2439 (1986)

Langreth D.C. and Perdew J.P., *Phys. Rev.* **B15** 2884 (1977)

Langreth D.C. and Perdew J.P., *Phys. Rev.* **B21** 5469 (1980)

Langreth D.C. and Mehl M.J., *Phys. Rev.* **B28** 1809 (1983)

Lawniczak-Jablonska K., Iwanowski R. J., Golacki Z., Traverse A., Pizzini S., Fontaine A., Winter I. and Hormes J., *Phys. Rev.* **B 53**, 1119 (1996)

Li T., Luo H., Greene R.G. and Ruoff A.L., *Phys. Rev. Lett.* **74** 5232 (1995)

Lichtenstein A.I., Katznelson M.I. and Gubanov V.A., *J. Phys. F: Met. Phys.* **14** L125 (1984)

Ling M.F., Staunton J.B. and Johnson D.D. 1995 *J. Phys. C: Solid State Phys.* **7** 1863

Lu Z.W., Laks D.B., Wei S.H. and Zunger A., *Phys. Rev.* **B 50** 6642 (1997)

Luchini M. U. and Nex C. M. M., *J. Phys. C: Solid State Phys.* **20** 3125 (1987)

Luo H., Greene R.G., Ghandehari K., Li T. and Ruoff A.L., *Phys. Rev.* **B50** 16232 (1994)

Luo H., Ghandehari K., Greene R.G., Ruoff A.L., Trail S.S. and DiSalvo F.J. *Phys. Rev.* **B52** 7058 (1995)

Lutgemeier H. and Dubiel S.M. *Journal of Magnetism and Magnetic Materials* **28** 277 (1982)

Marshall W., *J. Phys. C: Solid State Phys.* **1** 88 (1968)

Martínez-Herrera F.J., Mejía-Lira F., Aguilera-Gunja F., Morán-Lopez J. L., *Phys. Rev.* **B31** 1686 (1985)

Matthews J.C., *J. Phys. Soc. Japan* **32** 110 (1972)

Mensz P.M., *Appl. Phys. Lett.* **64** 2148 (1994)

Methfessel M., *Phys. Rev.* **B 38**, 1537 (1988)

Methfessel M., Rodriguez C. O. and Andersen O. K. *Phys. Rev.* **B 40**, 2009 (1989)

Mirebeau L., Cadeville M.C., Parette G. and Campbell I.A., *J. Phys. F: Met. Phys.* **12** 25 (1982)

Mirebeau I., Hennion M. and Parette G., *Phys. Rev. Lett.* **53**687 (1985)

Mohn P.H. and Wolfarth E. P., *J. Phys. F* **17** 2421 (1987)

Mookerjee A *J. Phys. C: Solid State Phys.* **6** L205 (1973) ; *J. Phys. C: Solid State Phys.* **6** 1340 (1973)

Mookerjee A. and Prasad R., *Phys. Rev.* **B 48** 17724 (1993)

Muñoz A., Rodríguez-Hernández P. and Mujica A., *Phys. Stat. Solidi* **B 198** 439 (1996)

Muñoz A., Rodríguez-Hernández P. and Mujica A., *Phys. Rev.* **B54** 11861 (1996)

Mryasov O.N., Liechtenstein A. I., Sandratskii and Gubanov V. A., *J. Phys.: Condens. Matter* **39** 7683 (1991)

Mryasov O.N., Gubanov V.A. and Lichtenstein A.I., *Phys. Rev.* **B45** 12330 (1992)

Muraoka Y. *et al J. Phys. Soc. Japan* **40** 414 (1976)

Nowak H. J., Andersen O. K., Fujiwara T., Jepsen O. and Vargas P., *Phys. Rev.* **B 44**, 3577 (1991)

Paduani C. and Krause J.C., *Phys. Rev.* **B 58** 175 (1998)

Pandey R. and Sivaraman S., *J. Phys. Chem. Solids* **52**, 211 (1991)

Pari G., Mathi Jaya S., Subramoniam G. and Asokamani R., *Phys. Rev.* **B 51**, 16 575 (1995).

Pari G., Ramakumar R. and Mookerjee A., *Mod. Phys. Lett.* **B 10**, 505 (1996)

Parker S.G., Reinberg A.R., Pinnell J.E. and Holton W.C., *J. Electrochem. Soc.* **118** 979 (1971)

Peiris S.M., Campbell A.J. and Heinz D.L., *J. Phys. Chem. Solids* **55** 413 (1994)

Perdew J.P., *Phys. Rev. Lett.* **55** 1665 (1985)

Perdew J.P., *Phys. Rev.* **B33** 8822 (1986)

Perdew J.P. and Wang Y., *Phys. Rev.* **B33** 8800 (1986)

Pierron-Bohnes V., Cadeville M.C. and Gautier F., *J. Phys. F: Met. Phys.* **13** 1689 (1982)

Pierron-Bohnes V., Cadeville M.C. and Parette G., *J. Phys. F: Met. Phys.* **15** 1441 (1985)

Pinski F.J., *Phys. Rev. Lett.* **56** 2096 (1981)

Radhakrishnan P. and Livet F. , *Solid state comm.* **25** 597 (1978)

Rasolt M., Malmstrom D. and Geldart D.J.W., *Phys. Rev.* **B20** 3012 (1979)

Rasolt M. and Geldart D.J.W., *Phys. Rev.* **B21** 3158 (1980)

Richter R. and Eschrig H., *Proc. 7th General EPS conf.*, Pisa (1987)

Richter R. and Eschrig H., *J. Phys. F: Met. Phys.* **18** 1813 (1988)

Ruoff A.L. and Grzybowski T.A., *Solid State Physics under pressure* edited by S. Minomura (Terra Scientific, Tokyo, 1985)

Ruoff A.L., Li Ting, Ho A. C., Pai M-F, Luo H., Greene R.G. and Narayana C., *Phys. Rev. Lett.* **81** 2723 (1998)

Saha T., Dasgupta I. and Mookerjee A., *Phys. Rev.* **B 50** 13267 (1994)

Saha T., Dasgupta I. and Mookerjee A., *J. Phys.: Condens. Matter* **8** 1979 (1996)

Saha T., in Ph.D. thesis submitted to Calcutta University (1997)

Sanchez J.M. and Morán-López J. L., *J. Phys.: Condens. Matter* **1** (1989)

Sanyal B., Biswas P.P., Mookerjee A., Das G.P., Salunke H. and Bhattacharya A.K., *J. Phys.: Condens. Matter* **10** 5767 (1998)

Sarkar R.L. and Chatterjee S., *J. Phys. C: Solid State Phys.* **10** 57 (1977)

Sarma D. D. , Shanthi N., Barman S. R., Hamada N., Sawada H. and Terakura K., *Phys. Rev. Lett.* **75**, 1126 (1995)

Sato H., Arrott A. and Kikuchi R. *Journal of Physics and Chemistry of Solids* **10** 19 (1959)

Schroder K., *Phys. Rev.* **125** 1209 (1962)

Schwarz K. and Salahub D.R. , *Phys. Rev.* **B25** 3427 (1982)

Shick A. B., Drchal V., Kudrnovsky J. and Weinberger P., *Phys. Rev.* **B 54** 1610 (1996)

Shull C.G. and Wilkinson M.K., *Phys. Rev.* **97** 304 (1955)

Springborg M. and Andersen O. K., *J. Chem. Phys.* **87** 7125 (1987)

Staunton J.B., Johnson D.D. and Pinski F.J., *Phys. Rev.* **B50** 1450 (1994)

Stepanyuk V.S., Grigorenko A.A., Kozlov A.V., Farberovich O.V., Mikhalin V.V. and Stepanova E.V., *Sov. Phys. Solid State* **31** 207 (1989)

Stepanyuk V.S., Szász A., Farberovich O.V., Grigorenko A.A., Kozlov A.V. and Mikhalin V.V., *Phys. Stat. Solidi* **155** 215 (1989)

Stepanyuk V.S., Grigorenko A.A., Katsne'son A.A., Farberovich O.V. and Mikhalin V.V., *Sov. Phys. Solid State* **32** 1028 (1990)

Stoelinga J.H.M. and Gersdorf R., *Physics Letters* **19** 640 (1966)

Stukel D.J., *Phys. Rev.* **B2** 1852 (1970)

Swalin R.A., *Thermodyanamics of solids*, Wiley, New York (1962)

Syassen K., *Phys. Stat. Solid* **91** 11 (1985)

Tsunoda Y., *J. Phys.: Condens. Matter* **1** 10427 (1988)

Turek I., Kudrnovský J., Drchal V. and Weinberger P., *Phys. Rev.* **B 49** 3352 (1994)

Turek I. *et al* in *Electronic structure of disordered alloys, surfaces and interfaces* 1997, Kluwer Academic Publishers

Twardowski A., *J. Appl. Phys.* **67**, 5108 (1990)

Uba S., *Phys. Rev.* **B57** 1534 (1998)

Van Baal C.M., *Physica* **64** 571 (1973)

Van Camp P.E. and Van Doren V.E., *Int. J. Quantum Chem.* **55** 339 (1995)

Van Camp P.E. and Van Doren V.E., *Solid State Commun.* **98** 741 (1996)

Van Camp P.E. and Van Doren V.E., *Phys. Rev.* **B55** 775 (1997)

Van Vechten A., *Phys. Rev.* **187** 1007 (1969)

von Barth U. and Hedin L., *J. Phys. C: Solid State Phys.* **5** 1629 (1972)

Vonsovskii S.V., *Magnetism*, Wiley, New York (1974)

Waag A., Heinke H., Scholl S., Becker C. R., and Landwehr G., *J. Cryst. Growth* **131**, 607 (1993)

Waag A., Fisher F., Lugauer H.J., Litz T., Laubender J., Lunz U., Zhender U., Ossau W., Gerhardt T., Moller M. and Landwehr G., *J. Appl. Phys.* **80** 792 (1996)

Wang C.S., Klein B.M. and Krakauer H. 1985 *Phys. Rev. Lett.* **54** 1852 (1985)

Wang M. W., Phillips M. C., Swenberg J. F., Yu E. T., McCaldin J. O., and McGill T. C., *J. Appl. Phys.* **73**, 4660 (1993)

Wang M. W., Swenberg J. F., Phillips M. C., Yu E. T., McCadlin J. O., Grant R. W., and McGill T. C., *Appl. Phys. Lett.* **64**, 3455 (1994)

Wei S.H. and Krakauer H., *Phys. Rev. Lett.* **55** 1200 (1985)

Weir S.T., Vohra Y. K. and Ruoff A.L., *Phys. Rev.* **B33** 4221 (1986)

Weller D., Harp G.R., Farrow R.F.C., Cebollada A. and Sticht J., *Phys. Rev. Lett.* **72** 2097 (1994)

Weyrich K. H., *Phys. Rev.* **B 37** 10269 (1988)

Wijn H.P.J. and Landolt-Bornstein L., *Magnetic properties of metals, 3d, 4d and 5d Elements, Alloys and Compounds*, New Series, Group III, Vol. 19, Pt. a (Springer-Verlag, Berlin) (1986)

Wolverton C., Ozolins V. and Zunger A., *Phys. Rev.* **B 50**, 8355 (1997)

Wolverton C., Ozolins V. and Zunger A., *Phys. Rev.* **B 57** 4332 (1998)

Wu .P, Kershaw R., Dwight K., and Wold A., *Mater. Res. Bull.* **24**, 49 (1989)

Yamoka S., Shimmuro D., Nakazawa H. and Fukunaga O., *Solid State Commun.* **33** 87 (1980)

Yeh C.Y., Lu Z.W., Froyen S. and Zunger A., *Phys. Rev.* **B46** 10086 (1992)

Yim W.M., Dismakes J.P., Stofko E.J. and Paff R.J., *J. Phys. Chem. Solids* **33** 501 (1972)

Zachariasen W., *Z. Phys. Chem.* **128** 417 (1927)

Zimmer H.G., Winzen H. and Syassen K., *Phys. Rev.* **B32** 4066 (1985)